1-1-2015

Multiscale Simulations of Dynamics of Ferroelectric Domains

Shi Liu
University of Pennsylvania, upennliushi@gmail.com

Recommended Citation

Liu, Shi, "Multiscale Simulations of Dynamics of Ferroelectric Domains" (2015). *Publicly Accessible Penn Dissertations*. 1085.
http://repository.upenn.edu/edissertations/1085

Multiscale Simulations of Dynamics of Ferroelectric Domains

Abstract

Ferroelectric materials exhibiting switchable polarization have been used as critical components in electronics, memory, actuators and acoustics, and electro-optics. The applications of ferroelectric materials heavily rely on the interactions between the polarization and external perturbations, such as electric field, stress, and temperature. It is therefore crucial to understand the dynamics of ferroelectric response at finite temperature. Despite the tremendous advance of computational power and the success of first-principles methods, large-scale simulations of dynamics in oxides at finite temperature can still only be performed using classical atomistic potential. We first develop a model potential based on principles of bond-valence and bond-valence vector conservation. The model potentials for PbTiO3 and BiFeO3 are parameterized using the results from first-principles calculations. The bond-valence-based force field allows for molecular dynamics simulations of ferroelectric response at large time and length scale. The intrinsic inertial response of ferroelectric domain walls is studied in PbTiO3. Examination of the evolution of the polarization and local structures of domain walls reveal that they stop moving immediately after the removal of the electric field, demonstrating that ferroelectric domain walls do not exhibit significant intrinsic inertial response. Taking the 90Â° domain walls in PbTiO3 as an example, we quantitatively estimate the domain wall velocity under a wide range of temperatures and electric fields. We find that many properties of ferroelectrics are dictated by the intrinsic nature of domain walls. We demonstrate that even in the absence of defects the intrinsic temperature- and field-dependence of the wall velocity can be described with a strongly non-linear creep-like region and a power-law depinning-like region. We propose a simple universal nucleation-and-growth-based analytical model that is able to quantify the dynamics of all types of domain walls in various ferroelectrics; this enables the prediction of the temperature- and frequency-dependence of coercive fields at finite temperature from first-principles. We also investigate the orientation-dependent evolution of nanoscale ferroelectric domain structures in PbZr0.2Ti0.8O3 films. Molecular dynamics simulations predict both 180Â° for (001)-/(101)-oriented films and 90Â° multi-step switching for (111)-oriented films, and these processes are subsequently observed in stroboscopic piezoresponse force microscopy. Finally, we investigate the domain walls in organometal halide perovskites. We find that organometal halide perovskites can form both charged and uncharged domain walls, due to the flexible orientational order of the organic molecules. The presence of charged domain walls will significantly reduce the band gap. We demonstrate that charged domain walls can serve as segregated channels for the diffusion of charge carriers.

Degree Type
Dissertation

Degree Name
Doctor of Philosophy (PhD)

Graduate Group
Chemistry

First Advisor
Andrew M. Rappe

Keywords
Bismuth Ferrite, Density Functional Theory, Domain Wall, Lead Titanate, Molecular Dynamics, Organometal Halide Perovskite

Subject Categories
Chemistry | Mechanics of Materials | Physical Chemistry

MULTISCALE SIMULATIONS OF DYNAMICS OF FERROELECTRIC DOMAINS

Shi Liu

A DISSERTATION

in

Chemistry

Presented to the Faculties of the University of Pennsylvania

in

Partial Fulfillment of the Requirements for the

Degree of Doctor of Philosophy

2015

Supervisor of Dissertation	Graduate Group Chairperson
Andrew M. Rappe	Gary A. Molander
Professor of Chemistry, and Materials Science and Engineering	Hirschmann-Makineni Professor of Chemistry

Dissertation Committee

Joseph E. Subotnik	Associate Professor of Chemistry
Jeffery Saven	Professor of Chemistry
Vivek Shenoy	Professor of Materials Science and Engineering

To my parents and sister,

for their love and supports

Acknowledgements

First and foremost, I would like to thank Professor Andrew M. Rappe, who not only opened the fascinating door of computational materials science to me, but also demonstrated how challenging, interesting and rewarding science could be. I am constantly inspired by his never-ending innovations, his kindness and supports to students and young scientists, and his dedications to science. I am deeply grateful to the valuable knowledge and enthusiasm for science he conveyed to me, which I hope I can pass them to more people.

I would like to thank my thesis committee, Professor Joseph E. Subotnik, Professor Jeffery Saven, Professor Dawn A. Bonnell and Professor Vivek Shenoy for their constructive comments and helpful suggestions. I thank Professor Masoud Soroush, Professor Lane Martin, Professor Aaron Lindenberg, and Professor Mitra Taheri for providing insights into work collaborated together that eventfully lead to many parts of this thesis.

I would like to express my sincere thanks to all the members of Professor Rappe's research group, both past and present, for their mentors, helps, advices, and supports. I thank Dr. Ilya Grinberg for teaching me almost everything I know about ferroelectrics and providing insights when I was buried by data. I thank Dr. Sriraj Srinivasa for showing me the beauty of computational chemistry and teaching me almost everything I know about polymer chemistry. I enjoy the collaborations with Dr. Jianmin Tao, Dr. Hiroyuki Takenaka, Dr. Fenggong Wang, Dr. Youngkuk Kim, Dr. Liang Z Tan, Dr. Tingting Qi, Dr. Steve Young, Dr. Nazanin Moghadam, Fan Zheng, Diomedes Saldana-Greco, Yubo Qi,

Rob Wexler, and Nathan Koocher; they are fantastic team members, and I own my successes to their selfless supports. My sincere thanks also go to Professor Shin-Han Young, Professor Joseph Schick, Professor Gaoyang Gou, Dr. Seungchul Kim, Dr. Dmitri Volja, Dr. Miguel Méndez Polanco, Dr. Lai Jiang, Dr. John Mark Martirez and Dr. John Brehm, and Jin Yang for sharing their valuable knowledge.

I am extremely grateful to my parents and sister. There is no measure of my thanks, love, and gratitude to them, for their constant supports and love in so many ways. Finally, I would like to thank Dr. Tingting Wu, without whom my whole life would be much less fun and much more difficult. Your love, your inspiration, and your smile shine my way. You are the one truly deserving of my deepest and enduring love.

ABSTRACT

MULTISCALE SIMULATIONS OF DYNAMICS OF FERROELECTRIC DOMAINS

Shi Liu

Andrew M. Rappe

Ferroelectric materials exhibiting switchable polarization have been used as critical components in electronics, memory, actuators and acoustics, and electro-optics. The applications of ferroelectric materials heavily rely on the interactions between the polarization and external perturbations, such as electric field, stress, and temperature. It is therefore crucial to understand the dynamics of ferroelectric response at finite temperature. Despite the tremendous advance of computational power and the success of first-principles methods, large-scale simulations of dynamics in oxides at finite temperature can still only be performed using classical atomistic potential. We first develop a model potential based on principles of bond-valence and bond-valence vector conservation. The model potentials for $PbTiO_3$ and $BiFeO_3$ are parameterized using the results from first-principles calculations. The bond-valence-based force field allows for molecular dynamics simulations of ferroelectric response at large time and length scale. The intrinsic inertial response of ferroelectric domain walls is studied in $PbTiO_3$. Examination of the evolution of the polarization and local structures of domain walls reveal that they stop moving immediately after the removal of the electric field, demonstrating that ferroelectric domain walls do not exhibit significant intrinsic inertial response. Taking the 90° domain walls in $PbTiO_3$ as an example, we quantitatively estimate the domain wall velocity under a wide range of temperatures and electric fields. We find that many properties of ferroelectrics are dictated by the intrinsic nature of domain walls. We demonstrate that even in the absence of defects the intrinsic temperature- and field-dependence of the wall velocity can be described with a strongly non-linear creep-like region and a power-law depinning-like region. We propose a simple universal nucleation-and-growth-based analytical model that is able to quantify the dynamics of all types of domain walls in various ferroelectrics; this enables the prediction of the temperature- and frequency-dependence of coercive fields at finite temperature from first-principles. We also investigate the orientation-dependent evolution of nanoscale ferroelectric domain structures in $\mathrm{PbZr_{0.2}Ti_{0.8}O_3}$ films. Molecular dynamics simulations predict both 180° for (001)-/(101)-oriented films and 90° multi-step switching for (111)-oriented films, and these processes are subsequently observed in stroboscopic piezoresponse force microscopy. Finally, we investigate the domain walls in organometal halide perovskites. We find that organometal halide perovskites can form both charged and uncharged domain walls, due to the flexible orientational order of the organic molecules. The presence of charged domain walls will significantly reduce the band gap. We demonstrate that charged domain walls can serve as segregated channels for the diffusion of charge carriers.

Contents

List of Tables

List of Figures

Preface

The materials in the Abstract and Chapter 1 are adapted from materials appeared in five published papers and one submitted paper as detailed below.

The materials in Chapter 4 appeared in S. Liu, I. Grinberg, H. Takenaka, and A. M. Rappe, "Reinterpretation of bond-valence model with bond-order formalism: an improved bond-valence based interatomic potential for $PbTiO_3$", *Phys. Rev. B* **88**, 104102 (2013). Copyright © 2013 American Physical Society.

The materials in Chapter 5 appeared in S. Liu, I. Grinberg, A.M. Rappe, "Development of a bond-valence based interatomic potential for $BiFeO_3$ for accurate molecular dynamics simulations", *J. Phys.: Condens. Matter* **25**, 102202 (2013). Copyright © 2013 IOP Publishing Ltd.

The materials in Chapter 6 appeared in S. Liu, I. Grinberg, A.M. Rappe, "Exploration of the intrinsic inertial response of ferroelectric domain walls via molecular dynamics simulations", *Appl. Phys. Lett.* **103**, 232907 (2013). Copyright © 2013 AIP Publishing LLC.

The materials in Chapter 7 has been submitted as S. Liu, I. Grinberg, A.M. Rappe, "Universal intrinsic origin for ferroelectric domain wall motion", to *Nature*, which is currently under review.

The materials in Chapter 8 appeared in R. Xu, S. Liu, J. Karthik, A.R. Damodaran, I. Grinberg, A.M. Rappe, and L.W. Martin, ”Ferroelectric polarization reversal via successive ferroelastic transitions”, *Nature Mater.* **14**, 79 (2015). Copyright © 2014 Macmillan Publishers Limited. R.X. and L.W.M. designed the experiments. S.L., I.G. and A.M.R. designed the simulation strategy. R.X. performed the experiments. S.L. carried out the MD simulations. R.X., J.K., A.R.D. and L.W.M. analyzed the experimental results. S.L., I.G. and A.M.R. analyzed the simulation results. R.X., S.L., I.G., A.M.R. and L.W.M. co-wrote the paper.

The materials in Chapter 9 appeared in S. Liu, F. Zheng, N.Z. Koocher, H. Takenaka, F. Wang, and A.M. Rappe, “Ferroelectric domain wall induced band-gap reduction and charge separation in organometal halide perovskites”, *J. Phys. Chem. Lett.* **6**, 693 (2015). Copyright © 2015 American Chemical Society.

Chapter 1

Introduction

Ferroelectric materials possess a spontaneous, switchable macroscopic polarization in the absence of an applied field [1]. The switchable polarization makes ferroelectrics critical components in non-volatile random access memory [2–5], actuators and sensors [6], and electro-optic devices [7]. The use of ferroelectric perovskite oxides in a variety of technological applications has prompted extensive investigations of their structures and dynamics. First-principles density functional theory (DFT) has served as a powerful tool to elucidate the structure-property relationship for ferroelectric materials [8–10]. Despite the success of first-principles methods, the great computational expense and the difficulties of studying finite-temperature properties have driven the development of more efficient atomistic and effective Hamiltonian potentials for molecular dynamics (MD) simulations [11–22]. The effective Hamiltonian method requires the dynamical modes that determine a specific property should be known *a priori*. Therefore, the MD simulations with an atomistic potential accounting for all the modes still own distinct advantages. However, the development of general atomistic potentials for ferroelectric oxides has proven difficult due to the complex nature of various metal-oxygen bonds [23].

Previously, an atomistic potential based on the widely used bond-valence (BV) theory [24] has been used to study phase transitions and domain wall motions in $PbTiO_3$ [25] as well as the structure and dynamics in the classic $0.75PbMg_{1/3}Nb_{2/3}O_3$–0.25 $PbTiO_3$ relaxor ferroelectric material [26, 27]. However, the potentials were found to be accurate for constant-volume constant-temperature (NVT) simulations only, with incorrect ground-state structures obtained when the constant volume constraint is lifted. In Chapter 4, we present a modified model potential based on the principles of bond-valence and bond-valence vector (BVV) conservation [28]. An energy term, bond-valence vector energy, is introduced into the atomistic model. The relationship between the bond-valence model and the bond-order potential is derived analytically in the framework of a tight-binding model, providing a quantum mechanical justification for the bond-valence potential. We parameterized the model potential for $PbTiO_3$. This model potential can be applied both to canonical-ensemble and isobaric-isothermic ensemble (NPT) MD simulations. Our force field also reproduces the experimental phase transition in NVT MD simulations and exhibited the experimental sequence of temperature-driven and pressure-driven phase transitions in NPT simulations. In Chapter 5, we apply this model to $BiFeO_3$, a multiferroeic perovskites oxides with high Curie temperature and Néel temperature [29–31]. We optimize the atomistic potential for $BiFeO_3$ based on DFT results. This classical interatomic potential reproduces the ferroelectric-to-paraelectric phase transition in both NVT and NPT simulations. The calculated domain wall energies for 71°, 109°, 180° domain walls agree well with DFT results. The success of our simple model potential for $BiFeO_3$ indicates that BV and BVV conservation provides firm basis for the development of accurate atomistic potentials for complex oxides.

In many cases, ferroelectrics adopt a multi-domain state where domains with polarization uniformly oriented in one direction are bounded by domains with polarization pointing in other directions. The interface separating regions of different polarities is called the domain wall [32]. The domain wall can be moved by applying external stimulus, such as electric filed and stress. The ability of manipulate domain walls with an external stimulus offers a powerful paradigm for novel device engineering at the nanoscale [5]. One important question that is of interest both scientifically and technologically is whether the ferroelectric domain wall has significant inertial response. In Chapter 6, we address this problem with NPT MD simulations of 180° and 90° domain walls under applied electric fields. Examination of the evolution of the polarization and local structure of domain walls reveals that they stop moving immediately after the removal of electric field, demonstrating that ferroelectric domain walls do not have significant intrinsic internal response.

Despite intense studies of domain walls, achieving controlled material design and device optimization for ferroelectrics remains a significant challenge. Experimentally, the observed dynamics of domain walls are usually explained as the behavior of an elastic interface pinned by a random potential generated by defects, which appear to be strongly sample-dependent [33–46]. Theoretically, it is difficult to connect 0 K first-principles-based microscopic quantities (e.g., domain wall energy) to finite-temperature macroscopic properties (e.g., coercive field) that are critical for material design and device performance [47]. In Chapter 7, taking the 90° domain walls in $PbTiO_3$ as an example, we explore the intrinsic ferroelectric response of domain walls with MD simulations under a wide range of temperatures and electric fields. We find that even in the absence of defects the intrinsic temperature- and field-dependence of the wall velocity can be described with a non-linear creep-like region and a power-law depinning-like region; the transition indicates a transformation from the nucleation-limited mechanism with large critical nucleus under low fields to the growth-limited mechanism with small critical nucleus under high fields. The estimated theoretical dynamical exponent μ and the velocity exponent θ agree well with the experimental values, highlighting the intrinsic origin for the domain wall motion in real materials. By mapping non-180° domain walls to a 180° domain wall, we propose a simple universal nucleation-and-growth-based analytical model that is able to quantify the dynamics of all types of domain walls in various ferroelectrics; this enables the prediction of the temperature- and frequency-dependence of coercive fields at finite temperature from first principles. This work offers a unified picture for domain wall motion and also an efficient framework for optimizing material properties of ferroelectrics.

In Chapter 8, we investigate the nature of switching in $PbZr_{0.2}Ti_{0.8}O_3$ thin films with a combination of thin film epitaxy, macro- and nanoscale property and switching characterization, and MD simulations. Differences are demonstrated between (001)-/(101)- and (111)-oriented films, with the latter exhibiting complex, nano-twined ferroelectric domain structures with high densities of 90° domain walls and broadened switching characteristics. Our MD simulations predict both 180° and 90° switching and these processed are subsequently observed in stroboscopic piezoresponse force microscopy. These observations provide insight into a previously unexplored aspect of ferroelectric switching and highlight the complexity of these materials. Such results have implications for our understanding of ferroelectric switching and offer opportunities to change domain reversal speed and potentially lead to interesting multi-state devices.

Finally, in Chapter 9, we explore the domain structures in organometal halide perovskites, a promising solar-cell material for next-generation photovoltaic applications [48–54]. We find that organometal halide perovskites can form both charged and uncharged domain walls, due to the flexible orientational order of the organic molecules. The electronic band gaps for domain structures possessing 180° and 90° walls are estimated with density functional theory. It is found that the presence of charged domain walls will significantly reduce the band gap by 20%-40%, while the presence of uncharged domain walls has no substantial impact on the band gap. We demonstrate that charged domain walls can serve as segregated channels for the diffusion of charge carriers. These results highlight the importance of ferroelectric domain walls in hybrid perovskites for photovoltaic applications and suggest a possible avenue for device optimization through domain patterning.

Chapter 2

Ferroelectrics and domain walls

2.1 Ferroelectric perovskite oxides

A ferroelectric is defined as an insulating system with two or more discrete stable or metastable states possessing different nonzero spontaneous macroscopic polarization in the absence of external electric field [1]. The spontaneous polarization can be switched by applying external perturbations such as electric and stress field (Fig. 2.1). Ferroelectricity was first discovered in Rochelle salt (sodium potassium tartrate tetra hydrate, $NaKC_4H_4O_6 \cdot 4H_2O$) by Valasek in 1920 [55]. The ballistic galvanometer studies of charge and discharge of Rochelle salt clearly demonstrated the switchable polarization and its significant temperature dependence [56–58], which eventually leads to the firm establishment of the term *ferroelectricity*. The study of ferroelectricity was greatly facilitated by the discovery of stable ferroelectric oxides, barium titanate ($BaTiO_3$), with the perovskite structure in early 1940s [59–61]. The name "perovskite" in materials science is generally referred to a class of materials (formula $AB\mathrm{O}_3$) with the same type of crystal structure as calcium titanium oxide, $CaTiO_3$. The perovskite structure (Fig. 2.2) consists of corner-shared $B\mathrm{O}_6$ octahedra with the B cation in the body center of the unit cell. This structure is able to adapt to a mismatch between the equilibrium A–O and B–O bond length. Moreover, it tolerates multiple types of A-site/B-site cations, allowing for realization of a large number of stoichiometric perovskites [62].

The discovery of ferroelectricity in $BaTiO_3$ was significant in a number of ways [23]. First, it demonstrated that ferroelectricity can be realized in inorganic materials without hydrogen bonding, which was previously suspected to be crucial for ferroelectric behavior. Second, the perovskite structure is much simpler than the Rochelle salt structural, making the analysis much simpler. Finally, after the discovery of $BaTiO_3$, a large number of other perovskites are found to support ferroelectricity (e.g., $PbTiO_3$, $KNbO_3$), and display other interesting electronic properties, such as antiferroelectricity in $PbZrO_3$ [63].

This thesis is focused on two technologically important ferroelectric perovskites, $PbTiO_3$ and $BiFeO_3$. Pure $PbTiO_3$ forms the end member of a number of solid solution systems with high electromechanical coupling properties, such as $Pb(Zr_{1-x}Ti_x)O_3$ (PZT), $PbZn_{1/3}Nb_{2/3}O_3$-$PbTiO_3$ (PZN-PT) and $PbMg_{1/3}Nb_{2/3}O_3$-$PbTiO_3$ (PMN-PT). [64] $PbTiO_3$ has a well-defined single transition with $T_C = 766$ K from a paraelectric cubic to a ferroelectric tetragonal phase [65]. The origin of ferroelectricity was attributed to the delicate balance between the long-range Coulomb forces and short-range repulsion [9]. In general, long-range Coulomb interaction favors a ferroelectric distortion, while the short-range repulsion will stabilize the paraelectric cubic phase. In $PbTiO_3$, the hybridization between the d-orbital of Ti atom at B site and p-orbital of oxygen atoms soften the B–O repulsion and allows the ferroelectricity. $BiFeO_3$ is a multiferroic perovskite oxide (Fig. 2.3) with high Curie and Neel temperature ($T_C \approx 1100$ K and $T_C \approx 643$ K) [29, 30]. The room-temperature phase of $BiFeO_3$ is classed as rhombohedra (point group $R3c$) [30]. The perovskite-type unit cell has a lattice constant of 3.965 Å and a rhombohedral angle of 89.3-89.4°, with ferroelectric polarization along the [111] direction [66].

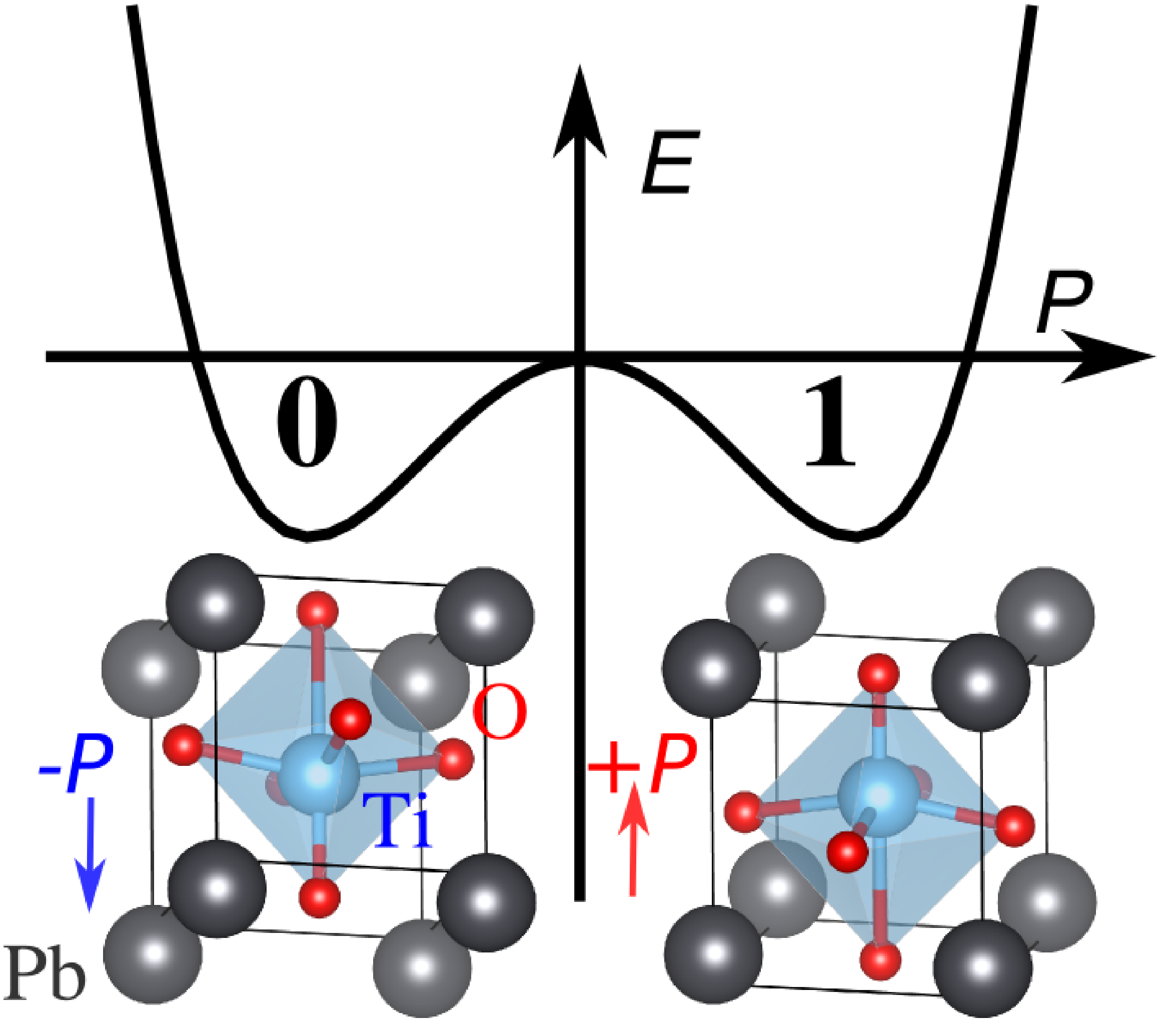

Figure 2.1: Schematic diagram of free energy as a function of polarization for a ferroelectric $PbTiO_3$ unit cell. The two degenerated ground states can serve as binary states in memory device.

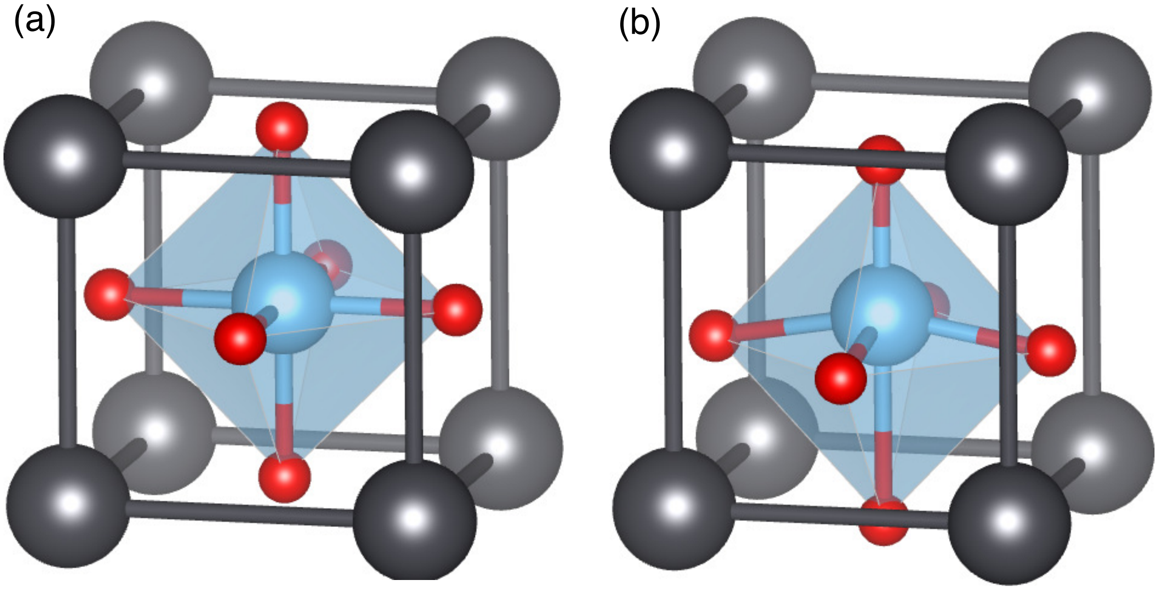

Figure 2.2: Perovskite (ABO_3) structure. (a) Cubic $PbTiO_3$ (b) Tetragonal $PbTiO_3$

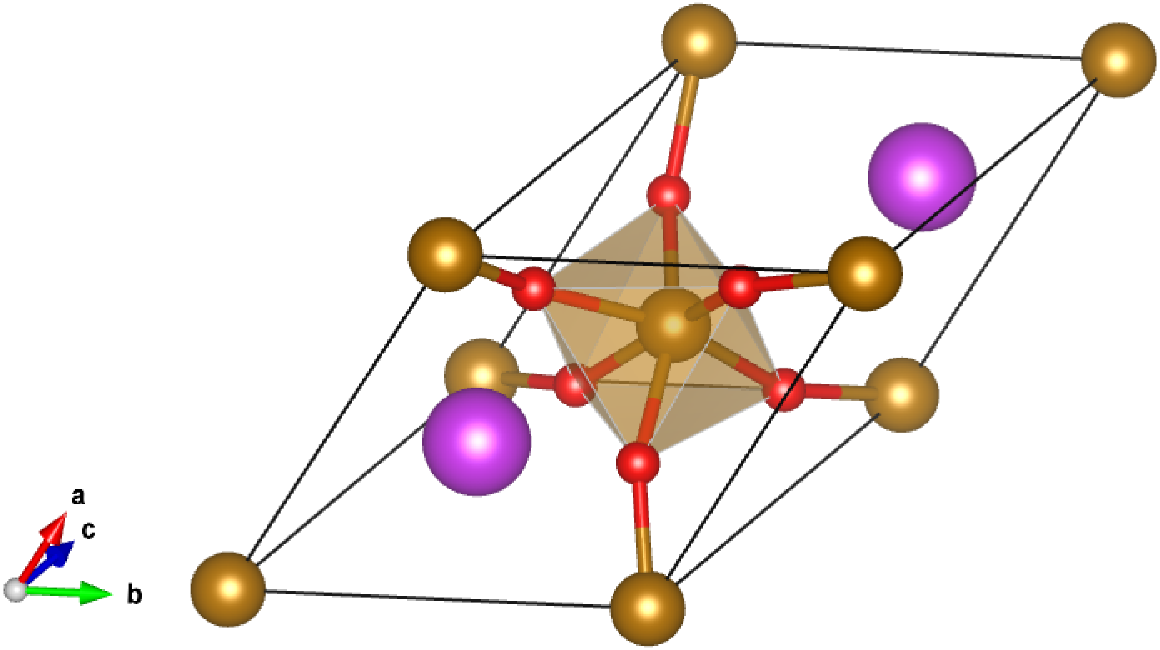

Figure 2.3: Structure of $R3c$ BiFeO$_3$.

2.2 Ferroelectric domains and domain walls

A domain is defined as a continuous volume within the material that dipoles align along the same direction. The formation of domains and domain walls in a bulk ferroelectric material is inevitable [32]. Many factors including strain, microscopic defects, surface charges, depolarization fields, and the thermal and electrical history of the sample may cause the formation of domains [67]. The equilibrium domain pattern for a particular (mechanical and electrostatic) boundary condition is determined by the minimization of the total energy ($\varepsilon_{\text{total}}$) of the crystal. In terms of energy density, the general formalism is [68]

$$\varepsilon_{\text{total}} = \varepsilon_e + \varepsilon_q + \varepsilon_{\text{DW}} + \varepsilon_s, \tag{2.1}$$

where ε_e is the elastic energy, ε_q is the electrostatic energy, ε_{DW} is the domain wall (interface) energy and ε_s is the surface energy associated with crystal terminations. Last decade has also seen a surge of interests in ferroelectric thin films grown over oxide substrates of similar lattice constants [69, 70]. In the thin-film form, film thickness and the mismatch of film-substrate lattice constants will also influence the formation and stability of domain configurations.

In experiments, piezoresponse force microscopy (PFM) is widely used to visualize and manipulate domains at nanoscale [71–75]. In PFM, an alternating voltage, $V = V_{dc} + V_{ac}\cos(\omega t)$ is applied through the scanning probe tip which causes periodic local vibrations (piezoelectric response) of the sample surface (Fig. 2.4). The resulting oscillations of the cantilever are detected and sensitively read out with the help of a lock-in amplifier (LLA) [76]. The first harmonic component, $A_{1\omega}$, of the tip defection, $A = A_0 + A_{1\omega}\cos(\omega t + \phi)$, depends on the tip motion and is given in the units of length; the phase ϕ carries information of the local polarization direction below the tip [77]. For example, the application of a positive bias on a c^- ferroelectric domain (polarization vector normal to the surface pointing downward) will have $\phi = 0°$; for a c^+ domain, $\phi = 180°$ under a positive tip bias. The ability to apply field though the PFM tip also enables local switching experiments.

A domain wall is defined as the interface separating neighboring domains of different polarities. The type of a domain wall is defined by the relative angle between the orientations of the polarization axes of the domains adjacent to it [32]. For example, Figure 2.5 shows domain structures with 180° and 90° domain walls in $\mathrm{PbTiO_3}$. First-principles density functional theory calculations reveal that the widths of domain walls are of the order of two lattice constants or less [78, 79]. However, transmission electron microscopy (TEM) studies reported widely ranging values between 10–60 Å [80–82]. The theory-experiment disagreement in values of domain wall widths may be attributed to the presence of defects and/or inhomogeneous stress field in the vicinity of domain boundaries. It should be noted that the domain wall widths calculated from first-principles are intrinsic values for defect-free ideal crystals, and therefore is a lower limit for the width of a domain wall.

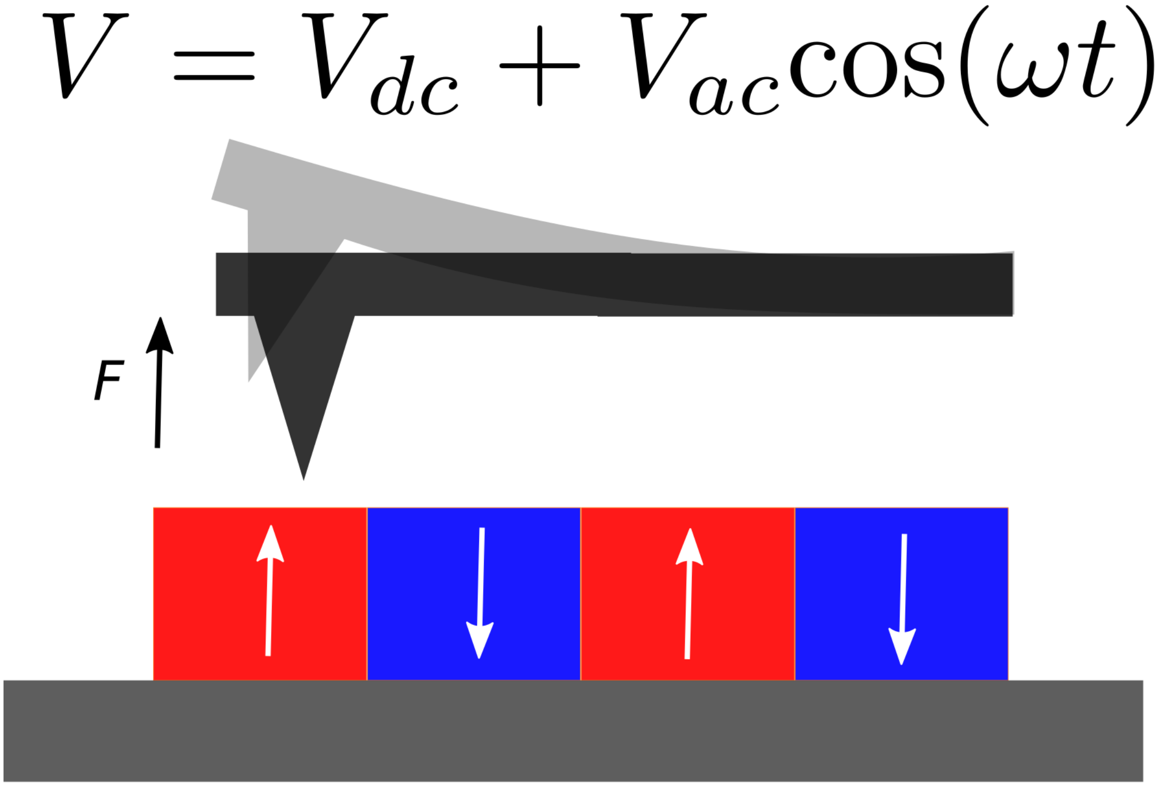

Figure 2.4: Schematic diagram of PFM detection. Local deformation of the sample surface leads to deflection of the cantilever.

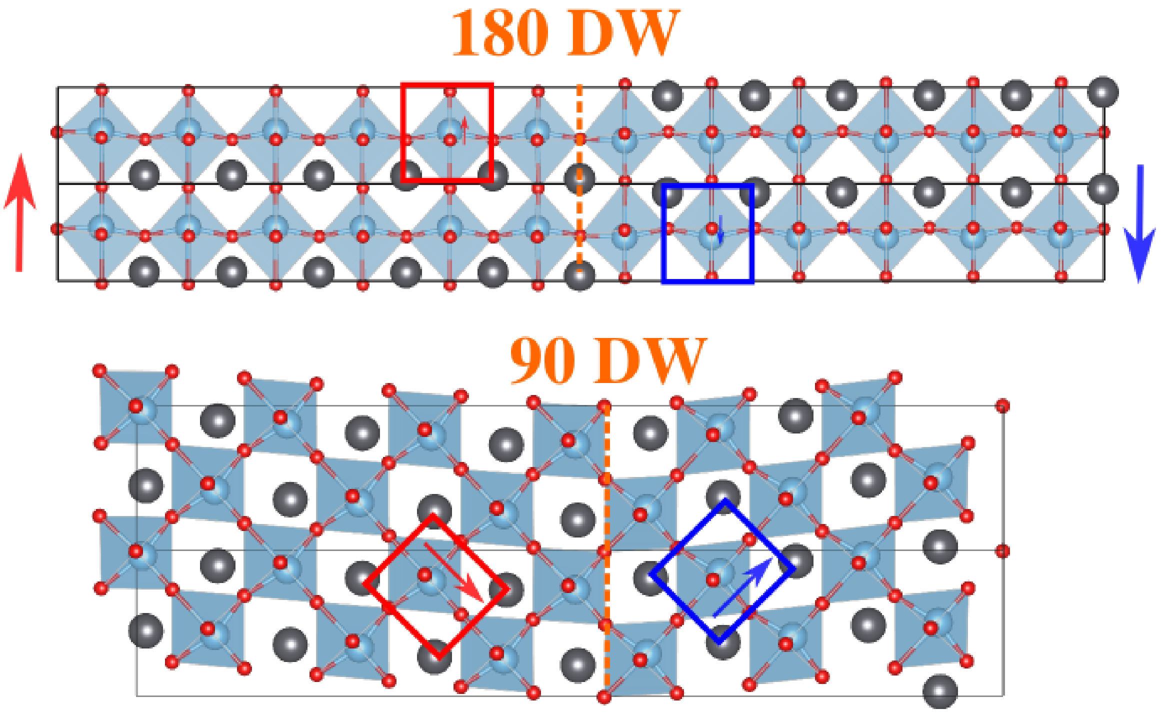

Figure 2.5: Domain wall structures in $PbTiO_3$.

2.3 Domain wall motion

In response to an external perturbation that selects for one polarization state over another, the domain wall will move to increase the size of the domain favored by the perturbation. The model for domain wall motion involves thermal nucleation of oppositely polarized nuclei aligning along with the electric field at the domain wall and their subsequent lateral expansion. This nucleaiton-and-growth was used to describe the 180° domain wall motion in $BaTiO_3$ crystals [33–35]. The energy of a nucleus U in the presence of a electric field E can be written as

$$U = -2P_sEV + \sigma_{\mathrm{DW}}S, \tag{2.2}$$

where P_s is the spontaneous polarization, V is the volume of the nucleus, S is the surface area of new domain walls, and σ_{DW} is the domain wall energy. The nuclei of new domains become stable and grow if the energy gain from aligning dipoles along with the electric field supersede the energy penalty for forming new domain walls. However, it was shown that a model assuming a sharp triangular nucleus (Fig. 2.6a) would necessitate implausibly large nuclei that leads to unrealistically large nucleation energies [83]. It was later revealed with multiscale simulations that the nucleus has a square shape with a diffuse interface (Fig. 2.6b). The nature of the diffuse interface significantly reduces the nucleation barrier and hence gives rise to much lower activation fields for domain wall motion [25].

Efforts have been made to estimate coercive fields with phenomenological free-energy theory [84, 85]. However, theoretical predictions for coercive fields are orders of magnitude higher than the experimentally observed values. Kim et al. calculated the theoretical coercive fields as 2.75 MV/cm for $LiTaO_3$ and 5.42 MV/cm for $LiNbO_3$ with a Landau-Ginsburg-Devonshire (LGD) type phenomenological model [84]. In contrast, the coercive fields for near-stoichiometric $LiTaO_3$ is $\approx$ 17 kV/cm, for near-stoichiometric $LiNbO_3$ is $\approx$ 40 kV/cm, and $\approx$210 kV/cm for their congruent compositions [86, 87]. Similarly, the idea intrinsic coercive field for PZT thin films estimated from first-principles ranged from 2.5 MV/cm to 10 MV/cm, [85] which are serval orders of magnitude higher than experimental values (10 kV/cm) [88–91]. These discrepancies were usually attributed to the presence of various crystal inhomogeneities and defects in real materials. In Chapter 7, we propose a simple universal nucleation-and-growth-based analytical model that is able to quantify the dynamics of all types of domain walls in various ferroelectrics; this enables the prediction of the temperature- and frequency-dependence of coercive fields at finite temperature from first-principles. The coercive fields estimated from our model agree well with experimental results, resolving long-standanding inconsistencies between the coercive fields calculated from phenomenological models and measured experimentally.

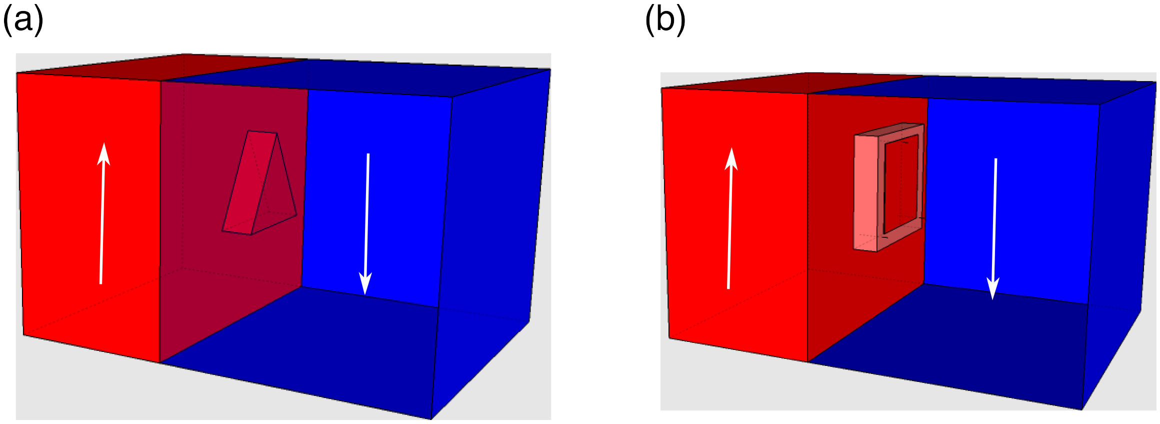

Figure 2.6: Schematic illustration of the nucleation model for 180° domain wall motion. (a) Miller–Weinreich model with a sharp triangular nucleus. (b) Shin-Grinberg-Rappe model with a square nucleus with a diffuse interface.

2.4 Creep and depinning

The dynamics of domain wall is usually understood as an elastic interface moving in a disordered media [92]. The competition between the elasticity, which tends to flatten the domain wall, and pinning of defects, which prevents the domain wall from sliding, is likely to govern the complex dynamical behavior of domain walls [46]. Figure 2.7 shows the velocity of the domain wall as a function of the driving force. In the absence of thermal activation (T = 0), the domain wall remains pinned until the driving force (F) reaches a critical threshold (F_c), then the domain wall moves with the velocity increasing abruptly. This behavior resembles the evolution of the order parameter during a second-order phase transition. Therefore, a universal scaling $v \propto (F - F_c)^\theta$ may be expected, where θ is called velocity exponent. When the driving force is high enough compared to the pinning contribution, the velocity becomes linear with the driving force $v \propto F$. In the presence of thermal fluctuation ($T > 0$), the domain wall may move under subcritical forces $F \ll F_c$. In this region, the domain wall has a strongly non-linear creep response to the external driving force,

$$v \propto \exp\left[-\frac{U_c}{k_B T}\left(\frac{F_c}{F}\right)^{\mu}\right]. \tag{2.3}$$

where U_c is is a characteristic energy scale and μ is called dynamical exponent. The dynamical exponent depends on the dimensionality of the system and the universality class of the disorder. The dynamical exponent $\mu = 1$ is usually ascribed to the random-field nature of the defects which break the symmetry of the ferroelectric double-well potential [39, 40], while $\mu = 0.5$ is an indication of random-bond defects which locally modify the symmetric ferroelectric double-well potential depth [36, 41, 42].

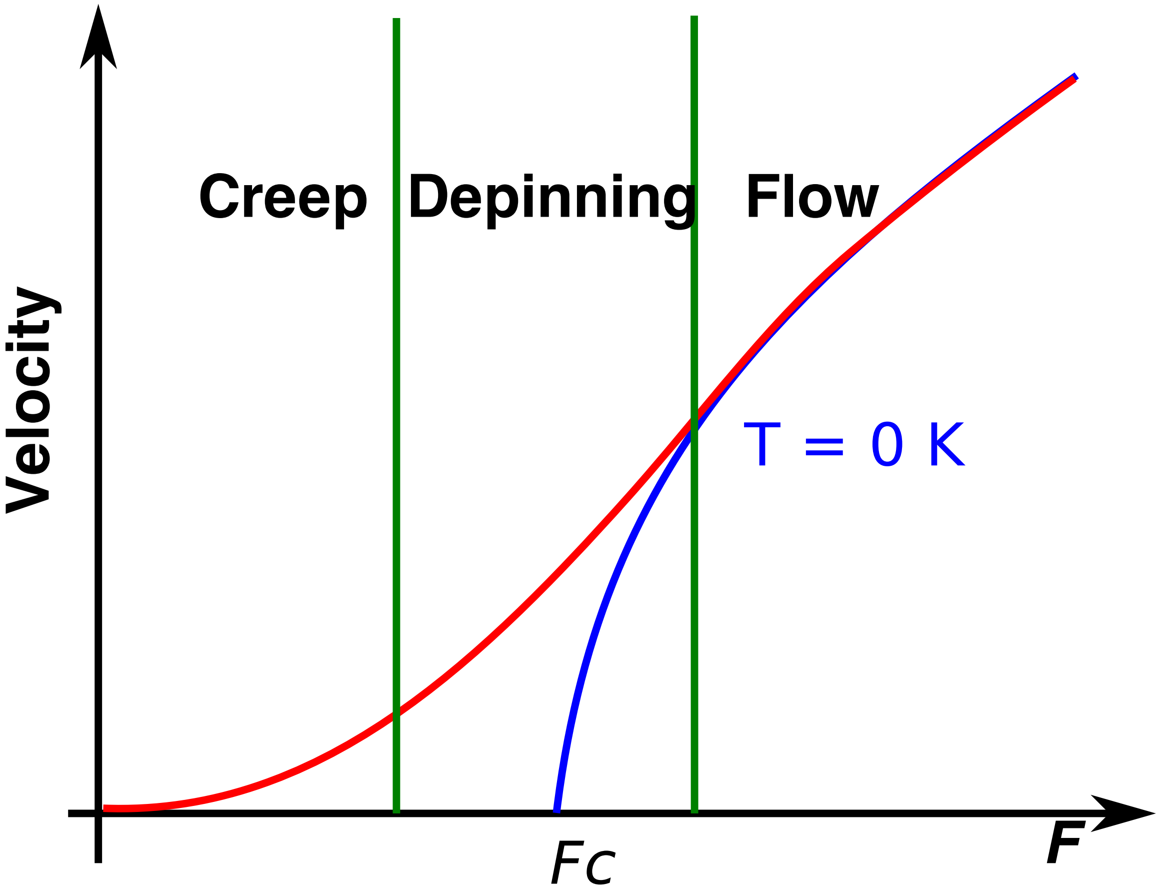

Figure 2.7: Velocity of an elastic interface as a function of the driving force.

Chapter 3

Theory and methodology

3.1 Introduction

Since 1911, it has been known that atoms and molecules are composed of electrons and nuclei (protons and neutrons). Classical mechanics predict that electrons will collapse into nuclei within a femtosecond. Hence, atoms, molecules, and other complex matters can not exist in a world governed by classical mechanics. This conundrum is resolved by quantum mechanics, which well explained the existence of matters. The ability of quantum mechanics to predict the total energy of a system of electrons and ions allows for the calculations of all physical properties of atoms, molecules, and solids [93]. Nearly all physical properties are related to the total energies or to differences between total energies. For example, the ground-state geometry of a molecule can be determined by minimizing the total energy as a function of internal coordinates (e.g., bond lengths and angles); the value of the equilibrium lattice constant of a crystal is the value of the lattice constant that gives the lowest energy. Computational modeling with quantum mechanics (first-principles) have been used to address a large amount of problems in a wide range of scientific disciplines.

Despite the tremendous success of first-principles methods, simulations based on classical mechanics still play a significant role in providing microscopic insights into the structure, dynamics and thermodynamics of complex systems consisting of large numbers of atoms [94]. Molecular dynamics (MD) simulations is a technique that calculates the time dependent behavior of an ensemble of atoms by integrating Newton's laws of motion [95]. In MD simulations, all atoms or ions are treated as structureless classical particles, interacting with each other through a predefined interatomic potential. With the knowledge of the force on each atom, the acceleration of each atom in the system is calculated according Newtons's second law ($F = ma$). Integration of the equations of motion then yields a trajectory of configurations that specifies how the positions, velocities and accelerations vary with time. From this trajectory, the average values of properties can be determined as a function of the positions and momenta of the particles in the system. Therefore, to carry out a MD simulation, one only needs the initial positions of the atoms, an initial distribution of velocities and a predefined potential energy function specifying all the interatomic interactions. The equations of motion are time reversible and deterministic: for a system of particles with given positions and velocities, the state of the system can be determined at any time in the future or the past.

3.2 Computational quantum mechanics

3.2.1 The Born-Oppenheimer approximation

The Schrödinger equation plays the central role in quantum mechanics. For a system of electrons and nuclei, the time-independent form of the Schrödinger equation is

$$H\Phi(\mathbf{r},\sigma,\mathbf{R}) = E\Phi(\mathbf{r},\sigma,\mathbf{R}), \tag{3.1}$$

where H is the total (non-relativistic) Hamiltonian, $\Phi(\mathbf{r},\sigma,\mathbf{R})$ is the eigenstate wavefunction, $\mathbf{r}$ denotes the positions of electrons, σ is a composite symbol for the spins of the electrons, and $\mathbf{R}$ denotes the positions of nuclei, and E is the eigenstate energy. In following part, the spin symbol σ is suppressed and will only be expressed explicitly when spin states become relevant. The Hamiltonian contains all the interactions and can be written as

$$H = T_{\mathrm{e}} + T_{\mathrm{n}} + V_{\mathrm{nn}} + V_{\mathrm{ee}} + V_{\mathrm{ne}}, \tag{3.2}$$

where T_{e} is the kinetic energy operator for electrons,

$$T_{\mathrm{e}} = -\sum_i \frac{\hbar^2}{2m_e}\frac{\partial^2}{\partial\mathbf{r}_i^2}, \tag{3.3}$$

T_{n} is the kinetic energy operator for nuclei,

$$T_{\mathrm{n}} = -\sum_{l} \frac{\hbar^2}{2M_l} \frac{\partial^2}{\partial \mathbf{R}_l^2}, \tag{3.4}$$

V_{nn} is the nucleus-nucleus interaction and can be written as

$$V_{\mathrm{nn}} = \frac{1}{2} \sum_{l,l',l\neq l'} \frac{e^2}{4\pi\epsilon_0} \frac{Z_l Z_{l'}}{|\mathbf{R}_l - \mathbf{R}_{l'}|}, \tag{3.5}$$

V_{ee} is the electron-electron interaction,

$$V_{\mathrm{ee}} = \frac{1}{2} \sum_{i,j,i\neq j} \frac{1}{4\pi\epsilon_0} \frac{e^2}{|\mathbf{r}_i - \mathbf{r}_j|}, \tag{3.6}$$

and V_{en} is the electron-nuclei interaction,

$$V_{\mathrm{en}} = -\sum_{i,l} \frac{Z_l}{4\pi\epsilon_0} \frac{e^2}{|\mathbf{R}_l - \mathbf{r}_i|}, \tag{3.7}$$

where $\mathbf{r}_i$ denotes the position of an electron i, $\mathbf{R}_l$ the position of a nucleus l, m_e the electronic mass, M_l the ionic mass and $Z_l e$ the ionic charge of nucleus l.

Finding the solution of the time-independent Schrödinger equation for the entire system is a formidable task. The Born-Oppenheimer (BO) approximation [96] allows us to treat electrons and nuclei as nearly independent entities, considerably simplifying the procedure for solving the Schrödinger equation. This approximation is justified by the fact that the nuclei, being much (10^3-10^5 times) heavier than electrons, move much more slowly than electrons. As a result, the electrons adjust quickly to the motions of ions. When solving the electronic problem, one can thus assume that the nuclei are fixed at their instantaneous configuration, and the electrons will quickly adjust (adiabatically) and stay at their ground state for that particular instantaneous configuration of nuclei. Within the BO approximation, the total wavefunction can be decomposed as

$$\Phi(\mathbf{R},\mathbf{r}) = \chi_n(\mathbf{R})\psi_e(\mathbf{R},\mathbf{r}), \tag{3.8}$$

where $\psi_e(\mathbf{R},\mathbf{r})$ represents the many-body electron wavefunction and satisfies the Schrödinger equation with nuclei at fixed positions $\mathbf{R}$,

$$\left[T_\mathrm{e} + V_\mathrm{ee}(\mathbf{r}) + V_\mathrm{en}(\mathbf{r},\mathbf{R})\right]\psi_e(\mathbf{R},\mathbf{r}) = E_\mathrm{e}\psi_\mathrm{e}(\mathbf{R},\mathbf{r}), \tag{3.9}$$

where E_e is the energy of electrons for nuclei frozen at positions $\mathbf{R}$. $\chi_n(\mathbf{R})$ satisfies following Schrödinger equation,

$$\left[T_\mathrm{n} + V_\mathrm{nn}(\mathbf{R}) + E_\mathrm{e}(\mathbf{R})\right]\chi_\mathrm{n}(\mathbf{R}) = E\chi_\mathrm{n}(\mathbf{R}). \tag{3.10}$$

From above equation, it is clear that the binding of nuclei is provided by $E_\mathrm{e}(\mathbf{R})$, as the nucleus-nucleus interaction $V_\mathrm{nn}(\mathbf{R})$ is repulsive. Thus, electrons form a “glue” that holds ions together.

The BO approximation is a good approximation for semiconductors and insulators with (large) band gaps. In these materials, typical phonon energies are of the oder of 0.01 eV, which is not large enough to excite electrons to states of higher energies. On the other hand, in metallic materials, the gap is zero and phenomena beyond BO approximation (such as phonon-mediated superconductivity) may occur [97]. Therefore, one has to be very careful when simulating metallic system with the BO approximation.

3.2.2 Hartree-Fock method

The BO approximation allows the decoupling of electronic motions from the ionic motions. However, the solution of Eq. 3.9 is still a challenging problem due to the large number of electrons as well as complicated geometry of many systems. A variety of approaches have been developed to obtain approximate solutions of Eq. 3.9. The simplest one is the Hartree approximation [98] in which the ground state wavefunction ψ_{H} is assumed to be a product of single-particle functions,

$$\psi_{\mathrm{H}}(\mathbf{r}) = \psi_1(\mathbf{r}_1)\psi_2(\mathbf{r}_2)\cdots\psi_N(\mathbf{r}_N), \tag{3.11}$$

where $\psi_i(\mathbf{r}_i)$ denotes the wavefunction of a single electron i and satisfies the orthonormal condition. The variational principle states that the exception value of the energy

$$E = \langle\psi_{\mathrm{H}}|\, H_{\mathrm{e}}\, |\psi_{\mathrm{H}}\rangle \leq E_0, \tag{3.12}$$

where E is the energy of electrons (the subscript "e" in Eq. 3.9 is dropped for simplicity in following discussions) and E_0 is the ground-state energy. Substituting Eq. 3.11 into Eq. 3.12, leads to

$$\begin{aligned} E = &-\sum_i \int \psi_i^* \frac{\hbar^2}{2m_e}\nabla_i^2\psi_i \mathrm{d}\mathbf{r}_i - \frac{1}{4\pi\epsilon_0}\sum_i\sum_l \int \psi_i^* \frac{e^2 Z}{|\mathbf{r}_i - \mathbf{R}_l|}\psi_i \mathrm{d}\mathbf{r}_i \\ &+ \frac{1}{8\pi\epsilon_0}\sum_i\sum_{j\neq i}\int \psi_i^*\psi_j^* \frac{e^2}{|\mathbf{r}_i - \mathbf{r}_j|}\psi_i\psi_j \mathrm{d}\mathbf{r}_i \mathrm{d}\mathbf{r}_j. \end{aligned} \tag{3.13}$$

The wavefunction ψ_i is varied to minimize E under the constraint $\int \psi_i^*\psi_i \mathrm{d}\mathbf{r}_i = 1$. This can be done using Lagrange multiplier method through minimizing

$$E - \sum_i \varepsilon_i \left[\int \psi_i^*\psi_i d\mathbf{r} - 1\right], \tag{3.14}$$

which is equivalent to solve

$$\frac{\delta E}{\delta\psi_i^*} - \varepsilon_i\psi_i = 0. \tag{3.15}$$

Taking the functional derivative of E, we get

$$-\frac{\hbar^2}{2m_e}\nabla_i^2\psi_i - \frac{1}{4\pi\epsilon_0}\sum_l \frac{e^2 Z}{|\mathbf{r}_i - \mathbf{R}_l|}\psi_i + \frac{1}{4\pi\epsilon_0}\sum_{j\neq i}\int \psi_i \frac{e^2 |\psi_j|^2}{|\mathbf{r}_i - \mathbf{r}_j|}\mathrm{d}\mathbf{r}_j = \varepsilon_i\psi_i. \tag{3.16}$$

The Hartree potential is defined as

$$v_{\mathrm{H}}(\mathbf{r}_i) = \frac{1}{4\pi\epsilon_0}\sum_{j\neq i}\int \frac{e^2 |\psi_j|^2}{|\mathbf{r}_i - \mathbf{r}_j|}\mathrm{d}\mathbf{r}_j. \tag{3.17}$$

and the potential from the nuclei is defined as

$$v_{\mathrm{n}}(\mathbf{r}_i) = -\frac{1}{4\pi\epsilon_0}\sum_l \frac{Ze^2}{|\mathbf{r}_i - \mathbf{R}_j|}. \tag{3.18}$$

We can rewrite Hartree potential as

$$\begin{aligned} v_{\mathrm{H}}(\mathbf{r}_i) &= \frac{1}{4\pi\epsilon_0}\int\int\sum_{j\neq i}\frac{e^2 |\psi_j|^2}{|\mathbf{r}_i - \mathbf{r}|}\delta(\mathbf{r}-\mathbf{r}_j)\mathrm{d}\mathbf{r}\mathrm{d}\mathbf{r}_j & (3.19)\\ &= \frac{1}{4\pi\epsilon_0}\int \frac{e^2}{|\mathbf{r}_i - \mathbf{r}|}\mathrm{d}\mathbf{r}\sum_{j\neq i}|\psi_j|^2. & (3.20)\end{aligned}$$

Therefore, the Hartree potential is the average electrostatic potential created by the rest of the electrons. For a system with a large number of electrons, v_{H} can be approximated by

$$v_{\mathrm{H}}(\mathbf{r}) = \frac{1}{4\pi\epsilon_0}\int \frac{e^2 n(\mathbf{r}')}{|\mathbf{r} - \mathbf{r}'|}\mathrm{d}\mathbf{r}. \tag{3.21}$$

Thus, the Hartree equation can be written as

$$\left[-\frac{\hbar^2}{2m_e}\nabla^2 + v_{\mathrm{n}}(\mathbf{r}) + v_{\mathrm{H}}(\mathbf{r})\right]\psi_i(\mathbf{r}) = \varepsilon_i\psi_i(\mathbf{r}). \tag{3.22}$$

Above equation is similar to the Schrödinger's equation for a single electron moving in a potential $v_{\mathrm{n}}(\mathbf{r}) + v_{\mathrm{H}}(\mathbf{r})$. The Hartree approximation therefore reduces the many-electron problem to one-electron problem.

There are two problems with the Hartree method. First, it neglects the correlations between electrons due to the Coulomb repulsion between electrons: electrons try to avoid each other as soon as possible. However, in Hartree approximation, electrons move independently. Second, the electronic wavefunction should be antisymmetric as electrons are fermions. The Hartree wavefunction (Eq. 3.11) violates the antisymmetry requirement. The second issue is resolved by using the Slater determinant as the many-electron wavefunction. The determinantal form of the wavefunction

$$\psi(\mathbf{r}_1, \mathbf{r}_2, \cdots, \mathbf{r}_N) = \frac{1}{\sqrt{N!}} \begin{vmatrix} \psi_1(\mathbf{r}_1) & \psi_1(\mathbf{r}_1) & \cdots & \psi_N(\mathbf{r}_1) \\ \psi_2(\mathbf{r}_1) & \psi_2(\mathbf{r}_2) & \cdots & \psi_N(\mathbf{r}_2) \\ \vdots & \vdots & \ddots & \vdots \\ \psi_N(\mathbf{r}_1) & \psi_N(\mathbf{r}_N) & \cdots & \psi_N(\mathbf{r}_N) \end{vmatrix} \tag{3.23}$$

is antisymmetric with respect to exchange of two electrons. Submitting the Slater determinant into Eq. 3.12 gives:

$$\begin{aligned} E =& \sum_i \int \psi_i^*(\mathbf{r}_i) \left[-\frac{\hbar^2}{2m_e} \nabla_i^2 - \sum_{il} \frac{Ze^2}{|\mathbf{r}_i - \mathbf{R}_l|} \psi_i(\mathbf{r}_i) \right] d\mathbf{r}_i \\ &+ \frac{1}{2} \sum_i \sum_{i \neq j} \int \int \frac{1}{4\pi\epsilon_0} \frac{e^2 \psi_i(\mathbf{r}_i)^2 \psi_i(\mathbf{r}_j)^2}{|\mathbf{r}_i - \mathbf{r}_j|} d\mathbf{r}_i d\mathbf{r}_j \\ &- \frac{1}{2} \sum_{i,j} \sum_{j \neq i} \int \int \frac{1}{4\pi\epsilon_0} \frac{e^2 \psi_j^*(\mathbf{r}_i) \psi_i^*(\mathbf{r}_j) \psi_i(\mathbf{r}_i) \psi_j(\mathbf{r}_j)}{|\mathbf{r}_i - \mathbf{r}_j|} d\mathbf{r}_i d\mathbf{r}_j. \end{aligned} \tag{3.24}$$

Comparing to Eq. 3.11 in Hartree approximation, Eq 3.24 has an extra energy term (last term) known as exchange energy arising from the Pauli Exclusion Principle. The exchange energy is non-zero only for parallel spins. As in the Hartree's case, minimizing E under the constraint of $\int \psi_i^*(\mathbf{r}_i)\psi_i(\mathbf{r}_i)d\mathbf{r}_i = 1$ gives the Hartree-Fock equation written as

$$\left[\frac{\hbar^2}{2m_e}\nabla_i^2 + v_{\mathrm{n}} + v_{\mathrm{H}}\right] - \int \sum_{j\neq i} \frac{1}{4\pi\epsilon_0}\frac{e^2}{|\mathbf{r}-\mathbf{r}'|}\psi_j(\mathbf{r}')^*\psi_i(\mathbf{r}')d\mathbf{r}'\psi_j(\mathbf{r}) = \varepsilon_i\psi_i(\mathbf{r}). \tag{3.25}$$

The Hartree-Fock is a mean-field theory: each electron moves in an average field generated by other electrons. The presence of exchange energy does include some correlations between the parallel spins.

3.2.3 Density functional theory

3.2.3.1 Hohenberg-Kohn theorems

The many-body wavefunction depends on the coordinates of all the electrons, making it a function of $3N$ variables, where N is the number of electrons. This makes the solution of the Schödinger equation numerically demanding as the system becomes larger. The first attempt to describe electronic systems in terms of $n(\mathbf{r})$, a function of only three variables, was made by Thomas and Fermi (Thomas-Fermi model) [99, 100]. Although Thomas-Fermi theory for homogenous electron gas is a very approximate theory, it contains the seeds for the development of modern density functional theory (DFT). In 1964, Hohenberg and Kohn proved two theorems [101, 102] that laid the foundation of the DFT:

Theorem 1. *The external potential $v(\mathbf{r})$ is a unique functional of the electron density $n(\mathbf{r})$. As a result, the total ground-state energy E of any many-electron system is also a unique functional of $n(\mathbf{r})$.*

Theorem 2. *The functional $E[n]$ for the total energy has a minimum equal to the ground-state energy at the ground-state density.*

To start, we first show that the expectation value of the electron-nuclei interaction V_{en} can be written as a functional of electron density. Recall that the Hamiltonian for interacting inhomogeneous electron gas is

$$H = T_\mathrm{e} + V_\mathrm{ee} + V_\mathrm{en}, \tag{3.26}$$

where

$$V_\mathrm{en} = -\sum_{i,l} \frac{Z_l}{4\pi\epsilon_0} \frac{e^2}{|\mathbf{R}_l - \mathbf{r}_i|} = \sum_i v(\mathbf{r}_i). \tag{3.27}$$

Introducing the electron density operator as

$$\hat{n}(\mathbf{r}) = \sum_i^N \delta(\mathbf{r} - \mathbf{r}_i), \tag{3.28}$$

the electron density is then

$$n(\mathbf{r}) = \langle\psi|\, \hat{n}(\mathbf{r})\, |\psi\rangle = \int \psi^* \hat{n}(\mathbf{r}) \psi d\mathbf{r}_1 \cdots d\mathbf{r}_N \tag{3.29}$$

Then $\langle\psi|\, V_\mathrm{en}\, |\psi\rangle$ can therefore be written as

$$\begin{aligned}
\langle\psi|\, V_\mathrm{en}\, |\psi\rangle &= \int \psi^* \sum_i v(\mathbf{r}_i) \psi d\mathbf{r}_1 \cdots d\mathbf{r}_N \\
&= \int \psi^* \sum_i v(\mathbf{r}) \delta(\mathbf{r} - \mathbf{r}_i) \psi d\mathbf{r}_1 \cdots d\mathbf{r}_N d\mathbf{r} \\
&= \int \psi^* v(\mathbf{r}) \hat{n}(\mathbf{r}) \psi d\mathbf{r}_1 \cdots d\mathbf{r}_N d\mathbf{r} \\
&= \int v(\mathbf{r}) n(\mathbf{r}) d\mathbf{r}.
\end{aligned} \tag{3.30}$$

Proof. The first theorem is proved by contradiction. One can assume there are two different potentials $v(\mathbf{r})$ and $v'(\mathbf{r})$ with ground state ψ and ψ' producing the same density $n(\mathbf{r})$. For simplicity, the ground state is assumed to be nondegenerate. Denote the Hamiltonians and ground-state energies associated with ψ and ψ', H and H', and E and E'. Based on the variational principle, we have

$$E = \langle\psi| H |\psi\rangle < \langle\psi'| H |\psi'\rangle . \tag{3.31}$$

Then

$$\begin{aligned} E < \langle\psi'| H |\psi'\rangle &= \langle\psi'| H + H' - H' |\psi'\rangle \\ &= \langle\psi'| H' |\psi'\rangle + \langle\psi'| H - H' |\psi'\rangle \\ &= E' + \langle\psi'| V - V' |\psi'\rangle \\ &= E' + \int (v(\mathbf{r}) - v'(\mathbf{r}))n(\mathbf{r})d\mathbf{r}. \end{aligned} \tag{3.32}$$

Similarly, starting with

$$E' = \langle\psi'| H' |\psi'\rangle < \langle\psi| H' |\psi\rangle \tag{3.33}$$

will lead to

$$E' = E + \int (v'(\mathbf{r}) - v(\mathbf{r}))n(\mathbf{r})d\mathbf{r}. \tag{3.34}$$

Adding Eq. 3.32 and Eq. 3.33, we get

$$E + E' < E + E', \tag{3.35}$$

which is clearly absurd. Therefore, the initial assumption must be false and hence the ground-state electron density determines $v(\mathbf{r})$ uniquely, proving Theorem 1. It follows directly that the ground-state electron density is produced by a unique H, which further determines the nondegenerate ground state of the system. Putting all these altogether, $n(\mathbf{r})$ determines the ground-state wavefunction uniquely and consequently the ground-state energy. $\square$

Proof. We start by writing the ground-state energy $E[n(\mathbf{r})]$ as

$$\begin{aligned} E[n(\mathbf{r})] &= \langle\psi| V |\psi\rangle + \langle\psi| T + V_{\text{ee}} |\psi\rangle \\ &= \int v(\mathbf{r})n(\mathbf{r})d\mathbf{r} + F[n(\mathbf{r})]. \end{aligned} \tag{3.36}$$

It is evident $F = \langle\psi| T + V_{\text{ee}} |\psi\rangle$ is a functional of $n(\mathbf{r})$ as ψ is a functional of $n(\mathbf{r})$. Assuming a changed electron density $n'(\mathbf{r})$ under the same potential $v(\mathbf{r})$, then the energy functional is

$$E[n'(\mathbf{r})] = \int v(\mathbf{r})n'(\mathbf{r})d\mathbf{r} + F[n'(\mathbf{r})]. \tag{3.37}$$

We know from the variational principle that for the state ψ' associated with $n'(\mathbf{r})$,

$$E[\psi] < E[\psi']. \tag{3.38}$$

As proved in Theorem 1, $E[\psi'] = E[n'(\mathbf{r})]$ and $E[\psi] = E[n(\mathbf{r})]$, therefore

$$E[n(\mathbf{r})] < E[n'(\mathbf{r})], \tag{3.39}$$

proofing Theorem 2. ☐

3.2.3.2 Kohn-Sham equations

The functional $F[n]$ defined in last section can be decomposed into three parts

$$F[n] = T_s[n] + \frac{e^2}{2}\int\int \frac{1}{4\pi\epsilon_0}\frac{n(\mathbf{r})n(\mathbf{r}')}{|\mathbf{r}-\mathbf{r}'|}d\mathbf{r}d\mathbf{r}' + E_{\text{xc}}[n], \tag{3.40}$$

where $T_s[n]$ is the kinetic energy of noninteracting electron gas of density $n(\mathbf{r})$ at its ground state, the second term is the classical Coulomb energy, and the third term $E_{\text{xc}}[n]$ is the exchange-correlation energy. The total energy functional is then

$$E[n] = \int v(\mathbf{r}) n(\mathbf{r}) d\mathbf{r} + F[n]. \tag{3.41}$$

Again, one has to minimize the energy subjecting to the constraint $\int n(\mathbf{r}) d\mathbf{r} = N$. This gives

$$\frac{\delta E[n]}{\delta n(\mathbf{r})} - \mu = 0, \tag{3.42}$$

or equivalently

$$\frac{\delta T_s[n]}{\delta n(\mathbf{r})} + v(\mathbf{r}) + \int \frac{e^2}{4\pi\epsilon_0} \frac{n(\mathbf{r}')}{|\mathbf{r}-\mathbf{r}'|} d\mathbf{r}' + \frac{\delta E_{\mathrm{xc}}[n]}{\delta n(\mathbf{r})} - \mu = 0, \tag{3.43}$$

where μ is the Lagrange multiplier. By defining

$$v_{\mathrm{H}}(\mathbf{r}) = \int \frac{e^2}{4\pi\epsilon_0} \frac{n(\mathbf{r}')}{|\mathbf{r}-\mathbf{r}'|} d\mathbf{r}' \tag{3.44}$$

and

$$v_{\mathrm{xc}}(\mathbf{r}) = \frac{\delta E_{\mathrm{xc}}[n]}{\delta n(\mathbf{r})} \tag{3.45}$$

we obtain

$$\frac{\delta T_s[n]}{\delta n(\mathbf{r})} + v(\mathbf{r}) + v_{\mathrm{H}}(\mathbf{r}) + v_{\mathrm{xc}}(\mathbf{r}) - \mu = 0. \tag{3.46}$$

However, in Eq. 3.46, neither functional $T_s[n]$ nor $v_{\mathrm{xc}}(\mathbf{r})$ is known. Kohn and Sham introduced orbitals (KS orbitals) into DFT by defining

$$n(\mathbf{r}) = \sum_i^N \left|\psi_i^{\mathrm{KS}}(\mathbf{r})\right|^2, \tag{3.47}$$

and an effective potential $v_{\text{eff}}(\mathbf{r})$

$$v_{\text{eff}}(\mathbf{r}) = v(\mathbf{r}) + v_{\text{H}}(\mathbf{r}) + v_{\text{xc}}(\mathbf{r}). \tag{3.48}$$

Substituting Eqs. 3.47 and 3.48 into Eq. 3.46 then leads to the Kohn-Sham equation:

$$\left[-\frac{\hbar^2}{2m_e}\nabla^2 + v_{\text{eff}}(\mathbf{r})\right]\psi_i^{\text{KS}}(\mathbf{r}) = \varepsilon_i^{\text{KS}}\psi_i^{\text{KS}}(\mathbf{r}). \tag{3.49}$$

The most important idea of the KS equation is to map an interacting many-electron system onto an auxiliary non-interacting system of independent particles, which has the same density as the original system. The particles each move independently in an effective potential $v_{\text{eff}}(\mathbf{r})$. This one-electron approximation is similar to Hartree and HF method. However, the KS equation includes the effects of exchange and correlation through $v_{\text{xc}}(\mathbf{r})$. It is noted that the exchange-correlation potential is an unknown function and approximations have to be made in order to solve the KS equation. The total energy can be expressed in terms of $\varepsilon_i^{\text{KS}}$ as

$$E = \sum_i \varepsilon_i^{\text{KS}} - \frac{e^2}{2}\int\int \frac{1}{4\pi\epsilon_0}\frac{n(\mathbf{r})n(\mathbf{r}')}{|\mathbf{r}-\mathbf{r}'|}d\mathbf{r}d\mathbf{r}' + E_{\text{xc}}[n] - \int v_{\text{xc}}(\mathbf{r})n(\mathbf{r})d\mathbf{r}. \tag{3.50}$$

3.2.3.3 Local density approxiamtion

In practice, the exchange-correlation energy functional must be approximated as the exact form is unknown. The first such approximation was developed by Kohn and Sham in 1965 and is known as LDA (local density approximation) [102]. It is assumed that the electron density $n(\mathbf{r})$ varies slowly in space, and the electron gas within a small volume could be considered locally homogenous. Thus, the local exchange-correlation energy could be calculated (at the lowest approximation) as a product of the small volume and the exchange-correlation energy density from the homogenous electron gas theory. The total exchange-correlation energy is then

$$E_{\mathrm{xc}}[n] = \int \varepsilon_{\mathrm{xc}}[n(\mathbf{r})]n(\mathbf{r})d\mathbf{r}, \tag{3.51}$$

where $\varepsilon_{\mathrm{xc}}[n(\mathbf{r})]$ is the exchange-correlation energy density from Thomas-Fermi model. The $v_{\mathrm{xc}}(\mathbf{r})$ can then be found by taking the functional derivation of $E_{\mathrm{xc}}[n]$,

$$v_{\mathrm{xc}}(\mathbf{r}) = \frac{\delta E_{\mathrm{xc}}[n]}{\delta n(\mathbf{r})} = \frac{d\left(\varepsilon_{\mathrm{xc}}[n(\mathbf{r})]n(\mathbf{r})\right)}{dn} = \mu_{\mathrm{xc}}[n(\mathbf{r})]. \tag{3.52}$$

The total energy in LDA approximation can now be written as

$$E = \sum_i \varepsilon_i - \frac{e^2}{2}\int\int \frac{1}{4\pi\epsilon_0}\frac{n(\mathbf{r})n(\mathbf{r}')}{|\mathbf{r}-\mathbf{r}'|}d\mathbf{r}d\mathbf{r}' + \int (\varepsilon_{\mathrm{xc}}[n(\mathbf{r})] - \mu_{\mathrm{xc}}[n(\mathbf{r})])n(\mathbf{r})d\mathbf{r}. \tag{3.53}$$

The exchange energy in LDA has a very simple form

$$E_{\mathrm{x}}^{\mathrm{LDA}} = \int d^3r\; n(\mathbf{r})\varepsilon_{\mathrm{x}}^{\mathrm{unif}}[n(\mathbf{r})], \tag{3.54}$$

where

$$\varepsilon_{\mathrm{x}}^{\mathrm{unif}} = -0.75(\frac{3}{\pi})^{\frac{1}{3}}n(\mathbf{r})^{1/3} = A_{\mathrm{x}}n(\mathbf{r})^{1/3}. \tag{3.55}$$

The correlation energy density ($\varepsilon_{\mathrm{c}}^{\mathrm{unif}}$) in LDA is more complicated as the exact analytical form are known only in extreme limits for homogenous electron gas. An expression that recover both high-density and low-density limits is given by Perdew and Wang [103], with parameters fitted to accurate Quantum Monte Carlo correlation energies.

The LDA has been generalized to the ground state of magnetic systems. The electron density is now equal to the sum of spin-up density $n_\uparrow(\mathbf{r})$ and spin-down density $n_\downarrow(\mathbf{r})$. The exchange-correlation function becomes a functional of $n_\uparrow(\mathbf{r})$ and $n_\downarrow(\mathbf{r})$. The spin-dependent KS equation reads

$$\left[-\frac{\hbar^2}{2m_e}\nabla^2 + v_{\text{eff}}^{\sigma}\right]\psi_{i\sigma}^{\text{KS}}(\mathbf{r}) = \varepsilon_{i\sigma}\psi_{i\sigma}^{\text{KS}}(\mathbf{r}), \tag{3.56}$$

where

$$v_{\text{eff}}^{\sigma} = v(\mathbf{r}) - \sigma\mu_B B(\mathbf{r}) + \frac{e^2}{4\pi\epsilon_0}\int \frac{n'(\mathbf{r})}{|\mathbf{r}-\mathbf{r}'|}d\mathbf{r}' + \frac{\delta E_{\text{xc}}[n_\uparrow(\mathbf{r}), n_\downarrow(\mathbf{r})]}{\delta n_\sigma(\mathbf{r})}\ [\sigma = \pm 1] \tag{3.57}$$

and

$$n_\sigma(\mathbf{r}) = \sum_{\text{occupied}} |\psi_{i\sigma}|^2 \tag{3.58}$$

3.2.3.4 Non-local approximation

It was argued that one can improve $E_{\text{xc}}[n]$ by expanding it in terms of gradient of the density and truncated it at some order. This is known as gradient expansion approximation (GEA) [102, 104]. The general form is

$$E_{\text{xc}}^{\text{GEA}} = E_{\text{xc}}^{\text{LDA}} + \int B_{\text{xc}}(n, \nabla n)d\mathbf{r}. \tag{3.59}$$

However, this recipe did not provide improvement over LDA. A breakthrough in DFT is represented by the following proposition of Perdew and Wang:

$$E_{\text{xc}}^{\text{PW91}} = \int f(n_\uparrow(\mathbf{r}), n_\downarrow(\mathbf{r}), \nabla n_\uparrow(\mathbf{r}), \nabla n_\downarrow(\mathbf{r}))d\mathbf{r}, \tag{3.60}$$

where f is a functional of density and its gradient [103, 105]. Later on, Perdew et al. [106] proposed another functional, PBE, which retains important features of PW91 while stratifying some exact properties (e.g., spin-scaling relation, uniform coordinate scaling and

Lieb–Oxford bound). The PBE exchange energy is expressed as

$$E_{\mathrm{x}} = \int d^3r\; n(\mathbf{r})\epsilon_{\mathrm{x}}^{\mathrm{unif}}(n(\mathbf{r}))F_{\mathrm{x}}(s), \tag{3.61}$$

where

$$F_{\mathrm{x}}(s) = 1 + \kappa - \frac{\kappa}{1 + \mu s^2/\kappa}\,, \tag{3.62}$$

$\kappa = 0.804$, $\mu = 0.235$, $s = |\nabla n|/2\pi k_F$, and $k_F = (3\pi n)^{1/3}$ is called the Fermi wavevector. The PBE correlation energy has the form

$$E_{\mathrm{c}}^{\mathrm{PBE}} = \int d^3r\; n[\epsilon_{\mathrm{c}}^{\mathrm{unif}}(n) + H(r_s, \xi, t)], \tag{3.63}$$

where

$$H(r_s, \xi, t) = \frac{e^2}{a_0}\gamma\phi^3 \ln\left[1 + \frac{\beta}{\gamma}t^2\left(\frac{1 + At^2}{1 + At^2 + A^2t^4}\right)\right], \tag{3.64}$$

$r_s = (3/4\pi n)^{1/3}$ is the local Seitz radius, $\xi = (n_\uparrow(\mathbf{r}) - n_\downarrow(\mathbf{r}))/n$ is the relative spin polarization, $t = |\nabla n|/(2\phi k_s n)$, $a_0 = \hbar^2/(m_e e^2)$, $\gamma = (1 - \ln 2)/\pi^2 = 0.031091$, $\beta = 0.066725$, $\phi(\xi) = [(1+\xi)^{2/3} + (1-\xi)^{2/3}]/2$ is a spin-scaling factor, $k_s = \sqrt{4k_F/(\pi a_0)}$, and

$$A = \frac{\beta}{\gamma}\left[\exp\left[\frac{-\epsilon_{\mathrm{c}}^{\mathrm{unif}}}{\gamma\phi^3 e^2/a_0}\right] - 1\right]^{-1}. \tag{3.65}$$

3.2.4 Bloch's theorem

For a periodic solid, the potential $v_{\text{eff}}(\mathbf{r})$ is also periodic,

$$v_{\text{eff}}(\mathbf{r}) = v_{\text{eff}}(\mathbf{r} + \mathbf{R}). \tag{3.66}$$

The solutions of the single-particle in the Schrödinger equation (or KS equation) in a periodic potential $v_{\text{eff}}(\mathbf{r})$ have a simple form which is known as Bloch's theorem. It states that the wave functions at points separated by a lattice vector $\mathbf{R}$ are connected with following relation,

$$\psi_{\mathbf{k}}(\mathbf{r}+\mathbf{R}) = \exp(i\mathbf{k}\cdot\mathbf{R})\psi_{\mathbf{k}}(\mathbf{r}). \tag{3.67}$$

Following that, it is easy to see that the wave function should have a form

$$\psi_{\mathbf{k}}(\mathbf{r}) = e^{i\mathbf{k}\cdot\mathbf{r}}u_{\mathbf{k}}(\mathbf{r}), \tag{3.68}$$

where $u_{\mathbf{k}}(\mathbf{r})$ is a periodic function with $u_{\mathbf{k}}(\mathbf{r}) = u_{\mathbf{k}}(\mathbf{r}+\mathbf{R})$. The vector $\mathbf{k}$ is a good quantum number for a periodic system; the wave function and energy eigenvalues of an electron in a periodic solid can be labeled by $\mathbf{k}$. If $\mathbf{k}$ satisfies the Bloch's theorem, $\mathbf{k}+\mathbf{G}$ also satisfies the Bloch theorem, where $\mathbf{G}$ is a reciprocal lattice vector. Therefore, all possible values of $\mathbf{k}$ can be confined to the unit cell of the reciprocal lattice, the first Brillouin zone. For each $\mathbf{k}$, there are serval energy eigenvalues that are labeled as $\varepsilon_{n\mathbf{k}}$ where n is called the band index. The band structure is a plot of $\varepsilon_{n\mathbf{k}}$ versus $\mathbf{k}$.

3.2.5 Plane wave expansion method

The periodic function $u_{n,\mathbf{k}}(\mathbf{r})$ can be expanded in a Fourier series:

$$u_{n,\mathbf{k}}(\mathbf{r}) = \sum_{m} c_{n,m}(\mathbf{k})e^{i\mathbf{G}_m\cdot\mathbf{r}}. \tag{3.69}$$

Equivalently,

$$\psi_{n,\mathbf{k}}(\mathbf{r}) = \sum_{m} c_{n,m}(\mathbf{k})e^{i(\mathbf{k}+\mathbf{G}_m)\cdot\mathbf{r}}. \tag{3.70}$$

Let $\mathbf{q} = \mathbf{k}+\mathbf{G}_m$, we have Bloch states expressed as

$$\psi_{n,\mathbf{k}}(\mathbf{r}) = \sum_{\mathbf{q}} c_{n,\mathbf{q}}\left|\mathbf{q}\right\rangle. \tag{3.71}$$

From above equation, we can see that the Block state $\psi_{n,\mathbf{k}}(\mathbf{r})$ is a superposition of plane waves with $\mathbf{q}$ wave vectors differ by $\mathbf{G}$. The effective potential can also be expanded in a Fourier series:

$$v_{\text{eff}}(\mathbf{r}) = \sum_m v_{\text{eff}}(\mathbf{G}_m) e^{i\mathbf{G}_m \cdot \mathbf{r}} \tag{3.72}$$

The non-zero matrix elements are

$$\langle \mathbf{q}' | \, v_{\text{eff}}(\mathbf{r}) \, | \mathbf{q} \rangle = \sum_m v_{\text{eff}}(\mathbf{G}_m) \left\langle \mathbf{q}' \right| e^{i\mathbf{G}_m \cdot \mathbf{r}} \left| \mathbf{q} \right\rangle = \sum_m v_{\text{eff}}(\mathbf{G}_m) \delta_{\mathbf{q}'-\mathbf{q},\mathbf{G}_m}. \tag{3.73}$$

Substituting Eq. 3.72 into the KS equation, multiplying by $\langle \mathbf{q}' |$ from the left and integrating over $\mathbf{r}$ gives the secular equation ,

$$\left\langle \mathbf{q}' \middle| \left[-\frac{\hbar^2}{2m_e} \nabla^2 + v_{\text{eff}}(\mathbf{r}) \right] \sum_{\mathbf{q}} c_{n,m} \middle| \mathbf{q} \right\rangle = \left\langle \mathbf{q}' \middle| \varepsilon_n \sum_{\mathbf{q}} c_{n,m} \middle| \mathbf{q} \right\rangle \tag{3.74}$$

and

$$\sum_{m'} \left[\frac{\hbar^2}{2m_e} \left| \mathbf{k} + \mathbf{G}_m \right|^2 \delta_{m,m'} + v_{\text{eff}}(\mathbf{G}_m - \mathbf{G}'_m) \right] c_{n,m'} = \varepsilon_n c_{n,m}. \tag{3.75}$$

In this form, the kinetic energy is diagonal, and the effective potential is described in terms of Fourier transforms. The size of the matrix is determined by the choice of cutoff energy $\frac{\hbar^2}{2m_e} \left| \mathbf{k} + \mathbf{G}_c \right|$

3.2.6 The pseudopotential approximation

The Bloch's theorem indicates the wave function for electrons in a periodic potential can be expanded with a plane-wave basis set. However, a large number of plane waves are needed to expand the tightly bound core orbitals in order to reproduce the rapid oscillations of the wave functions of the valence electrons in the core region. The pseudopotential (PP) approximation replaces the core electrons with a weaker potential that acts on pseudo wave functions [107–113]. As depicted in Fig. 3.1, the Coulomb potential is very strong and approaches infinity near the origin, while the PP is close to zero. Consequently, the pseudo wave function is smooth and nodeless in the core region (Fig. 3.2), which requires a smaller number of plane waves for its expansion than needed for the true wave function. In the PP approximation, the core electrons are eliminated and therefore the core levels are assumed to be fully occupied and unchanged in all atomic environments. This is known as the frozen core approximation, which is justified by the fact that inner-shell electrons hardly participate in bonding and are less sensitive to the environment.

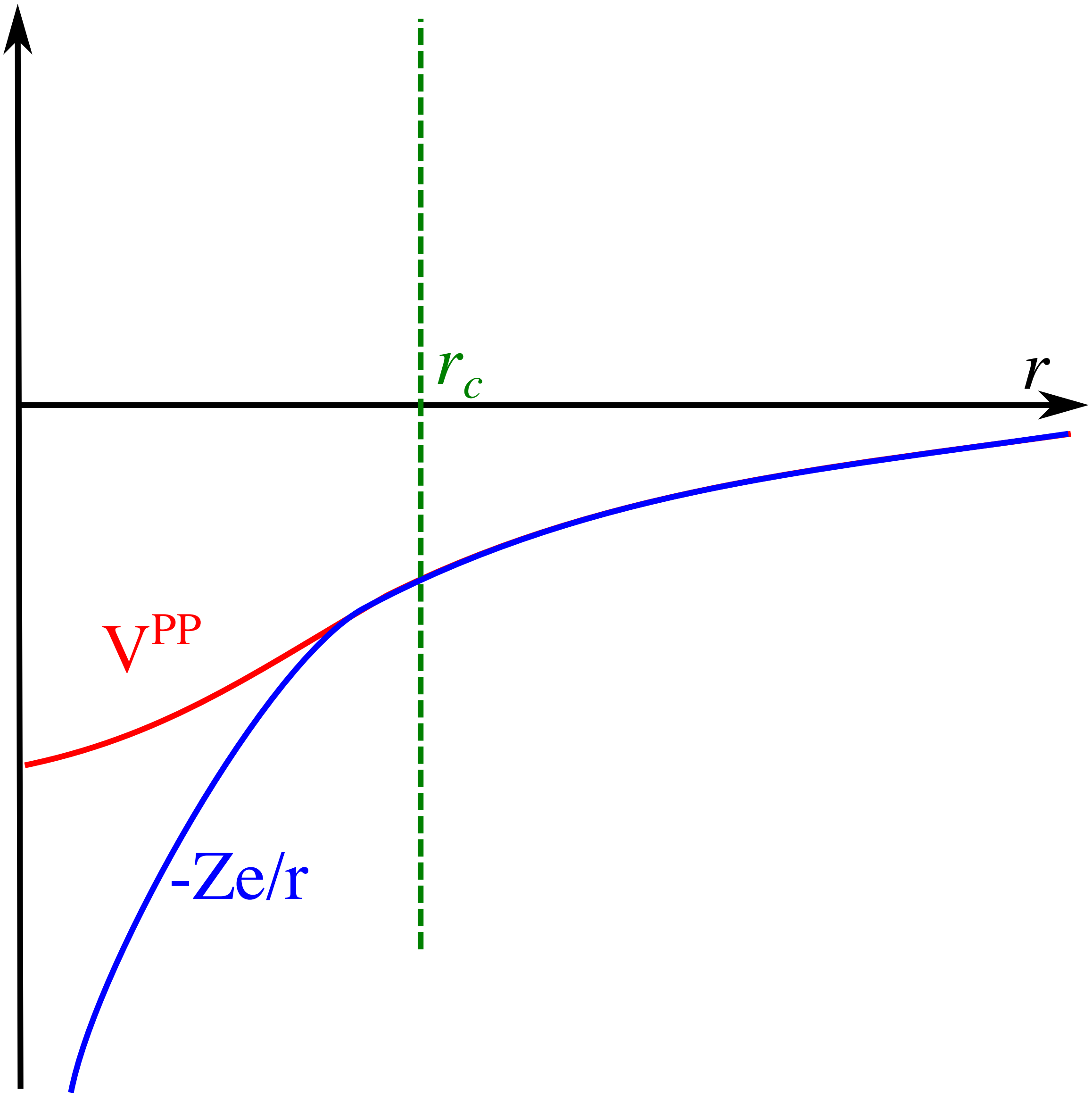

Figure 3.1: Schematic diagram of the relationship between all electron potential and pseudopotential

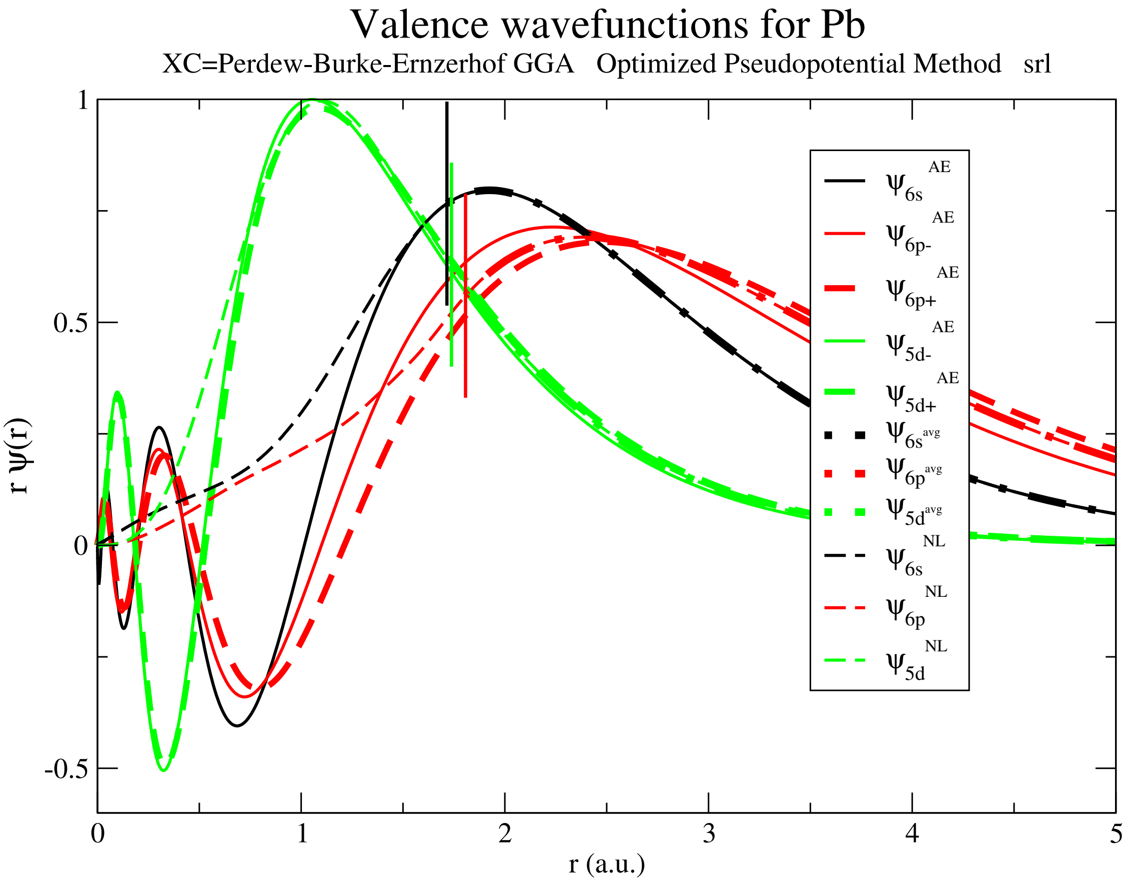

Figure 3.2: Comparison of pseudo and all-electron wave functions for Pb

We briefly discuss the main steps to construct PPs:

(1) True radial wave function for chosen reference configuration $R_l(r)$ is obtained by solving the radial KS equation:

$$\left[-\frac{1}{r}\frac{\hbar^2}{2m_e}\frac{d^2}{dr^2}r+\frac{\hbar^2}{2m_e}\frac{l(l+1)}{r^2}+v(r)\right]R_l(r)=\varepsilon_l R_l(r), \tag{3.76}$$

where

$$v(r)=-\frac{1}{4\pi\epsilon_0}\frac{e^2Z}{r}+v_{\mathrm{H}}(r)+\mu_{\mathrm{xc}}(r). \tag{3.77}$$

(2) The pseudo wave function $\phi_l^{\mathrm{PP}}(r)$ is constructed such that it satisfies following conditions [109]:

i. The $\phi_l^{\mathrm{PP}}(r)$ is nodeless.

ii. Beyond a suitably chosen cutoff radius r_c, the pseudo wave function $\phi_l^{\mathrm{PP}}(r)$ is equal to the true radial wave function $R_l(r)$:

$$\phi_l^{\mathrm{PP}}(r)=R_l(r), \text{for } r>r_c. \tag{3.78}$$

iii. The pseudo wave function $\phi_l^{\mathrm{PP}}(r)$ gives the same eigenvalues as the true wave function.

$$\varepsilon_l^{\mathrm{PP}}=\varepsilon_l. \tag{3.79}$$

iv. Norm-conservation: the charge enclosed within r_c for the $\phi_l^{\mathrm{PP}}(r)$ and true wave function $R_l(r)$ must be equal:

$$\int_0^{r_c}\left|\phi_l^{\mathrm{PP}}(r)\right|^2 r^2dr=\int_0^{r_c}\left|R_l(r)\right|^2 r^2dr. \tag{3.80}$$

A PP that fulfills this condition is called “norm-conserving pseudopotential” (NCPP) [109].

v. The logarithm derivatives of the real and pseudo wavefunction and their first energy derivatives agree for $r > r_c$. Note that properties (iv) and (v) are related through

$$-\frac{1}{2}\left[[rR(r)]^2 \frac{d}{d\varepsilon}\frac{d}{dr}\ln R(r)\right] = \int_0^R r^2 \left|R(r)\right|^2 dr. \tag{3.81}$$

that applies to each angular momentum l.

(3) The radial KS equation can be inverted to yield a screened potential that has the pseudo wave function as its eigenfunction with correct eigenvalue.

$$\left[-\frac{1}{r}\frac{\hbar^2}{2m_e}\frac{d^2 r\phi_l^{\mathrm{PP}}(r)}{dr^2} + \frac{\hbar^2}{2m_e}\frac{l(l+1)}{r^2}\phi_l^{\mathrm{PP}}(r) + w_l^{\mathrm{scr}}\phi_l^{\mathrm{PP}}(r)\right] = \varepsilon_l \phi_l^{\mathrm{PP}}(r). \tag{3.82}$$

The screened semi-local PP w_l^{scr} lacks the transferability as the screening of the valence electrons depends on the environment strongly. The transferability can be improved by removing the screening effects of the valence electrons (descreen),

$$w_l^{\mathrm{ps}}(r) = w_l^{\mathrm{scr}} - v_{\mathrm{H}}(r) - \mu_{xc}(r), \tag{3.83}$$

where

$$v_{\mathrm{H}}(r) = \int \frac{e^2}{4\pi\epsilon_0}\frac{n^v(r')}{|\mathbf{r}-\mathbf{r}'|}d\mathbf{r}', \tag{3.84}$$

and $\mu_{\mathrm{xc}}(r)$ is also calculated from $n^v(r')$, the valence electron density, estimated with

$$n^v(r') = \sum_{l,\mathrm{occupied}} \left|\phi_l^{\mathrm{PP}}(r)\right|^2. \tag{3.85}$$

When the atom is placed in a different environment, $v_{\mathrm{H}}(r)$ and $\mu_{\mathrm{xc}}(r)$ are recalculated and added to w_l^{scr}. The non-local (NL) PP in a solid-state calculation then takes the form of a sum over all angular momentum channels,

$$\hat{V}_{\mathrm{NL}}(\mathbf{r}) = \sum_l w_l^{\mathrm{ps}}(\mathbf{r})\mathbf{P}_l, \tag{3.86}$$

where $\mathbf{P}_l$ is the projector on the angular momentum state. Because the PP is angular-momentum-dependent, each angular momentum state l has its own potential that can be determined independently from the other potentials. It is therefore possible to use different reference configurations for different angular momenta. This allows the use of excited states or (partially) ionic states as reference states to construct the PP to improve the transferability.

As proposed by Kleinman and Bylander (KB) [114], the non-local PP can be represented in a semi-local form:

$$\hat{V}_{\mathrm{NL}} = V_{\mathrm{loc}}(r) + \sum_l \frac{|\Delta V_l(r) R_l^{\mathrm{ref}}\rangle \langle R_l^{\mathrm{ref}} \Delta V_l(r)|}{\left\langle R_l^{\mathrm{ref}} \right| \Delta V_l(r) \left| R_l^{\mathrm{ref}} \right\rangle}, \tag{3.87}$$

where $\Delta V_l(r) = w_l^{\mathrm{ps}}(r) - V_{\mathrm{loc}}(r)$ and $V_{\mathrm{loc}}(r)$ is arbitrary. The action of non-local potential on reference state is expressed as

$$\begin{aligned}\hat{V}_{\mathrm{NL}} |R_l^{\mathrm{ref}}\rangle &= V_{\mathrm{loc}}(r) |R_l^{\mathrm{ref}}\rangle + \sum_l \frac{|\Delta V_l(r) R_l^{\mathrm{ref}}\rangle \langle R_l^{\mathrm{ref}} \Delta V_l(r)| \, |R_l^{\mathrm{ref}}\rangle}{\left\langle R_l^{\mathrm{ref}} \right| \Delta V_l(r) \left| R_l^{\mathrm{ref}} \right\rangle} \\ &= \sum_l w_l^{\mathrm{ps}}(r) |R_l^{\mathrm{ref}}\rangle . \end{aligned} \tag{3.88}$$

Because the choice of $V_{\mathrm{loc}}(r)$ is arbitrary in the KB form, Ramer and Rappe [115] proposed to generate PPs with enhanced transferability by adding augmentation function $A(r)$ to local potential

$$\hat{V}_{\mathrm{NL}} = V_{\mathrm{loc}}(r) + A(r) + \sum_l \frac{|(\Delta V_l(r) - A(r)) R_l^{\mathrm{ref}}\rangle \langle R_l^{\mathrm{ref}} (\Delta V_l(r) - A(r))|}{\left\langle R_l^{\mathrm{ref}} \right| (\Delta V_l(r) - A(r)) \left| R_l^{\mathrm{ref}} \right\rangle}. \tag{3.89}$$

By adjusting $A(r)$, better transferability can be achieved.

Rappe et al. proposed to use the kinetic energy expansion as an optimization criterion in the construction of the PPs, based on the observation that the total energy and the kinetic energy have similar convergence properties [112]. For each l channel,the pseudo wave function within the cutoff $r_{c,l}$ is expressed in terms of Bessel functions,

$$\phi_l^{\mathrm{PP}}(r) = \sum_i^n c_i j_l(G_i r), \tag{3.90}$$

where $j_l(G_i r)$ are spherical Bessel functions with $i-1$ zeros at positions smaller than $r_{c,l}$. The value of G_i are fixed satisfying

$$\frac{j'(G_i r_{c,l})}{j(G_i r_{c,l})} = \frac{R_l'(r_{c,l})}{R_l(r_{c,l})}. \tag{3.91}$$

The values of a_i are determined such that:

i. $\phi_l^{\mathrm{PP}}(r)$ is normalized.

ii. First and second derivatives of $\phi_l^{\mathrm{PP}}(r)$ are continuous at $r_{c,l}$.

iii. $\Delta E_{\mathrm{kin}}(\{c_i\}, G_c)$ is minimal for

$$\Delta E_{\mathrm{kin}} = -\int \phi_l^{\mathrm{PP}}(r)^* \nabla^2 \phi_l^{\mathrm{PP}}(r) d\mathbf{r} - \int_0^{G_c} G^2 \left|\phi_l^{\mathrm{PP}}(G)\right|^2 dG, \tag{3.92}$$

where ΔE_{kin} is the kinetic energy contribution above a target cutoff value G_c. In practice, G_c is changed to minimize ΔE_{kin} to a small enough value.

3.3 Molecular dynamics

3.3.1 Equation of motion

Hamilton's variational principle summarizes most of classical mechanics, and has been extended to quantum mechanics and quantum field theory. It states that the trajectory of a mechanical system in the phase space has the time integral $\int \mathcal{L}dt$ at an extremum, where $\mathcal{L}$ is the Lagrangian. Given a set of N independent generalized coordinates and velocities $\{q_i, \dot{q}_i\}$, the Lagrangian $\mathcal{L}$ satisfies the Euler–Lagrange equations

$$\frac{d}{dt}(\frac{\partial \mathcal{L}}{\partial \dot{q}_i}) - \frac{\partial \mathcal{L}}{\partial q_i} = 0. \tag{3.93}$$

If q_i denotes a component of the cartesian coordinates for one of the atoms of mass m_i, we have

$$\mathcal{L} = \frac{1}{2}\sum_i m_i \dot{q}_i^2 - U(\{q_i\}), \tag{3.94}$$

where $U(\{q_i\})$ is the potential. Then Eq. 3.93 becomes

$$m_i \ddot{q}_i = -\frac{\partial U}{\partial q_i} = f_i, \tag{3.95}$$

where f_i is the corresponding force component. An alternative formulation is based on the Hamiltonian $\mathcal{H} = \mathcal{H}(\{q_i\}, \{p_i\}, t)$ that is defined as

$$\mathcal{H} = \sum_i \dot{q}_i p_i - \mathcal{L}, \tag{3.96}$$

where p_i is the generalized momentum

$$p_i = \frac{\partial \mathcal{L}}{\partial \dot{q}_i}. \tag{3.97}$$

The Hamiltonian equations of motion read

$$\dot{q}_i = \frac{\partial \mathcal{H}}{\partial p_i},\ \dot{p}_i = -\frac{\partial \mathcal{H}}{\partial q_i}. \tag{3.98}$$

3.3.2 Interatomic potenital

At the very heart of any MD simulation is the question of how to describe or approximate the interatomic potential $U\{q_i\}$ [94]. As discussed in Section 3.2, it is a highly nontrivial task to determine the potential energy surface from first-principles. MD scheme adopts a classical point of view, that is, each atom is represented as point mass, interacting through forces that depend on the separation. The interatomic potential used in MD is therefore a classical effective potential that approximates the quantum mechanical description. In practice, the full interaction is decomposed into two-body and many-body terms, long-range and short-range terms, and electrostatic and non-electrostatic interactions, which are represented by suitable functional forms. The parameters in these analytical energy functionals, in most cases, are not derived (calculated) directly from first-principles, but rather, are the product of the parametrization using a database of information, including the results of quantum mechanical calculations of energies and forces, experimental thermodynamic properties (e.g., density), spectroscopic data (e.g., vibrational frequency) and so on [116]. The parameters may be refined to improve the agreement between theory and experiment for a particular observable of interest (with possible sacrifice of the accuracy of other properties). Following are some widely used potentials:

(1) Lennard-Jones potential,

$$U = \epsilon_{ij}\left[\left(\frac{\sigma_{ij}}{r_{ij}}\right)^{12} - \left(\frac{\sigma_{ij}}{r_{ij}},\right)^{6}\right] \tag{3.99}$$

where ϵ is the depth of the potential well, σ is the distance at which the potential becomes zero.

(2) Buckingham potential,

$$U = Ae^{-Br} - \frac{C}{r^6}, \tag{3.100}$$

where A, B and C are constants for a given atomic pair.

(3) Harmonic bond potential,

$$U = k_b(r - r_0)^2, \tag{3.101}$$

where k_b is the spring constant and r_0 is the equilibrium bond length.

We developed a model potential based on two conservation principles in bond-valence theory for oxides:

(1) *Bond-valence conservation principle*: each atom i prefers to have the total bond valence of its bonds equal to its atomic valence, $V_{0,i}$ [24]. The actual atomic valence V_i for atom i can be calculated by summing over the individual bond valences V_{ij} for bonds between the atom and its nearest neighbors

$$V_{ij} = (\frac{r_{ij}}{r_{ij}^0})^{N_{ij}} \tag{3.102}$$

where r_{ij}^0 and N_{ij} are Brown's empirical parameters.

(2) *Bond-valence vector conservation principle*: each atom is assumed to have a desired length of bond-valence vector sum (BVVS). The bond-valence vector (BVV),$\mathbf{V}_{ij}$, is defined as a vector directed along the bond line with magnitude equal to the scalar bond valence. The bond-valence vector sum,$\mathbf{W}_{0,i}$, is the vector sum of individual $\mathbf{V}_{ij}$ [28]. As will demonstrated in Chapters 4 and 5, the BVVS serves as a measure of local symmetry breaking. Based on these conservation principles, we proposed bond-valence energy and

bond-valence vector energy.

$$U_{\mathrm{BV}} = \sum_i S_i (V_i - V_{0,i})^2, \tag{3.103}$$

and

$$U_{\mathrm{BVV}} = \sum_i D_i (\mathbf{W}_i^2 - \mathbf{W}_{0,i}^2)^2 \tag{3.104}$$

where S_i and D_i are scaling factors.

The force can be evaluated with Eq. 3.95 once the analytical form of the potential is known. Here we document the detailed derivation of the force resulting from bond-valence vector energy. The BVVS $\mathbf{W}_i$ for atom i at (x_i, y_i, z_i) can be calculated with

$$\mathbf{W}_i = \mathbf{W}_{ix} + \mathbf{W}_{iy} + \mathbf{W}_{iz}, \tag{3.105}$$

where

$$\begin{aligned} \mathbf{W}_{ix} &= \sum_{j \neq i} V_{ij} \frac{(x_i - x_j)}{r_{ij}} \hat{\mathbf{x}} \\ \mathbf{W}_{iy} &= \sum_{j \neq i} V_{ij} \frac{(y_i - y_j)}{r_{ij}} \hat{\mathbf{y}} \\ \mathbf{W}_{iz} &= \sum_{j \neq i} V_{ij} \frac{(z_i - z_j)}{r_{ij}} \hat{\mathbf{z}} \end{aligned} \tag{3.106}$$

For a given atom n, the x-component of the force is

$$\begin{aligned}
-f_n^x =& \frac{\partial U_{\mathrm{BVV}}}{\partial x_n} \\
=& \sum_i 2D_i(\mathbf{W}_i^2 - \mathbf{W}_{0,i}^2)2V_{ix}\frac{\partial V_{ix}}{\partial x_n} \\
&+ \sum_i 2D_i(\mathbf{W}_i^2 - \mathbf{W}_{0,i}^2)2V_{iy}\frac{\partial V_{iy}}{\partial x_n} \\
&+ \sum_i 2D_i(\mathbf{W}_i^2 - \mathbf{W}_{0,i}^2)2V_{iz}\frac{\partial V_{iz}}{\partial x_n},
\end{aligned} \tag{3.107}$$

where

$$\frac{\partial V_{ix}}{\partial x_n} = \sum_{j\neq i}\left(\frac{\partial V_{ij}}{\partial x_n}\frac{(x_i - x_j)}{r_{ij}} + V_{ij}(x_i - x_j)\frac{\partial(1/r_{ij})}{\partial x_n} + \frac{V_{ij}}{r_{ij}}\frac{\partial(x_i - x_j)}{\partial x_n}\right). \tag{3.108}$$

Given that

$$\frac{\partial r_{ij}}{\partial x_n} = \frac{x_i - x_j}{r_{ij}}\delta_{in} + \frac{x_j - x_i}{r_{ij}}\delta_{jn}, \tag{3.109}$$

we have

$$\frac{\partial V_{ij}}{\partial x_n} = -N_{ij}\left(\frac{r_{ij}^0}{r_{ij}}\right)^{N_{ij}-1}\frac{r_{ij}^0}{r_{ij}^2}\frac{\partial r_{ij}}{\partial x_n} = -\frac{N_{ij}V_{ij}}{r_{ij}}[\frac{x_i - x_j}{r_{ij}}\delta_{in} + \frac{x_j - x_i}{r_{ij}}\delta_{jn}], \tag{3.110}$$

$$\frac{\partial(1/r_{ij})}{\partial x_n} = -\frac{1}{r_{ij}^2}(\frac{x_i - x_j}{r_{ij}}\delta_{in} + \frac{x_j - x_i}{r_{ij}}\delta_{jn}). \tag{3.111}$$

Substituting Eqs. 3.110 and 3.111 into Eq. 3.108 leads to

$$\frac{\partial V_{ix}}{\partial x_n} = \sum_{j\neq i}\frac{V_{ij}}{r_{ij}}(\delta_{in} - \delta_{jn} - \frac{(N_{ij}+1)(x_i - x_j)^2}{r_{ij}^2}\delta_{in} + \frac{(N_{ij}+1)(x_j - x_i)^2}{r_{ij}^2}\delta_{jn}). \tag{3.112}$$

Similarly, we have

$$\frac{\partial V_{iy}}{\partial x_n} = \sum_{j\neq i}\left(\frac{\partial V_{ij}}{\partial x_n}\frac{(y_i-y_j)}{r_{ij}} + V_{ij}(y_i-y_j)\frac{\partial(1/r_{ij})}{\partial x_n}\right), \tag{3.113}$$

$$\frac{\partial V_{iz}}{\partial x_n} = \sum_{j\neq i}\left(\frac{\partial V_{ij}}{\partial x_n}\frac{(z_i-z_j)}{r_{ij}} + V_{ij}(z_i-z_j)\frac{\partial(1/r_{ij})}{\partial x_n}\right). \tag{3.114}$$

Now the x-component of the force can be written as

$$\begin{aligned} f_n^x = & \sum_i D_{ix}\left[\sum_{j\neq i}\frac{V_{ij}}{r_{ij}}(-\delta_{in}+\delta_{jn}+\frac{(N_{ij}+1)(x_i-x_j)^2}{r_{ij}^2}\delta_{in}-\frac{(N_{ij}+1)(x_j-x_i)^2}{r_{ij}^2}\delta_{jn})\right] \\ & +\sum_i D_{iy}\left[\sum_{j\neq i}\frac{V_{ij}}{r_{ij}}(\frac{(N_{ij}+1)(y_i-y_j)(x_i-x_j)}{r_{ij}^2}\delta_{in}-\frac{(N_{ij}+1)(y_j-y_i)(x_i-x_j)}{r_{ij}^2}\delta_{jn})\right] \\ & +\sum_i D_{iz}\left[\sum_{j\neq i}\frac{V_{ij}}{r_{ij}}(\frac{(N_{ij}+1)(z_i-z_j)(x_i-x_j)}{r_{ij}^2}\delta_{in}-\frac{(N_{ij}+1)(z_j-z_i)(x_i-xj)}{r_{ij}^2}\delta_{jn})\right], \end{aligned} \tag{3.115}$$

where $D_{i\alpha} = 4D_i(\mathbf{W}_i^2 - \mathbf{W}_{0,i}^2)V_{i\alpha},\ [\alpha = x, y, z]$. By defining following terms:

$$\begin{aligned} E(i,j) =& \frac{(N_{ij}+1)}{r_{ij}^2} \\ \Delta_x^{ij} =& x_i - x_j \\ \Delta_y^{ij} =& y_i - y_j \\ \Delta_z^{ij} =& y_i - y_j, \end{aligned} \tag{3.116}$$

we can write the force in a more concise way

$$\begin{aligned}
f_n^x &= \sum_i D_{ix}\left\{\sum_{j\neq i}\frac{V_{ij}}{r_{ij}}\left[-\delta_{in}+\delta_{jn}+E(i,j)(\Delta_x^{ij})^2\delta_{in}-E(i,j)(\Delta_x^{ij})^2\delta_{jn}\right]\right\}\\
&+\sum_i D_{iy}\left\{\sum_{j\neq i}\frac{V_{ij}}{r_{ij}}\left[E(i,j)\Delta_x^{ij}\Delta_y^{ij}\delta_{in}-E(i,j)\Delta_x^{ij}\Delta_y^{ij}\delta_{jn}\right]\right\}\\
&+\sum_i D_{iz}\left\{\sum_{j\neq i}\frac{V_{ij}}{r_{ij}}\left[E(i,j)\Delta_x^{ij}\Delta_z^{ij}\delta_{in}-E(i,j)\Delta_x^{ij}\Delta_z^{ij}\delta_{jn}\right]\right\}. \qquad (3.117)
\end{aligned}$$

Applying the Kronecker delta function and rearranging the terms, we obtain

$$\begin{aligned}
f_n^x &= -D_{nx}\sum_{j\neq n}\frac{V_{nj}}{r_{nj}}+\sum_{i\neq n}D_{ix}\frac{V_{in}}{r_{in}}+D_{nx}\sum_{j\neq n}\frac{V_{nj}}{r_{nj}}E(n,j)(\Delta_x^{nj})^2-\sum_{i\neq n}D_{ix}\frac{V_{in}}{r_{in}}E(i,n)(\Delta_x^{in})^2\\
&+D_{ny}\sum_{j\neq n}\frac{V_{nj}}{r_{nj}}E(n,j)\Delta_x^{nj}\Delta_y^{nj}-\sum_{i\neq n}D_{iy}\frac{V_{in}}{r_{in}}\Delta_x^{in}\Delta_y^{in}\\
&+D_{nz}\sum_{j\neq n}\frac{V_{nj}}{r_{nj}}E(n,j)\Delta_x^{nj}\Delta_z^{nj}-\sum_{i\neq n}D_{iz}\frac{V_{in}}{r_{in}}E(i,n)\Delta_x^{in}\Delta_y^{in}, \qquad (3.118)
\end{aligned}$$

$$\begin{aligned}
f_n^x &= -D_{nx}\sum_{j\neq n}\frac{V_{nj}}{r_{nj}}+\sum_{j\neq n}D_{jx}\frac{V_{jn}}{r_{jn}}+D_{nx}\sum_{j\neq n}\frac{V_{nj}}{r_{nj}}E(n,j)(\Delta_x^{nj})^2-\sum_{j\neq n}D_{jx}\frac{V_{jn}}{r_{jn}}(\Delta_x^{jn})^2\\
&+D_{ny}\sum_{j\neq n}\frac{V_{nj}}{r_{nj}}\Delta_x^{nj}\Delta_y^{nj}-\sum_{j\neq n}D_{jy}\frac{V_{jn}}{r_{jn}}\Delta_x^{jn}\Delta_y^{jn}\\
&+D_{nz}\sum_{j\neq n}\frac{V_{nj}}{r_{nj}}\Delta_x^{nj}\Delta_z^{nj}-\sum_{j\neq n}D_{jz}\frac{V_{jn}}{r_{jn}}\Delta_x^{nj}\Delta_z^{nj}. \qquad (3.119)
\end{aligned}$$

Finally, we reach

$$\begin{aligned} f_n^x = &\sum_{j\neq n}(D_{jx} - D_{nx})\frac{V_{nj}}{r_{nj}} + \sum_{j\neq n}\frac{V_{nj}}{r_{nj}}E(n,j)(\Delta_x^{nj})^2(D_{nx} - D_{jx}) \\ &+ \sum_{j\neq n}\frac{V_{nj}}{r_{nj}}E(n,j)\Delta_x^{nj}\Delta_y^{nj}(D_{ny} - D_{jy}) \\ &+ \sum_{j\neq n}\frac{V_{nj}}{r_{nj}}E(n,j)\Delta_x^{nj}\Delta_z^{nj}(D_{nz} - D_{jz}). \end{aligned} \tag{3.120}$$

3.3.3 Integration algorithms

The trajectory in MD simulations is advanced by integrating the equations of motion. A variety of integrators are available. The Verlet algorithm is one of the simplest and yields coordinates that are accurate to third order in Δt (time step) [95, 117]. The derivation of the Verlet formula follows immediately from the Taylor expansion of the coordinate variable,

$$x(t + \Delta t) = x(t) + \Delta t\dot{x}(t) + \frac{\Delta t^2}{2}\ddot{x}(t) + \frac{\Delta t^3}{3!}\dddot{x}(t) + O(\Delta t^4), \tag{3.121}$$

where t is the current time. Similarly

$$x(t - \Delta t) = x(t) - \Delta t\dot{x}(t) + \frac{\Delta t^2}{2}\ddot{x}(t) - \frac{\Delta t^3}{3!}\dddot{x}(t) + O(\Delta t^4). \tag{3.122}$$

Summing these two equations give

$$x(t + \Delta t) + x(t - \Delta t) = 2x(t) + \Delta t^2\ddot{x}(t) + O(\Delta t^4), \tag{3.123}$$

or

$$x(t + \Delta t) \approx 2x(t) - x(t - \Delta t) + \Delta t^2\ddot{x}(t). \tag{3.124}$$

The estimate of the new position contains an error that is of order Δt^4. The velocity can also be obtained as

$$x(t+\Delta t) - x(t-\Delta t) = 2\Delta t\dot{x}(t) + O(\Delta t^3), \tag{3.125}$$

or

$$v(t) = \dot{x}(t) = \frac{x(t+\Delta t) - x(t-\Delta t)}{2\Delta t} + O(\Delta t^2). \tag{3.126}$$

The expression for the velocity is only accurate to the order Δt^2. An equivalent integrating algorithm is the so-called Leapfrog algorithm [94]. It integrates the velocities at half-integer time steps and uses these velocities to compute the new positions,

$$v(t-\Delta t/2) = \frac{x(t) - x(t-\Delta t)}{\Delta t}, \tag{3.127}$$

and

$$v(t+\Delta t/2) = \frac{x(t+\Delta t) - x(t)}{\Delta t}. \tag{3.128}$$

From Eq. 3.128, the new position can be calculated with

$$x(t+\Delta t) = x(t) + v(t+\Delta t/2)\Delta t. \tag{3.129}$$

It is noted that the coordinates and velocities are evaluated at different times. If an estimate for $v(t)$ is required, following is a simple connection

$$v(t) = \dot{x}(t) = \dot{x}(t \mp \Delta t/2) \pm (\Delta t/2)\ddot{x}(t). \tag{3.130}$$

Once the new positions $x(t+\Delta t)$ is known, we may discard the positions at time $t-\Delta t$. The current positions become the old positions and the new positions become the current positions.

3.3.4 Temperature control: thermostat

A convenient definition of the temperature T in a classical many-body system makes use of the equipartition theorem over all degrees of freedom,

$$\frac{1}{2}k_B T N_{df} = \langle \mathcal{K} \rangle = \left\langle \sum_{i,\alpha} \frac{1}{2} m_i v_{i\alpha}^2 \right\rangle, \tag{3.131}$$

where k_B is Boltzmann's constant, N_{df} is the number of internal degrees of freedom, $\mathcal{K}$ is the instantaneous internal kinetic energy, m_i is the mass of the particle i, and $v_{i\alpha}$ is the α-th component of its velocity. The instantaneous temperature $\mathcal{T}$ is defined as

$$\mathcal{T} = \frac{2}{k_B N_{df}} \mathcal{K} \tag{3.132}$$

It is noted that the condition of constant temperature is not equivalent to the condition of constant kinetic energy [118]. For a canonical ensemble, the instantaneous kinetic energy per particle fluctuates, and its relative variance is $2/3N$, where N is the number of particles [95]. If the average kinetic energy per particle were fixed constant, then the system simulated is not a true constant-temperature ensemble. The *ad hoc* naive velocity-scaling scheme does not correspond to any known ensemble [95].

3.3.4.1 Anderson thermostat

Andersen proposed to couple the system to a heat bath to impose the desired temperature [119]. The coupling to a heat bath is achieved by occasionally changing the velocities of randomly selected particles. These "stochastic collisions" ensure that all accessible constant-energy levels are visited according to their Boltzmann weight. The coupling strength between the system and the heat bath is determined by the frequency (f) of stochastic collisions. Assuming successive collisions are independent, the distribution of time intervals between successive collisions follows the Poisson distribution:

$$P(t, f) = f \exp(-ft), \tag{3.133}$$

and $P(t, f)dt$ is the probability that collision will occur in interval $[t, t + dt]$. When a particle is selected to undergo a collision, it is given to a new velocity based on the Maxwell-Boltzmann distribution of the desired temperature T. Though Anderson thermostat yields good results for time-independent properties, it can not be applied to study dynamical properties. Because the stochastic collisions are unphysical disturbations, which may lead to sudden and random decorrelation of particles.

3.3.4.2 Nosé thermostat

Nosé proposed a temperature control algorithm based on an extended-system method [120]. The idea is to extend the real system by adding an artificial dynamical variable $\tilde{s}$ associated with an effective mass Q. The timescale in the extended system is stretched by the factor $\tilde{s}$

$$\tilde{\mathbf{r}} = \mathbf{r},\ \dot{\tilde{\mathbf{r}}} = \tilde{s}^{-1}\dot{\mathbf{r}},\ \tilde{s} = s,\ \dot{\tilde{\mathbf{s}}} = \tilde{s}^{-1}\dot{s} \tag{3.134}$$

The Lagrangian for the extended system is

$$\mathcal{L}(\tilde{\mathbf{r}}, \dot{\tilde{\mathbf{r}}}, \tilde{s}, \dot{\tilde{s}}) = \frac{1}{2}\sum_{i}^{N} m_i \tilde{s}^2 \dot{\tilde{\mathbf{r}}}_i^2 - U(\tilde{\mathbf{r}}) + \frac{Q}{2}\dot{\tilde{s}}^2 - g k_B T_o \ln \tilde{s} \tag{3.135}$$

where g is the number of degrees of freedom in the real system and T_o is the reference temperature of the heat bath. The first two terms represent the Lagrangian of the real physical system. The third and fourth terms represent Lagrangian associated with $\tilde{s}$ variable. The equations of motion for the extended system is

$$\ddot{\tilde{\mathbf{r}}}_i = m_i^{-1}\tilde{s}^{-2}\tilde{\mathbf{F}}_i - 2\tilde{s}^{-1}\dot{\tilde{s}}\dot{\tilde{\mathbf{r}}}_i \tag{3.136}$$

for physical variables and

$$\ddot{\tilde{s}} = Q^{-1}\tilde{s}^{-1}\left(\sum_{i=1}^{N} m_i\tilde{s}^2\dot{\tilde{\mathbf{r}}} - gk_BT_o\right) \tag{3.137}$$

for the $\tilde{s}$ variable. The Nosé equations of motion can also be derived using a Hamiltonian formalism. For the extended-system, the physical momenta $\tilde{\mathbf{p}}_i$ and the momentum $\tilde{p}_s$ associated with the $\tilde{s}$-variable are defined as

$$\tilde{\mathbf{p}}_i = \frac{\partial\mathcal{L}(\tilde{\mathbf{r}}, \dot{\tilde{\mathbf{r}}}, \tilde{s}, \dot{\tilde{s}})}{\partial\dot{\tilde{\mathbf{r}}}} = m_i\tilde{s}^2\dot{\tilde{\mathbf{r}}}_i,\ \tilde{p}_s = \frac{\partial\mathcal{L}(\tilde{\mathbf{r}}, \dot{\tilde{\mathbf{r}}}, \tilde{s}, \dot{\tilde{s}})}{\partial\dot{\tilde{s}}} = Q\dot{\tilde{s}}. \tag{3.138}$$

Compared with the real-system momenta,

$$\mathbf{p}_i = m_i\dot{\mathbf{r}}_i,\ p_s = Qs^{-2}\dot{s}, \tag{3.139}$$

the extended-system momenta are amplified by a factor $\tilde{s}$. The extended-system Hamiltonian reads

$$\mathcal{H}(\tilde{\mathbf{r}}, \tilde{\mathbf{p}}, \tilde{s}, \tilde{p}_s) = \frac{1}{2}\sum_{i}^{N} m_i^{-1}\tilde{s}^{-2}\tilde{\mathbf{p}}_i^2 + U(\tilde{\mathbf{r}}) + \frac{1}{2}Q^{-1}\tilde{p}_s^2 + gk_BT_o\ln\tilde{s} \tag{3.140}$$

The corresponding Hamiltonian equations of motion are

$$\dot{\tilde{\mathbf{p}}}_i = \tilde{\mathbf{F}}_i,\ \dot{\tilde{\mathbf{r}}}_i = m_i^{-1}\tilde{s}^{-2}\tilde{\mathbf{p}}_i \tag{3.141}$$

for the physical variables, and

$$\dot{\tilde{p}}_s = \tilde{s}^{-1}\left(\sum_i^N m_i^{-1}\tilde{s}^{-2}\tilde{\mathbf{p}}_i^2 - gk_BT_o\right), \dot{\tilde{s}} = Q^{-1}\tilde{p}_s \tag{3.142}$$

for the $\tilde{s}$-variable. For the whole extended system, the Nosé equations of motion sample a microcanonical ensemble with a constant energy. However ,the energy of the real physical system is not constant. The heat transfers between the real physical system and the heat bath as $\tilde{s}$ fluctuates. The sign of $\dot{\tilde{s}}$ determines the direction of the heat flow: when $\dot{\tilde{s}} < 0$, the heat flows into the real system; when $\dot{\tilde{s}} > 0$, the heat flows out of the real system. Nosé proved that Eqs. 3.136 and 3.137 sample a canonical ensemble of microstates of the real physical system [120]. The Nosé equations of motion are smooth, deterministic and time-reversible. Because the evolution of the variable $\tilde{s}$ (Eq. 3.137) is described by a second-order equation, the temperature of the real system will fluctuate in a nearly-periodic fashion as heat flows into and out of the system in an oscillatory way. However, the dynamics of the temperature evolution should not be periodic due to stochastic fluctuations and exponential thermal relaxation. The frequency of oscillation is closely related to the value of the effective mass Q and can be approximated as [118]

$$\nu = (2\pi)^{-1}(2N_{df}k_BT_o)^{1/2}Q^{-1/2}, \tag{3.143}$$

providing the velocities of the real system are initiated from a Maxwell-Boltzmann distribution, together with $\tilde{s}(0) = 1$ and $\dot{\tilde{s}}(0) = 0$.

3.3.4.3 Nosé-Hoover thermostat

As shown by Nosé and Hoover [121], the Nosé equations of motion can be reformulated in terms of real-system variables through following transformations:

$$\begin{aligned}
& dt = \tilde{s}^{-1} d\tilde{t},\ d/dt = \tilde{s}/d\tilde{t}, \\
& s = \tilde{s},\ \dot{s} = \tilde{s}\dot{\tilde{s}},\ \ddot{s} = \tilde{s}^2\ddot{\tilde{s}} + \tilde{s}\dot{\tilde{s}}^2, \\
& \mathbf{r} = \tilde{\mathbf{r}},\ \dot{\mathbf{r}} = \tilde{s}\dot{\tilde{\mathbf{r}}},\ \ddot{\mathbf{r}} = \tilde{s}^2\ddot{\tilde{\mathbf{r}}} + \tilde{s}\dot{\tilde{s}}\dot{\tilde{\mathbf{r}}}, \\
& p_s = \tilde{s}^{-1}\tilde{p}_s,\ \dot{p}_s = \dot{\tilde{p}}_s - Q^{-1}\tilde{s}^{-1}\tilde{p}_s^2, \\
& \mathbf{p} = \tilde{s}^{-1}\tilde{\mathbf{p}},\ \dot{\mathbf{p}} = \dot{\tilde{\mathbf{p}}} - Q^{-1}\tilde{s}^{-1}\tilde{p}_s\tilde{\mathbf{p}}.
\end{aligned} \tag{3.144}$$

By defining the quantity $\gamma = s^{-1}\dot{s} = Q^{-1}sp_s$, the Lagrangian equations of motion can be rewritten as

$$\ddot{\mathbf{r}}_i = m_i^{-1}\mathbf{F}_i - \gamma\dot{\mathbf{r}}_i, \tag{3.145}$$

where

$$\dot{\gamma} = -k_B N_{df} Q^{-1} \mathcal{T} \left(\frac{g}{N_{df}} \frac{T_o}{\mathcal{T}} - 1 \right). \tag{3.146}$$

It is noted that γ is a dynamical variable as its time derivative $\dot{\gamma}$ is determined by the instantaneous microstate of the system ($\mathcal{T}$). The variable γ plays the same role in Nosé-Hoover formulation as $\dot{\tilde{s}}$ in the Nosé formulation. That is, when γ is positive (negative), heat flows out of (into) the system. Noticeably, when the system temperature increases above T_o, the derivative of γ becomes positive, and the heat flow is progressively reduced. It is also proved that Nosé-Hoover equations of motion sample a canonical ensemble. The Nosé-Hoover equations of motion are smooth, deterministic and time-reversible.

The choice of fictitious mass Q requires some more words. One the one hand, too large value of Q may cause a poor temperature control. A long simulation time is required to obtain canonical distribution. On the other hand, too small value of Q may cause rapid temperature oscillations ($v \propto Q^{-1/2}$). When the frequency of the $\tilde{s}$-variable oscillation is significantly higher than the characteristic frequencies of the real physical system, the heat bath becomes effectively decoupled from the physical degrees of freedom. Consequently, a long simulation time is also required to achieve canonical sampling. If the initial real-system velocities are taken from a Maxwell-Boltzmann distribution, $Q \approx 1.4 N_{df} k_B T_o \xi_T^2$ is suggested as an appropriate value for simulations, where ξ_T is the temperature relaxation time [118, 122].

3.3.5 Pressure control: barostat

For a spatially homogenous system, the instantaneous internal pressure $\mathcal{P}$ of a system can be calculated with

$$\mathcal{P} = \frac{1}{dV}\left[\sum_i^N \left(\frac{\mathbf{p}_i^2}{m_i} + \mathbf{r}_i \mathbf{F}_i\right) - dV\frac{\partial U}{\partial V}\right], \tag{3.147}$$

where U is the potential. Andersen originally proposed a method for constant pressure MD simulations based on the extended ensemble approach [119]. The essential idea is to couple the system to an external variable V, the volume of the simulation box. This coupling mimics the effect of a piston. The piston has an effective mass Q. The coordinates and velocities of atoms in the real system are scaled as

$$\mathbf{r} = V^{1/3}\mathbf{s} \text{ and } \dot{\mathbf{r}} = V^{1/3}\dot{\mathbf{s}}. \tag{3.148}$$

The Lagrangian for the extended system is

$$\mathcal{L}(\mathbf{s}, V) = \frac{1}{2}\sum_i^N m_i V^{2/3}\dot{\mathbf{s}}_i^2 - U(\{V^{1/3}\mathbf{s}\}) + \frac{1}{2}Q\dot{V} - P_o V, \tag{3.149}$$

where P_o is the specified pressure. The equations of motion are

$$\begin{aligned} \ddot{\mathbf{s}} &= \frac{\mathbf{f}}{mV^{1/3}} - \frac{2}{3}\dot{\mathbf{s}}\dot{V}/V \\ \ddot{\mathbf{V}} &= (\mathcal{P} - P_o)/Q. \end{aligned} \tag{3.150}$$

Both $\mathbf{f}$ and $\mathcal{P}$ are calculated using normal, unscaled coordinates and momenta.

Andersen's method only allows for isotropic changes in the volume of the simulation box. Parrinello and Rahman extended this method to allow for anisotropic changes, varying both shape and size [123]. This technique is particularly useful for simulating phase transitions of solid crystals which involve the changes in the cell dimensions and angles. The coordinates are scaled as

$$\mathbf{r} = \mathbf{hs}, \tag{3.151}$$

where $\mathbf{h}$ is a 3×3 matrix whose columns are the vectors $\mathbf{a}$,$\mathbf{b}$ and $\mathbf{c}$ of the simulation box. The volume of the box is given by $V = |\mathbf{h}| = \mathbf{a} \cdot \mathbf{b} \times \mathbf{c}$. The equations of motion are again obtained from the Lagrange of the extended system:

$$\begin{aligned} m\ddot{\mathbf{s}} &= \mathbf{h}^{-1}\mathbf{f} - m\mathbf{G}^{-1}\dot{\mathbf{G}}\dot{\mathbf{s}} \\ Q\ddot{h} &= (\mathcal{P} - P_o)V(\mathbf{h}^{-1})^{\mathrm{T}}, \end{aligned} \tag{3.152}$$

where $\mathbf{G} = \mathbf{h}^{\mathrm{T}}\mathbf{h}$. The instantaneous stress tensor is given as

$$\mathcal{P}_{\alpha\beta} = \frac{1}{V}\left(\sum_i m(\mathbf{h}\dot{\mathbf{s}}_i)_\alpha^{\mathrm{T}}(\mathbf{h}\dot{\mathbf{s}}_i)_\beta + \sum_i \sum_{j>i} (\mathbf{hs}_{ij})_\alpha(\mathbf{f}_{ij})_\beta\right). \tag{3.153}$$

where $\mathbf{f}_{ij}$ is the force on i due to j in unscaled form.

Chapter 4

Reinterpretation of bond-valence model with bond-order formalism: an improved bond-valence based interatomic potential for $PbTiO_3$

4.1 Introduction

The use of ferroelectric perovskite oxides in a variety of technological applications has prompted extensive investigations of their structure and dynamics [1, 4]. First-principles density functional theory (DFT) calculations have played an important role in enhancing microscopic understanding of the relationships between composition, structure and properties [8–10]. Despite the success of first-principles methods, the great computational expense and the difficulties of studying finite-temperature properties have driven the development of more efficient atomistic and effective Hamiltonian potentials suitable for large-scale molecular dynamics (MD) simulations [11–22]. In particular, an atomistic potential based on the widely used bond-valence (BV) theory [24] has been developed [14, 16]. BV-based atomistic potentials have since been used to study phase transitions [124] and domain wall motion in $PbTiO_3$ [25], as well as structure and dynamics in the classic $0.75PbMg_{1/3}Nb_{2/3}O_3$-$0.25PbTiO_3$ relaxor ferroelectric material [26, 27].

The bond-valence theory, or bond-valence conservation principle, states that in a crystal structure, each atom i prefers to obtain a certain atomic valence, $V_{0,i}$. The actual atomic valence V_i, for atom i can be obtained by summing over the bond valences V_{ij}, which can be calculated from an empirical inverse power-law relationship [125, 126] between bond valence and bond length r_{ij}:

$$V_{ij} = \left(\frac{r_{0,ij}}{r_{ij}}\right)^{C_{ij}}. \tag{4.1}$$

$r_{0,ij}$ and C_{ij} are Brown's empirical parameters. The energy contribution of the bond-valence is chosen to have the following form:

$$E_{BV} = \sum_i \varepsilon_i = \sum_i S_i (V_i - V_{0,i})^2, \tag{4.2}$$

where ε_i is the atomic bond-valence energy and S_i is a scaling parameter.

Despite the success of the rather simple ten-parameter BV model potential [16] for $\mathrm{PbTiO_3}$, no rigorous quantum mechanical justification has been provided for the bond-valence potential energy, raising questions about the general applicability of this type of atomistic potential. In addition, the potentials obtained in previous work [16, 124] were found to be accurate for NVT simulations only, with incorrect ground state structures obtained when the constant volume constraint is lifted. In this paper, we show how the bond-valence energy can be derived from the second-moment bond-order potential, extend the model to represent higher moments of the local density of states (LDOS), and show that this allows accurate simulations for both constant-volume and constant-pressure conditions.

4.2 Methodology

An analysis of the physics that gives rises to the bond-valence conservation principle shows that the bond-valence energy can be naturally derived from the second-moment bond-order potential, such as the well-known Finnis-Sinclair potential [127, 128]. Within the framework of a tight-binding model [129], the Finnis-Sinclair potential can be partitioned into atomic contributions as:

$$U_{\mathrm{FS}}(\mathbf{r}_1, ...\mathbf{r}_{\mathrm{N}}) = \sum_i E_i = \sum_i \left[\sum_{\langle j \rangle} \phi(r_{ij}) - \gamma_i (\mu_i^{(2)})^{\frac{1}{2}} \right], \tag{4.3}$$

where $\mathbf{r}_i$ is the atomic position, E_i is the local atomic energy and $\phi(r_{ij})$ is a pair-wise repulsive potential depending on the distance between atom i and its nearest-neighboring atom j. The second term represents the bonding energy; γ_i is a constant and $\mu_i^{(2)}$ is the second moment of the LDOS. The second moment $\mu_i^{(2)}$ measures the width of the LDOS distribution, and as shown by Cyrot-Lackmann and Ducastelle [130–132], can be evaluated from the summation over all the nearest-neighbor hopping paths that start and end on atom

i:

$$\mu_i^{(2)} = \sum_{\langle j \rangle} \beta_{ij}\beta_{ji} = \sum_{\langle j \rangle} \beta_{ij}^2, \tag{4.4}$$

where $\langle j \rangle$ means the summation of nearest neighbors of i, and β_{ij} is the *averaged* hopping integral between atom i and j. Because the overlap of atomic orbitals decays as $\exp(-\sigma_{ij}r_{ij})$ [128], Eq (3) can be written as

$$U_{\text{FS}} = \sum_i E_i = \sum_i \sum_{\langle j \rangle} a_{ij} e^{-2\sigma_{ij}r_{ij}} - \sum_i \gamma_i \left(\sum_{\langle j \rangle} b_{ij} e^{-2\sigma_{ij}r_{ij}} \right)^{\frac{1}{2}}, \tag{4.5}$$

with $\phi(r_{ij}) = a_{ij}e^{-2\sigma_{ij}r_{ij}}$ and $\mu_i^{(2)} = \sum_{\langle j \rangle} b_{ij}e^{-2\sigma_{ij}r_{ij}}$, where a_{ij} is a constant that scales the strength of the repulsive interactions between atom i and atom j, and b_{ij} scales the bonding interaction.

Despite the different appearance of Eq (4.2) and Eq (4.5), we can rewrite the bond-valence energy in a similar form to the FS potential. First of all, we point out that the energy function for bond-valence energy is not unique since Eq (4.2) simply enforces that any deviation from the desired atomic valence will incur an energy penalty. Therefore, we could rewrite the bond-valence energy as

$$E'_{BV} = \sum_i S'_i \left(\sqrt{V_i} - \sqrt{V_{0,i}}\right)^2, \tag{4.6}$$

with a proper choice of S' as a scaling parameter. The bond-valence is an empirical concept, and it has been modeled with various functional forms including inverse power law and exponential [24]. For the narrow range of distances of first nearest neighbor pairs, exponential and power law yield similar results. Given that the bond-valence reflects the bonding strength, we define it as an exponential of the interatomic distance:

$$V_{ij} = b'_{ij} e^{-2\sigma_{ij} r_{ij}} \tag{4.7}$$

where b'_{ij} is a parameter depending upon the type of atomic pair. Expanding Eq (4.6) gives

$$E'_{BV} = \sum_i S'_i V_i - 2S'_i \sqrt{V_{0,i} V_i} + S'_i V_{0,i}. \tag{4.8}$$

The last term, $S'_i V_{0,i}$, is a constant and will cancel out when energy differences are considered. Henceforth we will not write out this constant term explicitly. Substituting Eq (4.7) into Eq (4.8), we obtain

$$E'_{BV} = \sum_i \sum_{\langle j \rangle} S'_i b'_{ij} e^{-2\sigma_{ij} r_{ij}} - \sum_i 2S'_i \sqrt{V_{0,i}} \left(\sum_{\langle j \rangle} b'_{ij} e^{-2\sigma_{ij} r_{ij}} \right)^{\frac{1}{2}}. \tag{4.9}$$

It becomes evident that the bond-valence energy expressed in Eq (4.9) is remarkably similar to the FS potential in Eq (4.5). Eq (4.5) and Eq (4.9) becomes equivalent if we choose

$$S'_i b'_{ij} = a_{ij} \tag{4.10a}$$

$$2S'_i b'_{ij} \sqrt{V_{0,i}} = b_{ij} \tag{4.10b}$$

Rearranging Eq (4.10), we obtain $V_{0,i} = b_{ij}^2 / 4a_{ij}^2$. Therefore, for any system where the ratio of coefficients for bonding and repulsive interactions, b_{ij}/a_{ij}, is constant among the neighbors of atom i, this ratio defines this atom's bond valence. Thus, the bond valence energy Eq (4.9) is equivalent to Eq (4.5). The equivalence between the bond-valence energy and the Finnis-Sinclair potential means that the bond-valence conservation experimentally observed in solids is based on the quantum-mechanical description of bonding that underlies the Finnis-Sinclair model.

Compared to the bond-order potential, the application of the bond-valence model does not require extra efforts to parametrize hopping integrals, because the bond-valence parameters for a wide variety of atomic pairs are already known from crystallography [24]. Since the bond-valence model is a second-moment bond-order potential, its limitations, such as the inability to obtain the correct ground state structure in NPT simulations, are likely due to the fact that the second moment only accounts for the width of LDOS but does not reflect its shape. One consequence of this is that the BV energy depends only on the total valence and is entirely insensitive to the number of bonds or their relative strengths. This feature of all second-moment models makes it difficult to distinguish between competing crystal structures, which are controlled by the higher moments [128]. Therefore, a systematic way to improve the bond-valence model is to include the contributions of higher moments of the LDOS (such as fourth moment) to the total energy [133, 134].

In this work, we choose the bond-valence vector sum (BVVS) [24, 28] to reflect the change of the fourth moment of the LDOS. The bond-valence vector is defined as a vector lying along the bond with magnitude equal to the bond-valence ($|\mathbf{V}_{ij}| = V_{ij}$), as shown in Fig. 4.1. A simple argument is presented in the Appendix to illustrate the relationship between the fourth moment of the LDOS and the sum of the bond-valence vectors in a periodic structure. Generally, the changes in the local symmetry of the bonding environment affect the value of the fourth moment of the LDOS, which is also reflected by the change of BVVS. We suggest that BVVS is a natural way to capture the change in the fourth moment of LDOS. For many materials, it has been shown that the ground-state structure favors symmetric local bonding environment and a zero BVVS. Therefore, the criterion of BVVS = 0 for the ground-state structure has been suggested as a complement to the original bond-valence conservation principle [24, 28]. However, this is not followed for crystal structures in which symmetry breaking (BVVS $\neq 0$) becomes significant due to electronic-structure driven distortions, such as the second order Jahn-Teller distortion exhibited by Ti atoms in an octahedral environment and the stereochemical lone-pair driven distortions of Pb^{2+} cation. The BVVS can thus be considered as a measure of local symmetry breaking. We therefore generalize this principle by proposing that each ion has a desired length of bond-valence vector sum. The bond-valence vector energy, E_{BVV}, is defined as

$$E_{BVV} = \sum_{i} D_i (\mathbf{W}_i^2 - \mathbf{W}_{0,i}^2)^2, \tag{4.11}$$

where

$$\mathbf{W}_i = \sum_{j \neq i} \mathbf{V}_{ij} = \sum_{j \neq i} V_{ij} \hat{\mathbf{R}}_{ij}. \tag{4.12}$$

D_i is the scaling factor, $\hat{\mathbf{R}}_{ij}$ is a unit vector pointing from atom i to j, $\mathbf{W}_i$ is the calculated bond-valence vector sum and $\mathbf{W}_{0,i}$ is the desired value of bond-valence vector sum. It is noted that only the norm of the bond-valence vector sum is taken in the energy term (square of $\mathbf{W}_i$) since the energy is a scalar quantity and the energy expression should bot break the system symmetry. The value of $\mathbf{W}_{0,i}$ can be computed using the optimized atomic positions in the lowest-energy structure identified from first principles. We note here that the proposed BVV energy is a simplified fourth-moment bond-order potential, as the calculation of BVVS for a given atom only requires the knowledge of its nearest neighbors.

The interatomic potential for our modified bond-valence model is given by:

$$E = E_c + E_r + E_{BV} + E_{BVV} + E_a \tag{4.13}$$

$$E_c = \sum_{i<j} \frac{q_i q_j}{r_{ij}} \tag{4.14}$$

$$E_r = \sum_{i<j} \left(\frac{B_{ij}}{r_{ij}} \right)^{12} \tag{4.15}$$

$$E_a = k \sum_{i}^{N_{\text{oxygen}}} (\theta_i - 180^\circ)^2 \tag{4.16}$$

where E_c is the Coulomb energy and E_r is the short-range repulsive Lennard-Jones energy. In both the Finnis-Sinclair potential and the bond-valence model, only averaged hopping integrals between neighboring atoms are used, which is equivalent to approximating all the atomic orbitals as s-type [128]. However, bonding in $PbTiO_3$ involves p-d orbital hybridizations, which do display angular dependence. Physically, in $PbTiO_3$ this results in an energy cost for rotations of oxygen octahedra. To introduce the dependence of energy on the interatomic angles, we include an angle potential term, E_a, which is defined locally for all the O-O-O angles along the oxygen octahedral axes, as shown in Fig. 4.2. This rotationally-invariant angle potential prevents unphysically large tilting of oxygen octahedra.

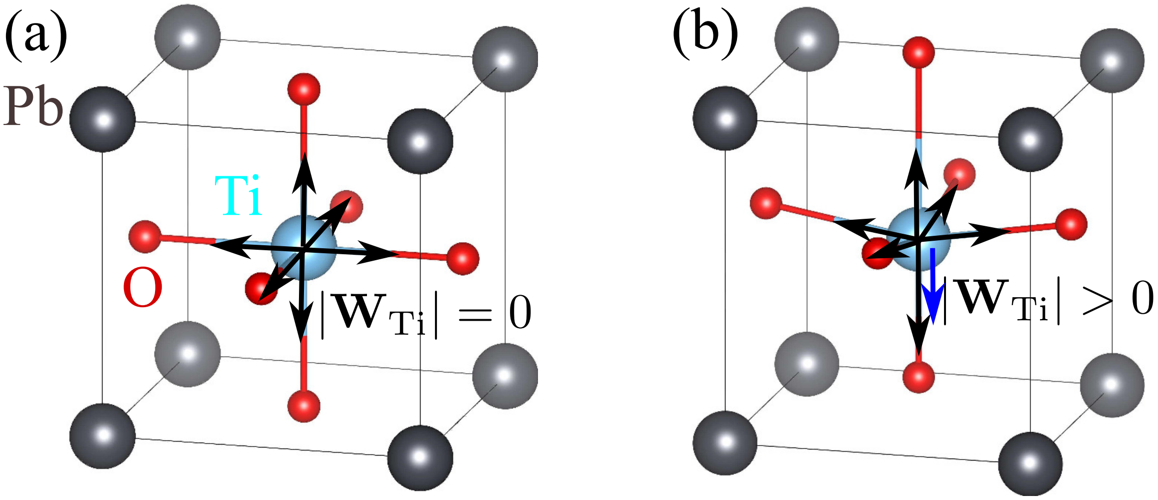

Figure 4.1: Schematic representation of bond-valence vector summation around Ti in (a) cubic $PbTiO_3$ and (b) tetragonal $PbTiO_3$. Gray, blue and red balls denote Pb, Ti and O. The back arrows scale the individual bond-valences, and the blue arrow shows the resultant bond-valence vector sum $\mathbf{W}_{\mathrm{Ti}}$.

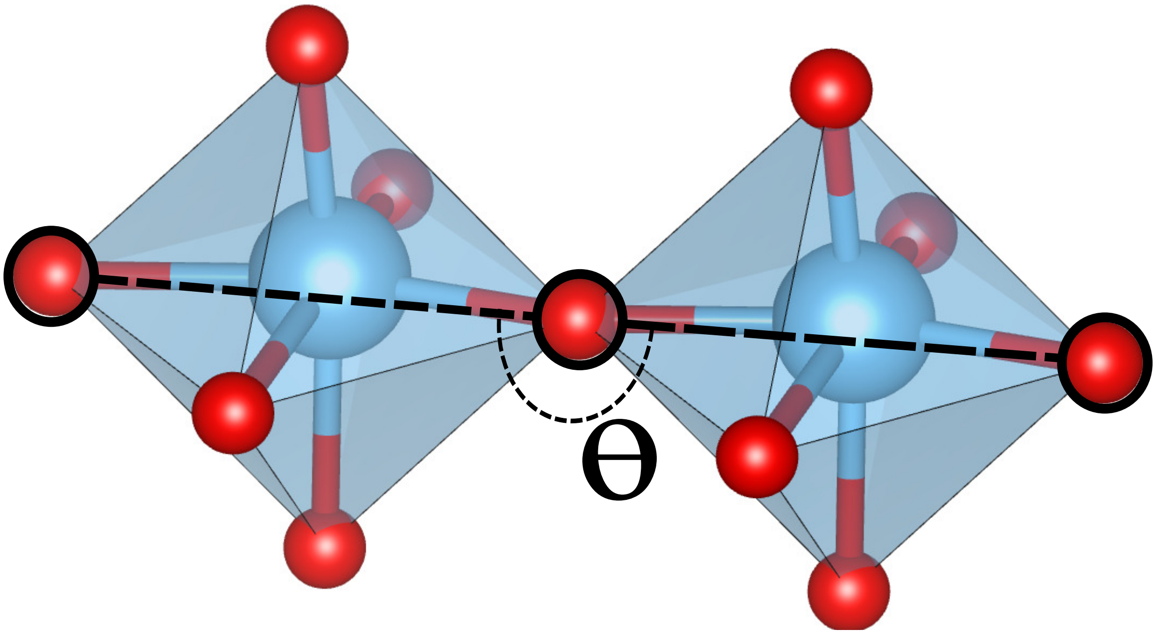

Figure 4.2: Angle potential in bond-valence model.

The potential parameters required to be fitted for $PbTiO_3$ can be summarized as follows: spring constant k for angle potential, charges q_i, scaling factors S_i and D_i for each species, and short-range repulsion parameters, B_{ij}, for each pair type (Pb-Ti, Pb-O, Ti-O and O-O). The Brown's empirical parameters ($r_{0,ij}$ and $C_{0,ij}$) are taken from Ref [125] and Ref [126]. We implemented this bond-valence model in the LAMMPS code [135].

Figure 4.3 shows our parameterization protocol. The optimization of the potential parameters is performed using simulated annealing (SA) global optimization method to fit a database of structural energy differences and atomic forces (E & $\mathbf{F}$) derived from *ab initio* DFT calculations with the ABINIT code [136]. We used the $2 \times 2 \times 2$ supercell as the reference structure. The energy and atomic forces are computed with $2 \times 2 \times 2$ Monkhorst-Pack k-point mesh [137] using PBEsol [138] as the exchange-correlation energy functional. We start with an initial database that contains the lowest-energy tetragonal structure, strained tetragonal structures, the lowest-energy cubic structure, strained cubic structures, and randomly picked orthorhombic structures with various lattice constants. After each SA run, the optimized potential parameters are used to perform constant-stress MD simulations to generate equilibrium structures at various temperatures, which are then put back to the database. The process is continued until the energies and forces of the structures sampled during MD simulations are accurately reproduced (difference between MD value and DFT value is $\approx$4 meV/atom).

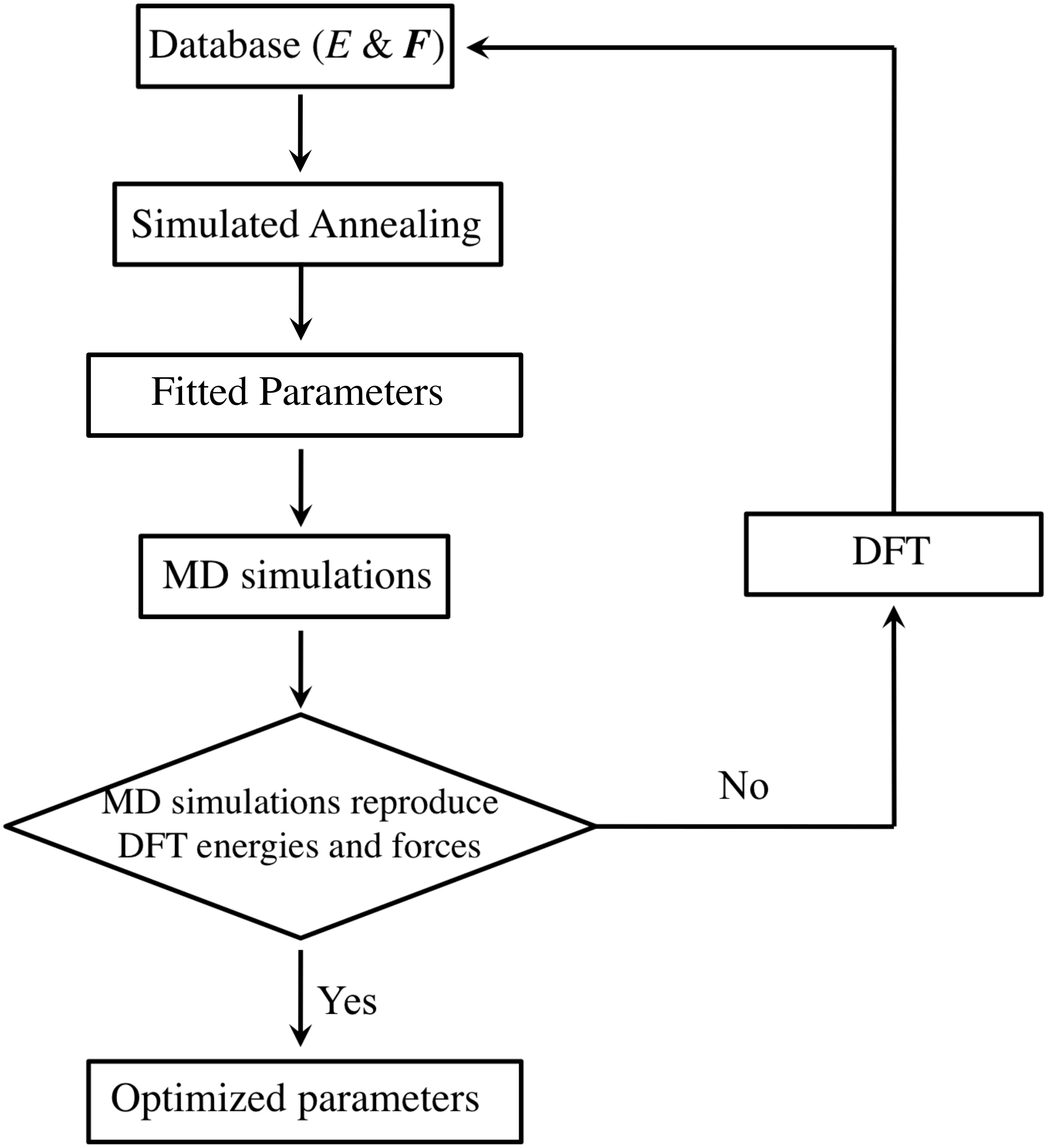

Figure 4.3: Potential optimization protocol used in this work.

4.3 Results and discussion

4.3.1 MD simulations of temperature-driven phase transition

Table 4.3.1 presents the optimized potential parameters. To account for the overestimation of the $PbTiO_3$ c/a ratio by PBEsol (c/a=1.10 versus c/a=1.07 experimentally) [139], we adjusted Brown's empirical parameter $r_{0,ij}$ to make the V_β for Pb, Ti and O reach their atomic valences in the lowest-energy tetragonal structure obtained with PBEsol. The value of preferred BVVS is then calculated with the modified $r_{0,ij}$. We find that the oxygen atoms do not have a preference for a specific value of bond-valence vector sum. This is because in perovskites, some oxygen atoms are highly displaced ($|\mathbf{W}_\mathrm{O}| > 0$), while others stay around the high-symmetry point ($|\mathbf{W}_\mathrm{O}| = 0$). So the BVVS term is included for Pb and Ti only.

Table 4.1: Optimized potential parameters of modified bond-valence model. The angle potential parameter k is 0.0152 eV/(deg)^2.

						$B_{\beta\beta'}$(Å)				
	$r_{0,\beta \mathrm{O}}$	$C_{0,\beta \mathrm{O}}$	q_β(e)	S_β(eV)	D_β	Pb	Ti	O	$V_{0,\beta}$	$\mathbf{W}_{0,\beta}$
Pb	1.960	5.5	1.38177	0.31646	2.23180	–	2.17558	1.71871	2.00	0.40297
Ti	1.798	5.2	0.99997	–	0.11888	–	–	1.28582	4.00	0.46541
O	-	-	-0.79391	1.52613	–	–	–	1.83109	2.00	–

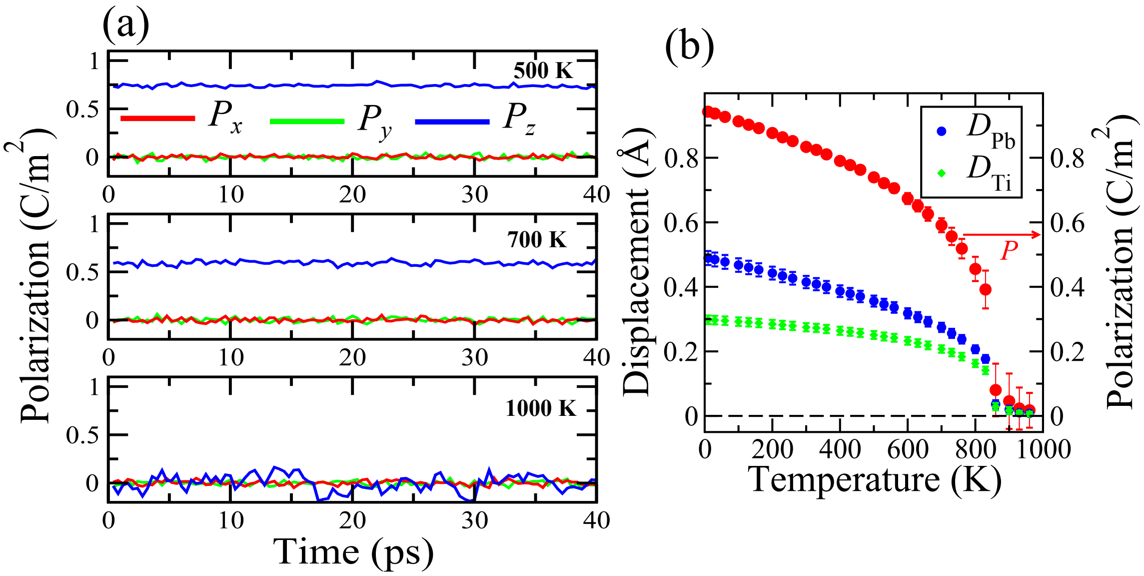

Figure 4.4: Temperature-dependent properties of PbTiO_3 obtained from NVT simulations with lattice constants fixed to experimental values. The c axis is along z direction. (a) Time evolution of components of polarization for various temperatures. (b) Spontaneous polarization and atomic displacements along the c axis as a function of temperature.

Using this optimized model potential for $PbTiO_3$, we studied the temperature dependence of lattice constants, polarization and displacements of Pb and Ti ions using an $8 \times 8 \times 8$ supercell. We first performed canonical-ensemble MD simulations with lattice constants fixed to experimental values, using the Nosé-Hoover thermostat to control the temperature. Figure. 4.4(a) shows the evolution of polarization at different temperatures: only P_z along the c axis has significant values at low temperature and the overall polarization becomes zero at and above T_c. For these simulations, we obtained 830 K for the ferroelectric-to-paraelectric first-order phase transition temperature T_c, shown in Fig. 4.4(b). This agrees well with the experimental T_c of 765 K [65], and is an improvement relative to the 550 K value obtained in NVT calculations with an earlier BV potential without BVVS term [16, 124]. We then used the new potential in NPT simulations, with the pressure maintained at 0.1 MPa by the Parrinello-Rahman barostat [123]. For the ground state structure at 10 K, we obtained the lattice constant a=3.834 Å and c/a=1.15. The equilibrium c/a ratio in MD is larger than the PBEsol DFT value [139]. Figure 4.5 displays the temperature dependence of lattice constants, spontaneous polarization and atomic displacements of Pb and Ti obtained from NPT simulations. As temperature increases, the c/a ratio decreases gradually, together with the polarization and atomic displacements. The phase transition from tetragonal to cubic occurs at 400 K, lower than the experimental value. The rather large magnitude of spontaneous polarization compared to experimental value (P = 1.25 C/m^2 vs. experimental P = 0.75 C/m^2) and the large atomic displacements at temperatures below T_c are due to the overestimated tetragonality of the PBEsol functional and some amplification of this effect in the resulting potential.

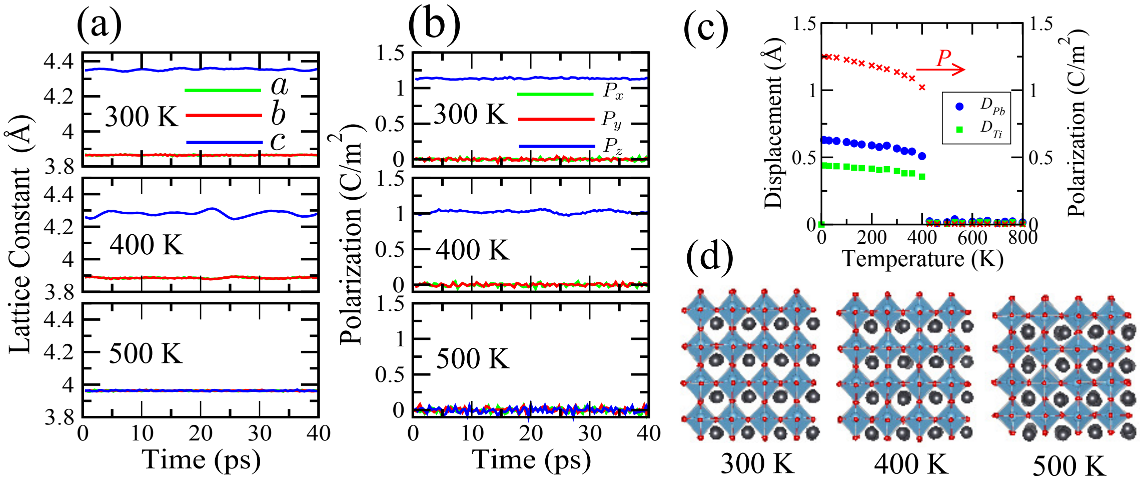

Figure 4.5: Temperature-dependent properties of $\mathrm{PbTiO_3}$ obtained from NPT simulations. Time dependence of (a) profiles of lattice constants and (b) profiles of polarization along the Cartesian axes for various temperatures. (c) Spontaneous polarization and atomic displacements as a function of temperature. (d) Snapshots of the structures of $\mathrm{PbTiO_3}$.

4.3.2 MD simulations of domain walls

We find that the new potential is capable of describing domain wall (DW) energetics and structures. The supercell used to model the domain wall is constructed following the method in Ref. 42. The domain wall energy (E_{DW}) is calculated by

$$E_{\mathrm{DW}} = \frac{E_N - E_{\mathrm{bulk}}}{S_{\mathrm{DW}}}, \tag{4.17}$$

where E_N is the energy of the supercell, E_{bulk} is the energy of a single-domain supercell of the same size, and S_{DW} is the area of the domain wall. Figure 4.6(a) presents simulation of 180° Pb-centered domain walls at 10 K. The computed domain wall energy is 208 mJ/m^2, agreeing very well with 170 mJ/m^2 obtained via PBEsol DFT calculations (with an $8\times1\times1$ supercell). To simulate a 90° domain wall, we used a supercell with $N_1 = 16$, $N_2 = 4$, and $N_3 = 4$, as shown in Fig. 4.6(b). The dimensions of the supercell are fixed to the values calculated based on experimental lattice constants of tetragonal PbTiO$_3$. The domain wall energy is estimated to be 90 mJ/m^2 and also shows a satisfying agreement with the PBEsol DFT value of 64 mJ/m^2 (with an $8 \times 1 \times 1$ supercell). We note that the BV potential is highly efficient, as all the interactions are pair-wise. This allows simulation of a 40×40×40 supercell (320,000 atoms) for 40 ps with a 1.0 fs timestep using only 2268 seconds of clocktime with 320 cores on the iBM iDataPlex supercomputer at the Navy DoD Supercomputing Resource Center.

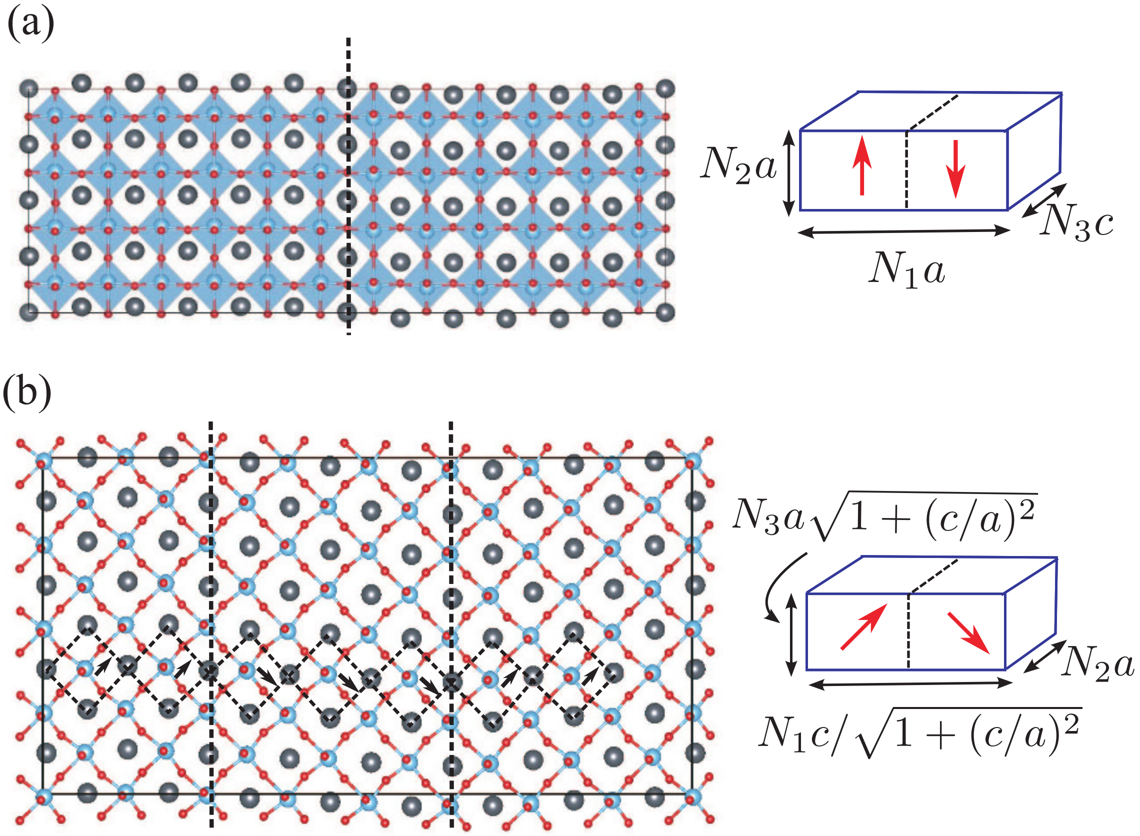

Figure 4.6: Simulated domain wall using modified bond-valence model. (a) 180° domain wall constructed with a 12×4×4 supercell; (b) 90° domain wall with $N_1 = 16$, $N_2 = 4$, $N_3 = 4$.

4.3.3 MD simulations of pressure-driven phase transition

We have also examined the performance of the potential in simulations of pressure-induced phase transitions in $PbTiO_3$ with a $10 \times 10 \times 10$ supercell. Figure 4.7 shows the pressure dependence of lattice constants and polarization. We find two phase transitions, at 6.5 GPa and 11 GPa. Below 6.5 GPa, the structure is ferroelectric. The tetragonality decreases with increased pressure and the magnitude of polarization along the long axis reduces accordingly. Above 6.5 GPa, the c/a ratio becomes 1 but the structure maintains ferroelectricity up to 11 GPa. Between 6.5 GPa and 11 GPa, we find the coexistence of multiple monoclinic phases. The polarization disappears when the pressure exceeds 11 GPa and the structure becomes centrosymmetric and paraelectric. Our simulated results are consistent with Wu and Cohen's first-principles studies [140, 141] and recent experimental results by Ahart *et al* [142]. We did not find any reentrance of ferroelectricity up to 60 GPa.

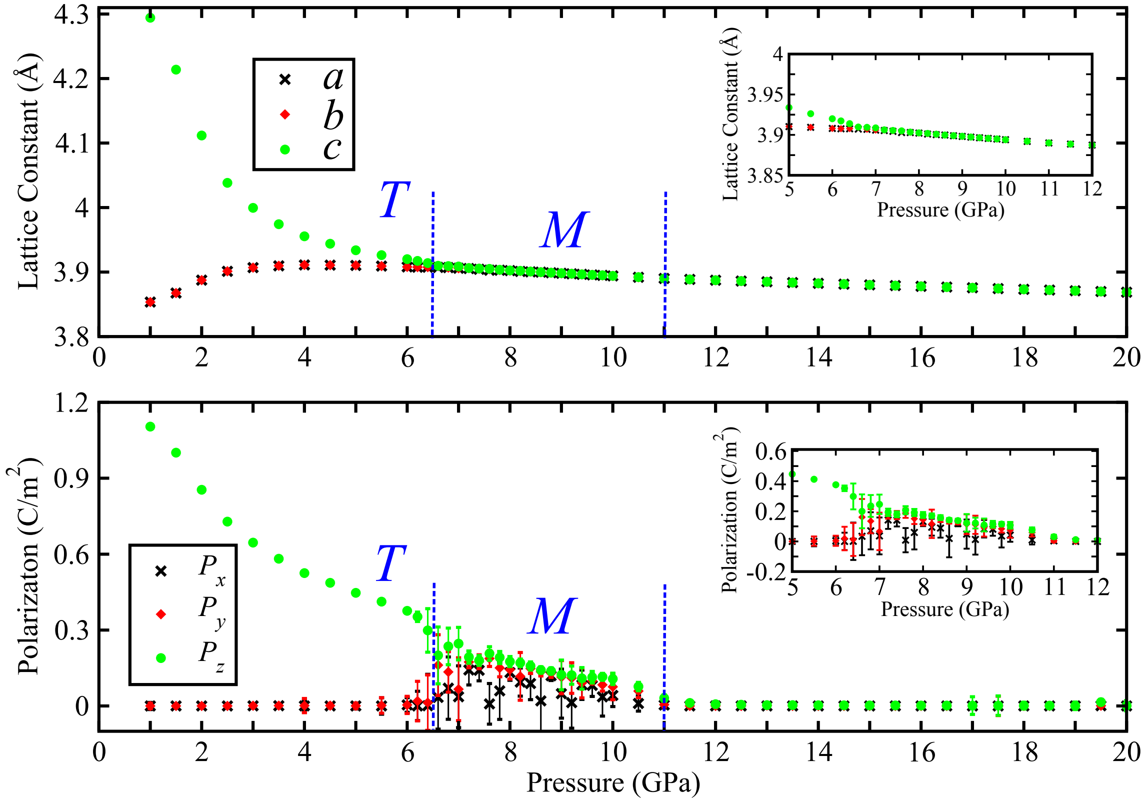

Figure 4.7: Pressure-induced phase transitions of $PbTiO_3$ obtained from MD simulations. Lattice axes coincide with the Cartesian axes (a along x, b along y and c along z).

4.4 Conclusion

We have shown that bond-valence energy is formally equivalent to the second-moment bond-order potential. The introduction of bond-valence vector energy based on the bond-valence vector conservation principle improve the bond-valence model. The new potential of $\mathrm{PbTiO_3}$ reproduces the polarization, ferroelectric instability and phase transition in NVT simulations, and also captures the temperature-driven phase transition qualitatively in NPT simulations. Both calculated 180° DW energy and 90° DW energy using this new potential are in agreement with DFT values. This new potential is efficient enough to simulate large supercells. The studies of pressure-induced phase transition with the new potential show two phase transitions, consistent with previous experimental studies. We expect that this improved bond-valence model can be applied to other oxides due to its simplicity, efficiency and accuracy. [143]

4.5 Appendix

The bond valence of an individual bond V_{ij} is defined in Eq. 4.7 to be proportional to the square of hopping integral β_{ij}. Both the bond-valence vector sum, $\mathbf{W}_i$, and the fourth-moment of the LDOS, $\mu_i^{(4)}$, can reflect the change of local symmetry of bonding environment. Figure 4.8 gives an example of a one-dimensional AB alloy. The desired bond valence of $A-B$ in the undistorted structure is set to be a, and therefore the hopping integral is equal to $\sqrt{\chi a}$, where χ is a constant. It is easy to calculate that the bond valence summation and $\mu^{(2)}$ at atom A are $2a$ and $2\chi a$, respectively. Suppose that the lattice constant and A-B bond distances are changed such that the bond-valence of the longer $A-B$ bond to $(a-\delta)$ and the shorter one becomes $(a+\delta)$. Accordingly, the hopping integral for the longer $A-B$ become $\sqrt{\chi(a-\delta)}$ and the shorter one $\sqrt{\chi(a+\delta)}$. The bond-valence conservation principle is obeyed in both structures so they cannot be distringuised at the second moment or bond-valence level. However, the $\mathbf{W}_A$ changes from zero in the undistorted structure to 2δ in the distorted structure, and the $\mu_A^{(4)}$ is reduced from $6\chi^2a^2$ to $6\chi^2a^2 - 2\chi^2\delta^2$. It is evident that only the hopping path involving the next-nearest neighbors contributes to the change of fourth-moment. Since the fourth moment hopping terms and the BVVS change at the same order, the change of fourth moment, $\Delta\mu_i^{(4)}$, can be approximated with $(|\mathbf{W}_i| - |\mathbf{W}_{i,0}|)^2$. We choose $\mathbf{W}_i^2$ instead of $|\mathbf{W}_i|$ in the formula of E_{BVV} to make sure E_{BVV} is a differentiable function for each $\mathbf{W}_i$.

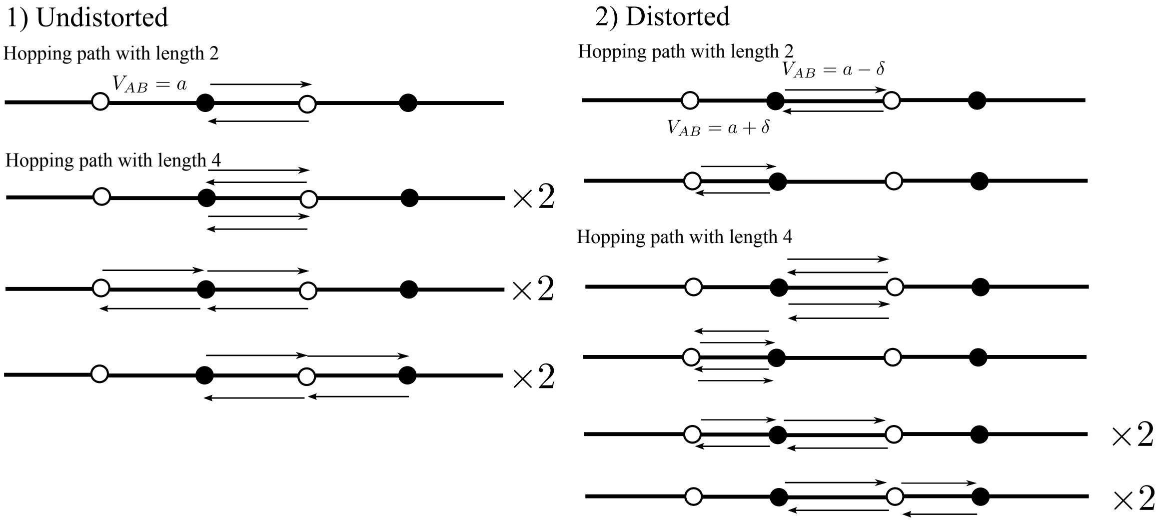

Figure 4.8: Hopping paths in one-dimensional AB alloy. Empty and filled circles represent elements A and B. The bond-valence between A and B is represented as a.

Chapter 5

Development of a bond-valence based interatomic potential for $BiFeO_3$ for accurate molecular dynamics simulation

5.1 Introduction

$BiFeO_3$ (BFO) is a multiferroic perovskite oxide with high Curie and Neel temperatures ($T_C \approx 1100$ K and $T_\mathrm{N} \approx 643$ K) [29, 30]. Recently, it has attracted intense attention, both experimentally and theoretically, due to its potential technological applications [31, 144–150]. First-principles density functional theory (DFT) calculations have been applied to study the structural, electronic, magnetic, and ferroelectric properties of $BiFeO_3$ [151–155]. However, conventional first-principles methods are limited due to their large computational cost. Bellaiche *et al.* [156] recently developed an effective Hamiltonian scheme for $BiFeO_3$, which enables the computational investigation of finite-temperature properties via Monte Carlo simulations [157, 158]. Despite this success, there is still a strong need for a true atomistic potential that could reproduce the full dynamical behavior of $BiFeO_3$ at finite temperature. However, the development of general atomistic potentials for ferroelectric oxides has proven difficult due to the complex nature of various metal-oxygen bonds [23].

5.2 Methodology

We recently developed a classical potential for $PbTiO_3$ [159] based on the bond-valence and the bond-valence vector conservation principles [24, 28]. The bond-valence conservation principle states that each atom i prefers to have the total bond valence of its bonds equal to its atomic valence, $V_{0,i}$. The actual atomic valence V_i for atom i can be calculated by summing over the individual bond valences V_{ij} for bonds between the atom and its nearest neighbors. It has been shown in many inorganic compounds that the bond valence (BV) can be modeled with an inverse power-law correlation between the bond length and bond valence [125, 126] given in Eq (1).

$$V_{ij} = \left(\frac{r_{0,ij}}{r_{ij}}\right)^{C_{ij}}, \tag{5.1}$$

where $r_{0,ij}$ and C_{ij} are Brown's empirical parameters and are readily available for many atomic pairs [24]. The bond-valence vector (BVV),$\mathbf{V}_{ij}$, is defined as a vector directed along the bond line with magnitude equal to the scalar bond valence. The bond-valence vector summation (BVVS),$\mathbf{V}_{0,i}$, is the vector sum of individual $\mathbf{V}_{ij}$ [28]. As shown in Fig 5.1, the BVVS serves as a measure of local symmetry breaking. We therefore propose that each atom is assumed to have a desired length of BVVS. The bond-valence vector conservation principle applies not only to a vast number of materials where BVVS = 0 is preferred but also to materials exhibiting noncentrosymmetric atomic environments due to electronic distortions, such as the second-order Jahn-Teller distortion for d^0 cations (Ti^{4+} and Nb^{5+}) and lone-pair driven distortion of Pb^{2+} and Bi^{3+}. The improved model potential of $PbTiO_3$ has been applied to both canonical ensemble (NVT) and isobaric-isothermal ensemble (NPT) molecular dynamics (MD) simulations. In this paper, we demonstrate that our BV model can be generalized to other materials by developing an atomistic potential for $BiFeO_3$.

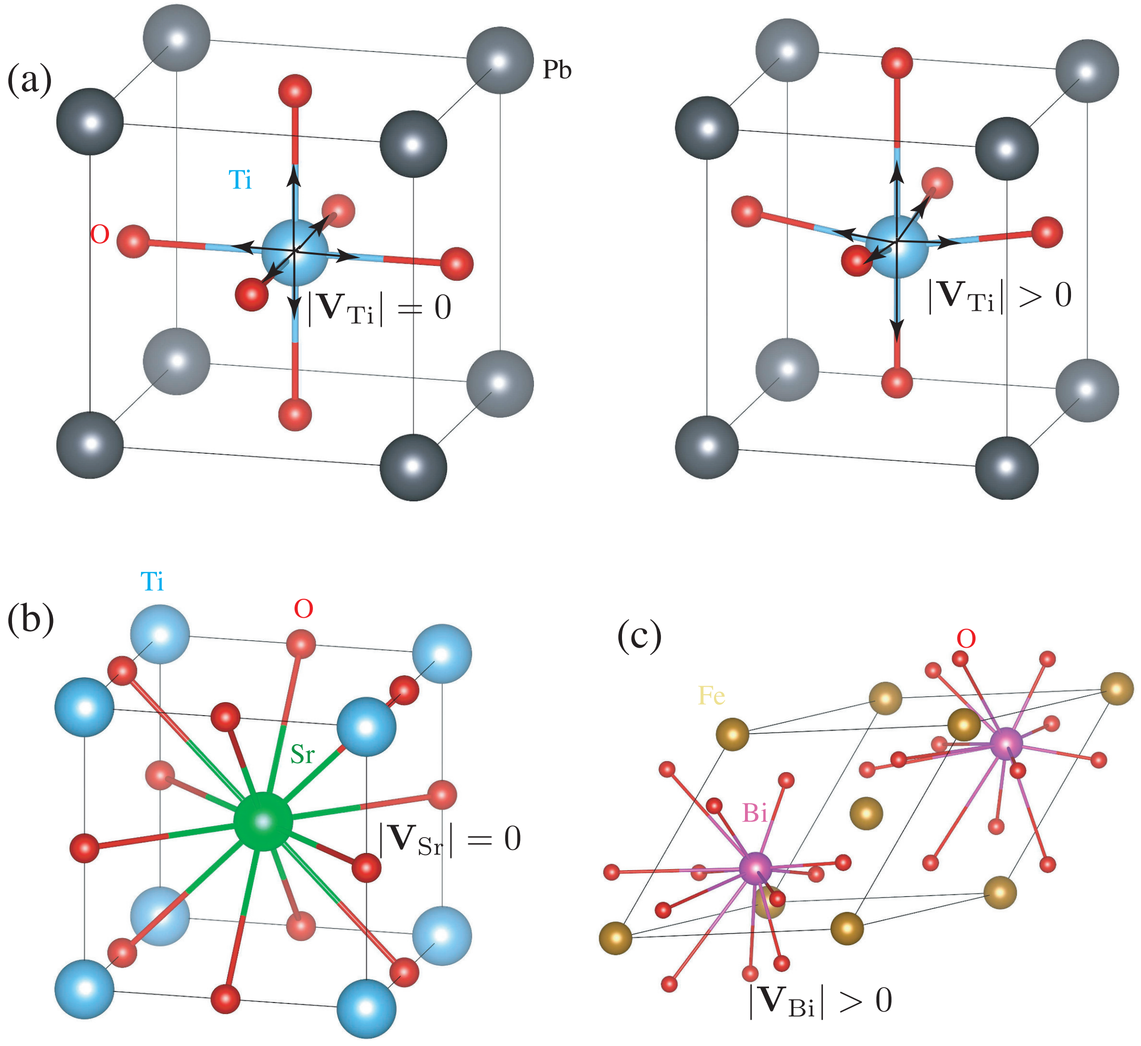

Figure 5.1: Schematic representation of bond-valence vector summation. (a) cubic $PbTiO_3$ and tetragonal $PbTiO_3$; (b) cubic $SrTiO_3$; (c) ground state $BiFeO_3$.

The total interatomic potential for BFO is given by:

$$E = E_c + E_r + E_{BV} + E_{BVV} \tag{5.2}$$

$$E_c = \sum_{i<j} \frac{q_i q_j}{r_{ij}} \tag{5.3}$$

$$E_r = \sum_{i<j} \left(\frac{B_{ij}}{r_{ij}} \right)^{12} \tag{5.4}$$

$$E_{BV} = \sum_i S_i (V_i - V_{0,i})^2, \tag{5.5}$$

$$E_{BVV} = \sum_i D_i (\mathbf{V}_i^2 - \mathbf{V}_{0,i}^2)^2 \tag{5.6}$$

where E_c is the Coulomb energy, E_r is the short-range repulsive Lennard-Jones energy, E_{BV} is the bond-valence energy, and E_{BVV} is the bond-valence vector energy. The E_{BV} and E_{BVV} will be minimized when all the ions in a crystal structure have positions satisfying the desired BVS and BVVS. We note that we recently justified the BV energy quantum mechanically in a framework of a tight-bonding model, showing that the BV energy term is formally equivalent to a second moment bond order potential, and the BVVS term is linked to the fourth moment of the local density of states [159]. Those derivations provide a firm physical basis for our BV model. The potential parameters obtained from the fitting are: charges q_i, scaling factors S_i and D_i for each species and short-range repulsion parameters, B_{ij}.

We use the simulated annealing global optimization method to optimize potential parameters by fitting a database of *ab initio*-derived structural energy differences and atomic forces. The electronic structure is calculated with the local density approximation (LDA) plus Hubbard U parameter as implemented in the QUANTUM-ESPRESSO [160] package. We use the 40-atom supercell as the reference structure. The Brillouin zone is sampled using a $4 \times 4 \times 4$ Monkhorst-Pack k-point mesh [137]. We use norm-conserving pseudopotentials [112] generated using OPIUM [161] with a plane-wave energy cutoff of 50 Ry. The initial database contains the ground-state ferroelectric rhombohedral ($R3c$) structure, strained $R3c$ structures, paraelectric rhombohedral ($R\bar{3}c$), strained $R\bar{3}c$ structures, and randomly chosen orthorhombic structures with various lattice constants. The optimized force field obtained from each simulated annealing run is used to run both constant-volume and constant-stress MD simulations to generate equilibrium structures at various temperatures, the energies and atomic forces of which are then added to the fitting database. We also used the 109° domain wall structure found by Lubk *et al.* [162] in the database to ensure correct domain wall energies. The parameterization process is continued until the force field correctly reproduces the DFT energies and atomic forces of structures sampled by MD simulations.

5.3 Results and discussion

5.3.1 MD simulations of temperature-driven phase transition

Table 5.3.1 presents the optimized potential parameters. Brown's empirical parameters $r_{0,ij}$ are tuned until $V_{0,i}$ values for Bi, Fe and O in the ground-state structure are equal to their respective atomic valences ($C_{\mathrm{BiO}} = 6.0$, $r_{0,\mathrm{BiO}} = 2.071$ Å, $C_{\mathrm{FeO}} = 5.117$, $r_{0,\mathrm{FeO}} = 1.756$ Å). The value of desired BVVS is then calculated with the modified empirical parameters. The validity of the potential is first tested via constant-volume MD simulations at various temperatures with lattice constants fixed to experimental values. [31] For these simulations, we used a 5120-atom rhombohedral supercell ($a = b = c = 44.64$ Å, $\alpha = \beta = \gamma = 60°$) and the Nosé-Hoover thermostat to control the temperature. Figure 5.2(a) shows the temperature dependence of polarization along the [111] axis. The simulations show a ferroelectric-to-paraelectric first-order phase transition at T_c=760 K. Analysis of local displacements (Fig. 5.2(b)) shows that at $T < T_c$, all displacements are only along the [111] direction. At $T > T_c$, the local displacements are non-zero but are evenly split between the positive and negative directions, resulting in no net polarization. This behavior is characteristic of the order-disorder phase transition. The magnitude of the local displacements decreases with temperature, which is characteristic of the displacive phase transitions. We therefore conclude that the phase transition is of the mixed order-disorder and displacive phase character, as is typical for ferroelectrics.

Table 5.1: Optimized potential parameters for $BiFeO_3$.

				B_{ij}(Å)				
	q_β(e)	S_β(eV)	D_β	Fe	Bi	O	$V_{0,\beta}$	$\mathbf{V}_{0,\beta}$
Fe	1.93753	0.84065	–	–	1.70139	1.48115	3.00	0.01798
Bi	1.77706	0.70313	0.76798	–	1.78529	1.77085	3.00	0.87373
O	-1.23820	0.67213	4.50044	–	–	1.39114	2.00	0.32866

We then used the potential in NPT simulations. The external stress is maintained at 0.1 MPa by the Parrinello-Rahman barostat. We used a 2560-atom perovskite-type orthorhombic supercell as the starting structure. Figure 5.3 depicts the evolution of polarization and atomic displacements with temperature. At low temperature, all three components of polarization, P_x, P_y and P_z, have significant values with small fluctuation, such that the overall polarization points toward the [111] direction. As the temperature increases, the magnitude of the polarization decreases. At high temperature (700 K), P_x, P_y and P_z all become zero, indicating a paraelectric structure. Therefore, the T_c obtained from NPT MD simulation is 660 K. This underestimates the experimental T_c of 1100 K. Such underestimation is consistent with the previously found underestimation of T_c in NPT BVMD $PbTiO_3$ simulations [163]. The difficulty of reproducing experimental T_c appears to be a general feature for both atomistic simulation using interatomic potential [12, 164] and the effective Hamiltonian scheme [21, 165–167]. We believe that this systematic error is partly due to the use of LDA functional in potential parametrization. DFT calculations with LDA functionals are known to underestimate the experimental lattice constants and P values. Since in perovskites T_c scales as P^2, smaller P magnitude leads to underestimation of theoretical T_c. The underestimation of T_c may also be partially due to an imperfect representation of the DFT potential by the atomistic force-field model. Since our bond-valence model is essentially a simplified fourth-moment bond-order potential, introducing new energy terms that utilize higher moments may further improve its performance.

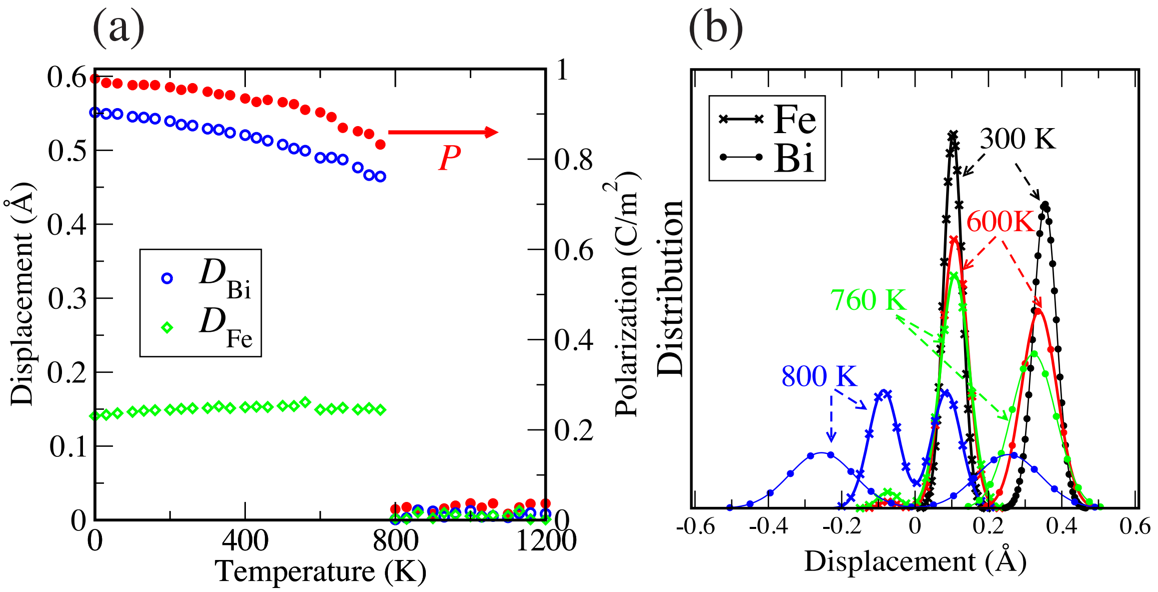

Figure 5.2: Temperature-dependent properties of BiFeO_3 obtained from NVT simulations. (a) Spontaneous polarization and average atomic displacements of Bi and Fe along the [111] axis for BiFeO_3. (b) Probability distributions of atomic displacements along [100] axis. The atomic displacements along [010] and [001] show similar distributions.

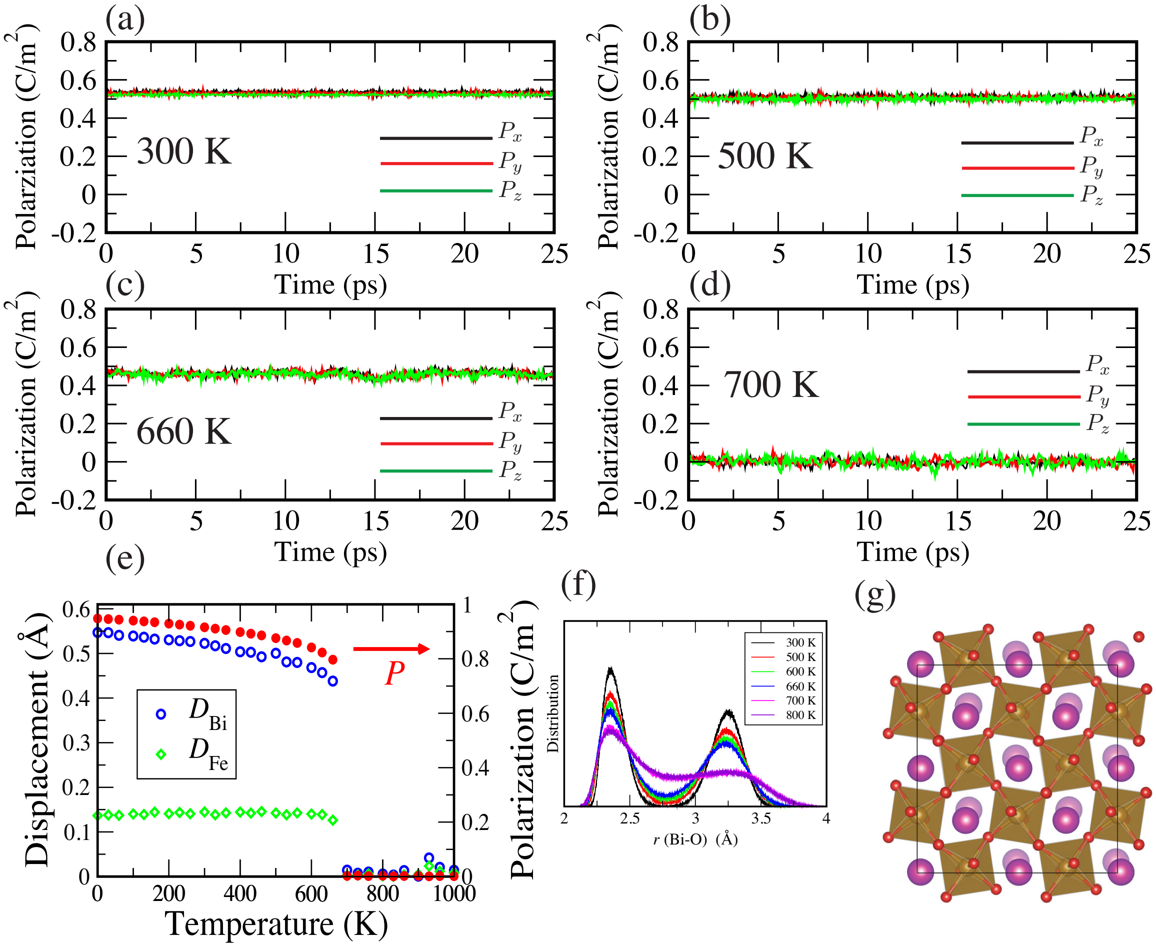

Figure 5.3: Temperature-dependent properties of $BiFeO_3$ obtained from NPT simulations. (a)-(d) Evolution of polarization along Cartesian axes. (e) Spontaneous polarization and atomic displacements along the [111] axis as a function of temperature.(f) Pair distribution function for Bi-O atomic pair as a function of temperature. (g) Oxygen octahedral tilting in $BiFeO_3$ at 700 K along c axis.

Analysis of local structure shows that below T_c the displacements of Fe^{3+} ions with respect to the center of their oxygen octahedra do not change with temperature significantly. On the other hand, the displacement of Bi^{3+} shows a stronger temperature dependence, with a strong decrease as temperature increases. This agrees with previous experimental studies [168, 169] which found that the shift of Bi^{3+} makes the main contribution to the temperature changes of the electric polarization of BiFeO$_3$. It is also found that the pair distribution function (PDF) for Bi-O atomic pair exhibits two well separated peaks below T_c, and then become more dispersed above T_c. This indicates the change of the coordination number of Bi during phase transion, which supports the $R3C$ to $Pbnm$ phase transition reported previously [169]. The time-averaged structure of the paraelectric phase (averaged with 500 structures obtained from a 20 ps MD simulation) is close to the structure of GdFeO$_3$, which shows octahedral tilting of $a^-a^-b^+$, typical for perovskite with space group $Pbnm$ (Figure 3(g)). This further supports the assignment of $Pbnm$ as the space group of the paraelectric phase.

5.3.2 MD simulations of domain walls

Domain structure and dynamics play important roles in ferroelectric switching, photovoltaic effects and other phenomena intensely studied in BiFeO$_3$. To further test the potential and its applicability to the study of BFO domain walls, we calculate the energies of 71°, 109°, and 180° domain walls. The domain wall energy is estimated using:

$$E_{\mathrm{DW}} = \frac{E_N - E_{\mathrm{bulk}}}{S_{\mathrm{DW}}} \tag{5.7}$$

where E_N is the energy of the supercell containing the domain wall, E_{bulk} is the energy of the bulk BiFeO$_3$ supercell of the same size, and S_{DW} is the domain wall area. For BFO, the DW structure is particularly interesting, as recent DFT calculations by Diéguez *et al.* [170]

found that several local minima are possible for the domain walls with up to factor of three difference in DW energy for the same DW orientation, compared to the values reported by Lubk *et al* [162]. The three low-energy and three high-energy DW structures found by Lubk *et al.* and Diéguez *et al.* therefore provide a stringent test of our potential, which as stated above, was parameterized using only the high-energy 109° wall.

To assess the accuracy of our BV potential, we carried out NPT simulations at 10 K using supercells shown in Fig. 5.4. The 71° wall was constructed with $6\sqrt{2} \times 2\sqrt{2} \times 4$ supercell with domain boundary in the (110) plane; the 109° domain wall was simulated with a $12 \times 2\sqrt{2} \times 2\sqrt{2}$ supercell with the boundary in (100) plane and polarization vector changing from $[1\bar{1}\bar{1}]$ to [111] across the domain wall; a $6\sqrt{2} \times 2\sqrt{2} \times 4$ supercell was used for constructing the 180° domain wall with boundary in the (110) plane. We found DW energies of 372 mJ/m^2, 232 mJ/m^2, 1032 mJ/m^2 for the 71°, 109° and 180° high-energy walls, respectively. For the low-energy DWs, we found 156 mJ/m^2, 34 mJ/m^2 and 110 mJ/m^2 for the 71°, 109° and 180° walls. These values compare favorably with 363 mJ/m^2, 205 mJ/m^2, 829 mJ/m^2, 167 mJ/m^2, 62 mJ/m^2 and 82 mJ/m^2 DW energies obtained by the corresponding DFT calculations [162, 170]. The agreement between DFT and atomistic potential values is quite good and indicates that our atomistic potential accurately reproduces the $BiFeO_3$ potential energy surface. We emphasize once again that this agreement was achieved while only using the high-energy 109° structure in potential parameterization and is due to the firm physical basis of the potential.

5.4 Conclusion

In this work, we present an atomistic interatomic potential for $BiFeO_3$ based on the bond-valence and the bond-valence vector conservation principles. This model potential reproduces the ferroelectric to paraeletric phase transition and the temperature dependence of

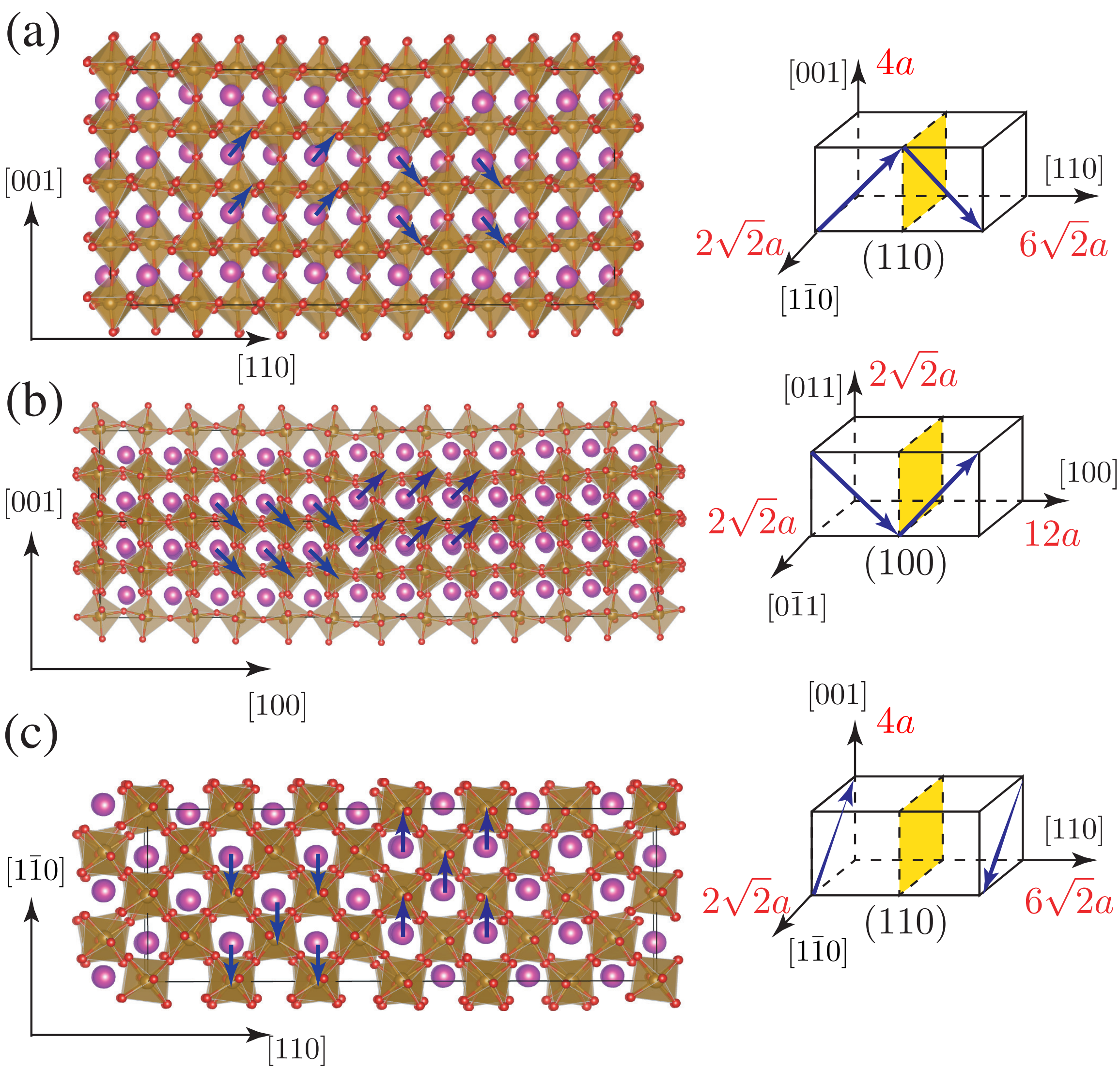

Figure 5.4: Simulated domain wall structures using the BV potential of $BiFeO_3$. (a) 71°; (2) 109°; (3) 180°. Dimensions of each supercell are given in units of the lattice constant a. The blue arrow represents the direction of polarizations.

local cation displacements in $\mathrm{BiFeO_3}$ in both NVT and NPT simulations. The calculated energies of various domain walls are also in agreement with DFT results. We believe that the bond-valence model approach achieves a balance between efficiency, accuracy, and transferability and we therefore expect that this type of interatomic potential will be applicable to a broad range of oxides.

Chapter 6

Exploration of the intrinsic inertial response of ferroelectric domain walls via molecular dynamics simulations

6.1 Introduction

Ferroelectric materials have been studied intensely due to their numerous important technological applications in electronics, optics, and acoustics [1, 4, 171, 172]. In many cases, ferroelectrics adopt a multi-domain state where domains with polarization uniformly oriented in one direction are bounded by domains with polarization pointing in other directions. The boundary separating regions of different polarity is called the domain wall (DW) [1]. The DW can be moved by external electric field and stress, causing one region to grow. Therefore, controlling DW motion is critical to applications of ferroelectric materials such as non-volatile random access memory [2, 3, 5, 173]. Though ferroelectric materials have been studied for more than fifty years, the microscopic understanding of how different types of DWs form and move remains incomplete.

One unanswered question that is of interest both scientifically and technologically is whether ferroelectric DWs exhibit real momentum and significant inertial response. It is generally reported that a ferroelectric DW, the motion of which involves movements of atoms, has real inertia, whereas the magnetic DW, which is due to the flipping of massless spins, has no momentum [174, 175]. However, these claims has been challenged recently for both ferroelectric and magnetic DWs [176–179]. For magnetic domains, experimental studies reveal that magnetic DWs can exhibit significant momentum and inertial response [178, 179]. For ferroelectrics, the inertial response of a DW can be evaluated by examining its behavior after the driving force is removed. This effect is currently a subject of debate. Dawber *et al.* [180] observed that the ferroelectric DW travels from the perimeter to the center in a circular capacitor: once the wall motion is initiated, it propagates with viscous drag, which they attributed to the coupling of the domain wall to acoustic phonons. The good agreement between the measured dependence of impedance response on capacitor perimeter and theoretical predictions with a simple one-dimension phonon drag equation suggests that the ferroelectric DW has significant inertial response. Similar deceleration of the DW under applied field was observed by Kim *et al.* [181] and also assigned to ballistic character of DW motion. However, Molotskii *et al.* [176] later pointed out that Dawber *et al.* used a high value of the relaxation time ($\tau \approx 50$ ns). After using a much smaller τ ($\approx 10^{-4}$ ns) derived from the effective DW mass reported by Kittel [182], Molotskii *et al.* obtained a post-field propagation distance around 10^{-10} m, which is smaller than the lattice constant [176]. Furthermore, recent in-situ investigations of the dynamics of superdomain (a-c domain bundles) boundaries in $BaTiO_3$ with piezoresponse force microscopy (PFM) also indicated that the DW stops when the external voltage is turned off [177]. The presence or lack of the domain wall momentum can have both extrinsic or intrinsic origins. To elucidate the *intrinsic* inertial response, we perform molecular dynamics (MD) simulations of ferroelectric DWs.

6.2 Methodology

To model the dynamics of DWs, the simulation of a large system at finite temperature is required. We have recently developed an interatomic potential based on bond-valence theory [14, 16, 24, 25, 143, 159]. The model potentials for two ferroelectric materials, $PbTiO_3$ and $BiFeO_3$, have been parameterized based on first-principles results [143, 159]. The optimized potential is accurate for both constant volume (NVT) and constant pressure (NPT) conditions and sufficiently efficient for large-scale (≈1,000,000 atoms) molecular dynamics (MD) simulations. In this work, we use MD simulations to study the momentum of DWs in the classic $PbTiO_3$ ferroelectric. As shown in Fig. 6.1, the 180° DW (the wall separating regions with antiparallel polarization) is constructed with a $24 \times 8 \times 8$ supercell with polarization aligned along z axis. The 90° DW (the wall separating regions with perpendicular polarization) is modeled with a $40 \times 40 \times 40$ supercell with alternating domains having polarization in the xy plane.

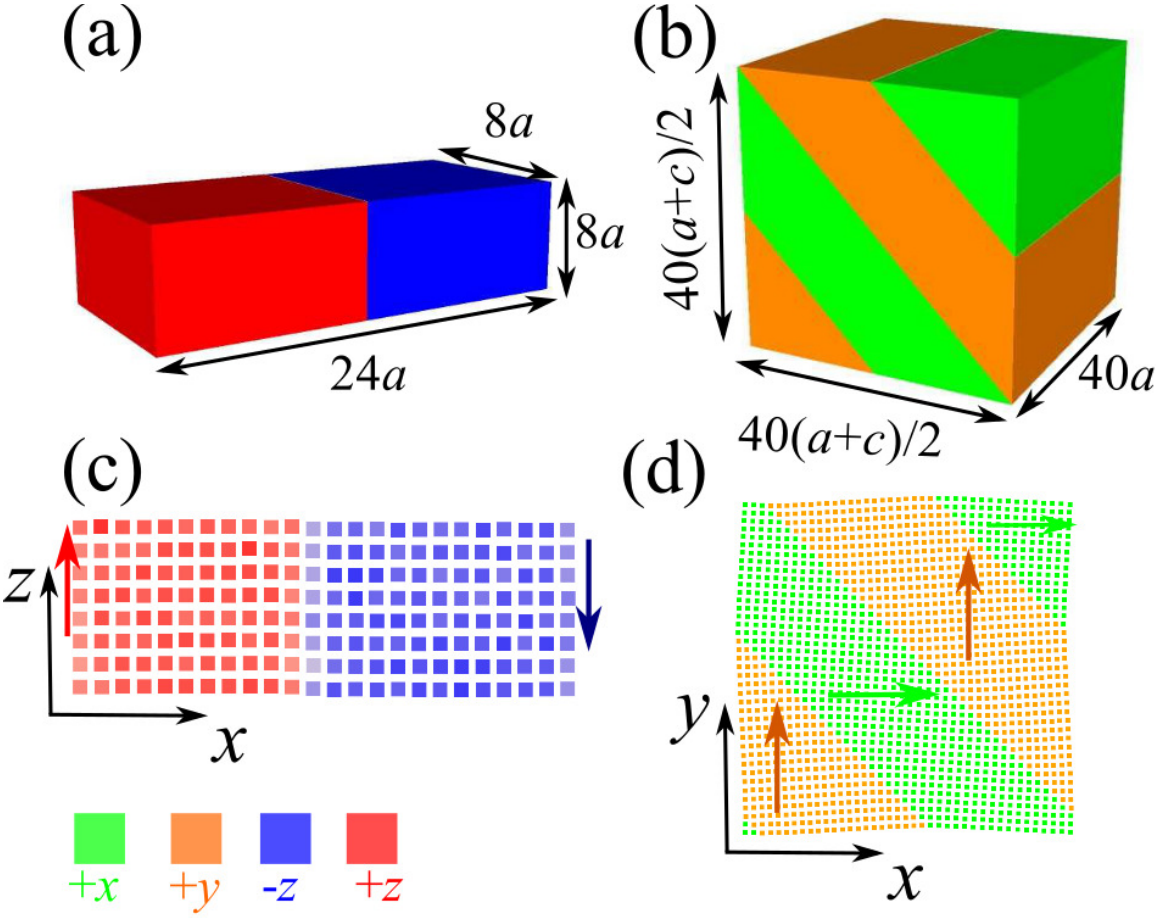

Figure 6.1: Domain walls in PbTiO$_3$. (a) $24 \times 8 \times 8$ supercell used for 180° DW. (b) $40 \times 40 \times 40$ supercell used for 90° DW. (c) domain pattern of 180° DW in xz plane. (d) domain pattern of 90° DW in xy plane. Each cell is colored based on the direction of the dipole: green for $+x$, orange for $+y$, red for $+z$, and blue for $-z$.

6.3 Results and discussion

6.3.1 Domain structures at finit temperature

We perform NPT MD simulations with a Parrinello-Rahman barostat as follows: first, the DW motion is initiated by applying an external electric field for a period of time; then the field is turned off allowing the DWs to evolve freely. If the DW does indeed have momentum, it will keep moving after the electric field is removed. Given that accurate determination of the DW position is critical for the evaluation of momentum, we first determined the thickness of DWs. As shown in Fig. 6.2, we calculated the averaged polarization for each layer of cells across the DWs at temperatures from 10 K to 240 K. We found that the 180° DW is 1-2 unit cells thick, while the width of 90° DW is 4-5 unit cells (the half width of the polarization profile around the domain boundary) at finite temperature. In this study, we propose that only when a DW moves inertially by a distance comparable to the width of a DW, the inertial response can be regarded as "significant".

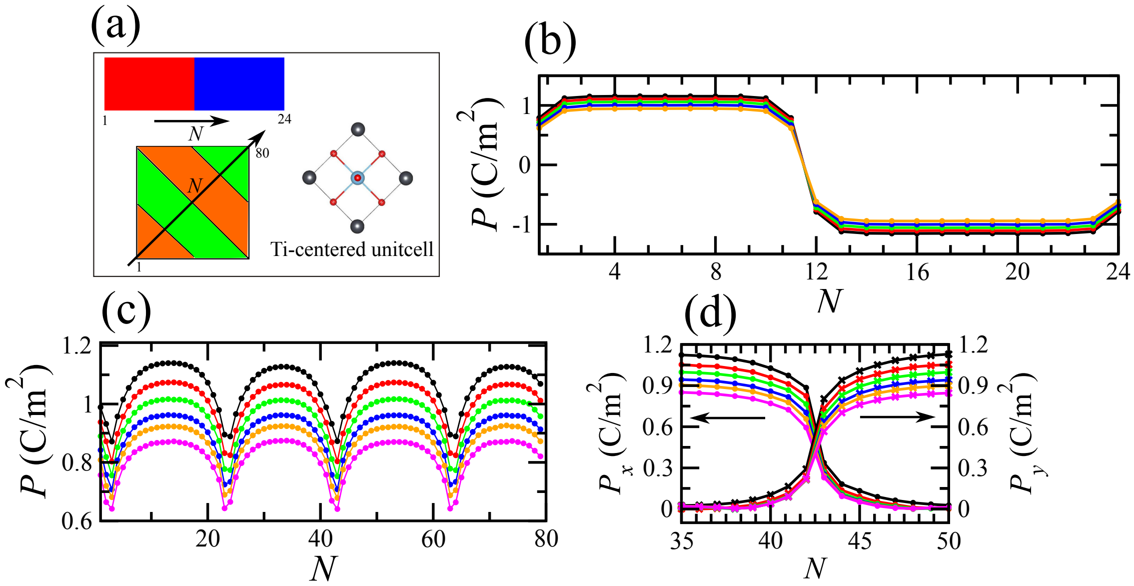

Figure 6.2: (a) Illustration of our choice of layer index, N, in DWs. The Ti-centered unit cell is used for local polarization calculation. (b)-(c) Temperature-dependent polarization profiles across the 180° DW and the 90° DW. (d) Temperature-dependent x-component and y-component polarization profiles across the 90° DW from layer N=35 to layer N=50. Lines with different color represent different temperatures: black, 10 K; red, 100 K; green, 160 K; blue, 200 K; orange, 220 K; magenta, 240 K.

6.3.2 Inertial response of 180° DW

The change of the overall polarization of the supercell directly reflects the DW motion. Figure 6.3 presents the change of P_z for 180° DW under various pulses at 220 K. As the electric field is applied along $+z$ direction, the magnitude of P_z increases, indicating the field-driven movement of DW along $+x$. Once the field is turned off, two types of equilibrations are observed: 1) the magnitude of P_z is reduced until it reaches equilibrium, for example for $E = 1.8$ MV/cm, t_E=4 ps; 2) the magnitude of P_z first decreases, then increases by a small amount and eventually equilibrates, for example $E = 2.2$ MV/cm, t_E=4 ps. To elucidate the origins of these two types of equilibrations, we examined the structure of 180° DW by analyzing the evolution of the local polarizations in the supercell. Figure 6.4 presents the change of the polarization profile in response to a 4 ps-long electric field pulse. The drop of P_z at the instant of field removal results mainly from the reduction in the magnitudes of local dipoles that were aligned with the applied field ($+z$) and the increase in the magnitude of the dipoles pointing toward $-z$. When the field is removed, both types of dipoles return to their zero-field values. More importantly, both the polarization profiles and the visualized domain patterns show that the position of the DW does not change once the field is removed, which suggests that the 180° DWs do *not* have inertial response. The two types of polarization responses are actually caused by the growth or annihilation of a nucleus at the domain boundary. At 4 ps, we see from Fig. 6.4(a) that the local dipoles in layer $N = 16$ were partially switched at the time of field removal. Similarly, in Fig. 6.4(b), it is observed that the switching process in layer $N = 16$ has already started, but has not yet finished. This means the domain wall is not flat during the motion. Figure 5 shows the changes of the dipoles in these two layers in the absence of electric field. We can see that at 4 ps, the nucleus (number of red squares) in $N = 16$ (E=1.8 MV/cm) is small and eventually disappears, resulting in the reduction of the polarization (Type 1 response). This is consistent with experimentally observed backswitching of the domain boundary after the driving electric field is removed [177]. On the other hand, the size of nucleus in layer $N = 16$ (E = 2.2 MV/cm) is already large; therefore, the nucleus can keep growing until the whole layer becomes $+z$ polarized. This spontaneous switching process is responsible for the increase of the polarization (Type 2 response). We therefore suggest that after the electric field is turned off, only the layers in which the size of nucleus exceeds the critical size will finish the switching process in the absence of electric field. The cessation of DW motion at the instant of field-removal is a direct consequence of the intrinsic energy barrier for nucleation. We would like to note here the difference between a phonon and a DW. The motion of a phonon and a DW both involve the displacements of atoms. However, phonons are distortions away from a *single* local minimum in the structural phase space; displacing one atom creates forces on its neighbors, leading to the propagation of a phonon wave. By contrast, when a ferroelectric bicrystal is at rest, atoms are located in *one of the two* local minima ($+z$ or $-z$ domain) and are not under any force. A traveling DW, as we showed, moves one plane of atoms from one local minimum ($-z$ domain) to another local minimum ($+z$ domain). Therefore, during DW motion there is no restoring force that would cause the atoms in nearby unit cells to switch the direction of their off-center ferrroelectric distortion.

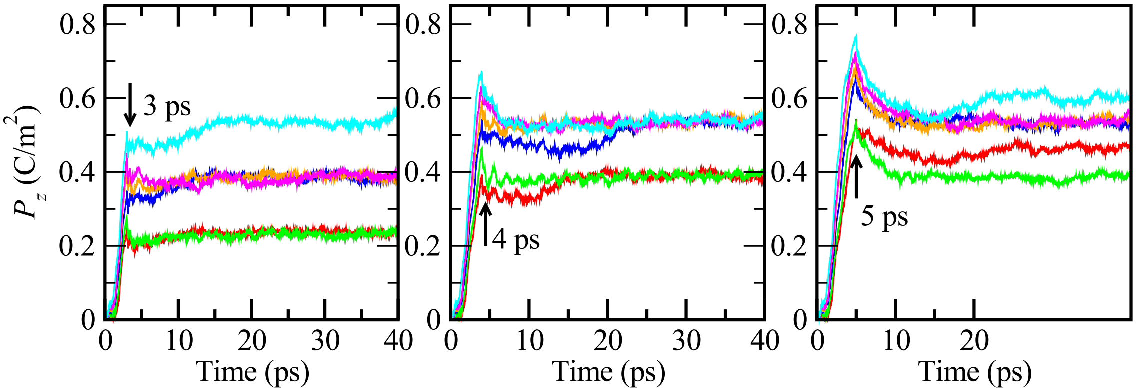

Figure 6.3: The evolution of z-component polarization of 180° DW in response to electric filed pulse. Lines with different color represent different electric fields: red, 1.8 MV/cm; green, 2.0 MV/cm; blue, 2.2 MV/cm; orange, 2.4 MV/cm; magenta, 2.6 MV/cm; cyan, 2.8 MV/cm. The electric field is turned off at 3 ps, 4 ps, and 5 ps, respectively.

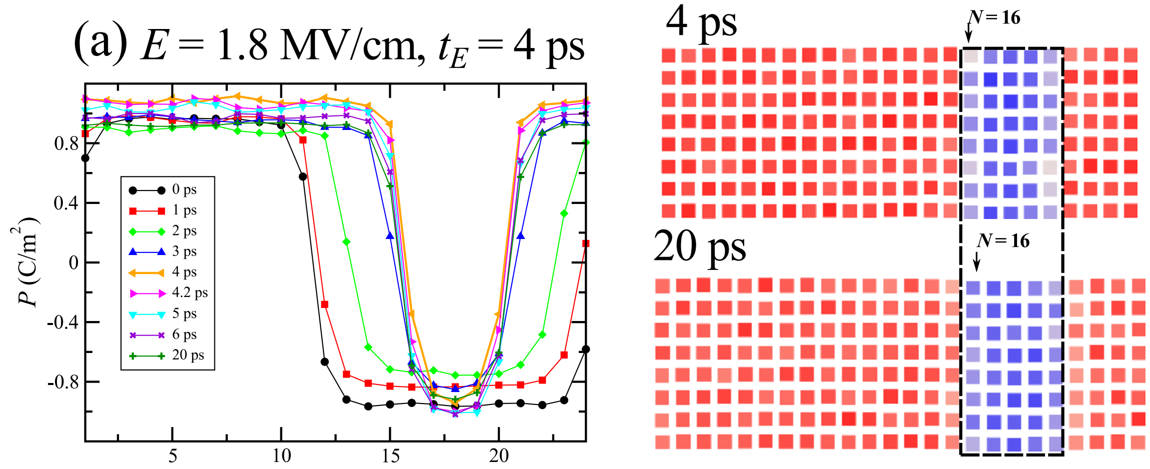

(a) $E = 1.8$ MV/cm, $t_E = 4$ ps

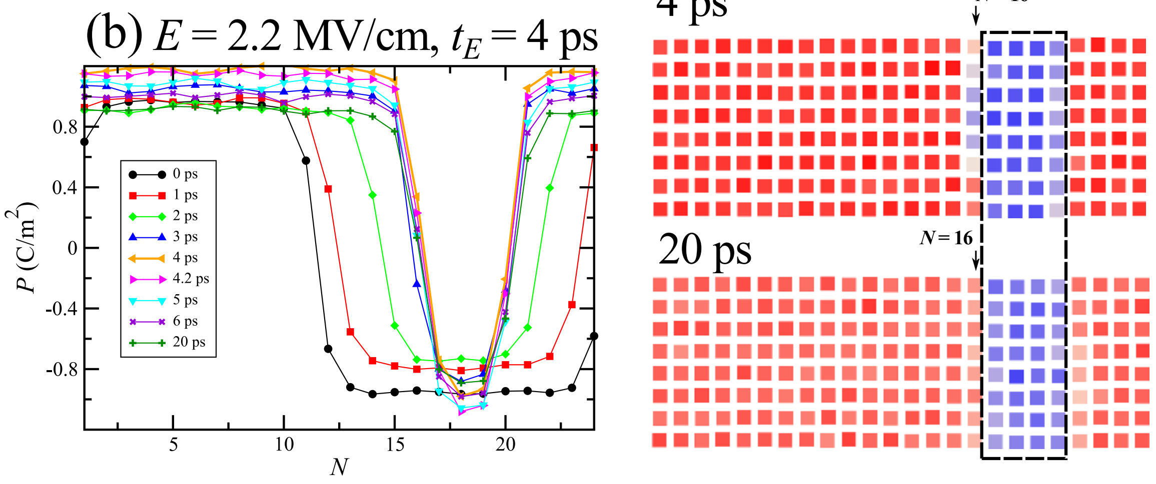

(b) $E = 2.2$ MV/cm, $t_E = 4$ ps

Figure 6.4: Evolution of the polarization profiles (left) and domain patterns (right) of a 180° DW in $PbTiO_3$.

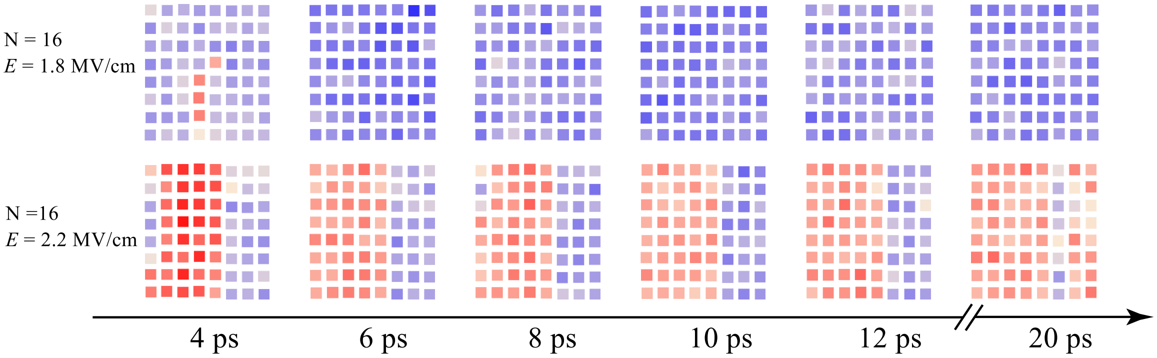

Figure 6.5: Schematic representation of nucleus annihilation (top) and growth (bottom) at domain boundary. The electric field is turned off at 4 ps.

The experimental studies cited above [177, 180, 181] have found that the DW velocity under applied field is time-dependent and the speed of DW at a given time depends on the initial velocity and damping. However, according to Merz's law, DW velocity depends only on the strength of the applied field at the given time [33]. To investigate whether there is any memory of previous conditions in the intrinsic DW motion mechanism, we carried out two sets of simulations. In one set of simulations, the DWs are initially driven by electric fields of different magnitudes and then the field magnitudes are changed to the same value for all simulations. In another set of simulations, the same electric field is applied initially for all simulations, followed by the application of different electric fields. Figure 6.6 shows the time evolution of the polarization obtained by using this protocol in NVT simulations with a $48 \times 8 \times 8$ supercell. The slope of the polarization profile, k, specifies the speed of the DW. As shown in Fig. 6.6(a), the DWs that experience a higher initial field show larger velocities before 6 ps. For $t > 6$ ps, the field is set to the same value for all simulations, all DWs show nearly identical velocities, regardless of their initial launching velocities. The dramatic difference in the velocities before and after 6 ps is illustrated in the insert in Fig. 6.6(a). From Fig. 6.6(b), we find that the velocities of DWs under different fields follow Merz's law, $\ln v \propto 1/E$ [33]. Our simulations show that the velocity of the DW does not depend on the initial velocity and has no time dependence, dissimilar to a ballistic motion. Instead, the velocity follows Merz's low and is solely dependent on the magnitude of the external electric field. This further demonstrates that the 180° DW has little or no intrinsic inertial response.

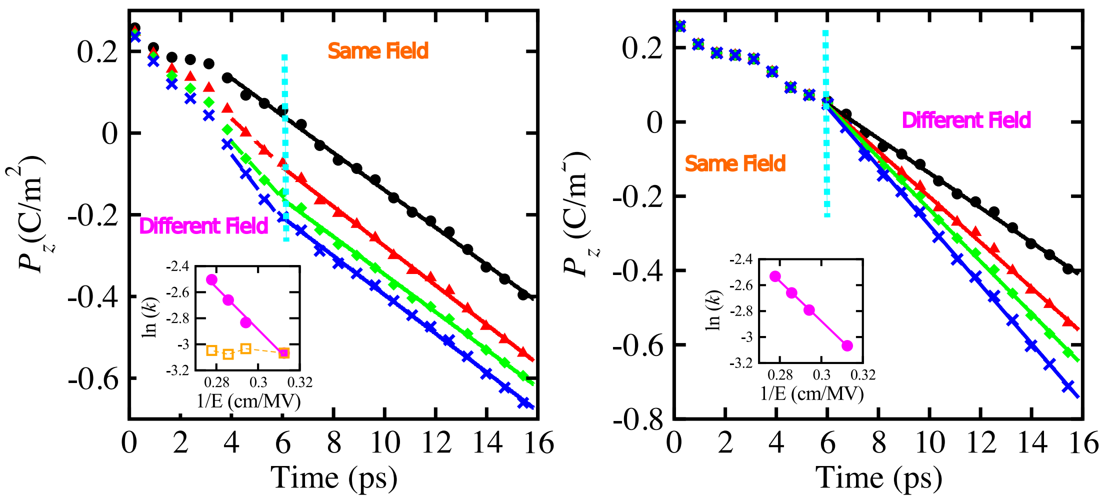

Figure 6.6: Evolution of the polarization of a 180° DW under sequentially applied electric fields of different magnitudes. The electric field is applied along $-z$ direction. Symbols with different colors represent different electric fields: black, 3.2 MV/cm; red, 3.4 MV/cm; green, 3.5 MV/cm; blue, 3.6 MV/cm. For a given electric field, 20 simulations starting with different initial equilibrated structures are performed to get the averaged polarization profile. (a) Different electric fields are applied until 6 ps and then switched to the same electric field (3.2 MV/cm). The inset illustrates the dependence on the DW velocity on the initial applied field for $t < 6$ ps (magenta) and $t > 6$ ps (orange). (b) The electric fields of the same magnitude (3.2 MV/cm) is applied until 6 ps and then switched to different electric fields. The inset shows that the speed of a domain wall follows Merz's law.

6.3.3 Inertial response of 90° DW

We now examine the 90° DWs. The evolution of P_x for 90° DW in response to different electric-field pulses at 200 K is shown in Fig. 6.7. Since the 90° DW energy is known to be about four times lower than 180° DW energy [79], much smaller electric fields were applied along $+x$ direction. The increased magnitude of x-component of total polarization under electric field again indicates the movement of DWs driven by field. Similar to what was found for 180° DWs, the removal of electric field results in a decrease of P_x. Figure 6.8 shows the changes of domain patterns and P_x profiles for a 4 ps 0.4 MV/cm electric pulse. The motion of 90° DW (highlighted as red broken line) is evident from 0 ps to 4 ps. The overall result is an increase of the area of field-favored domains at the expense of the domains with dipoles oriented opposite to the field. After the field is turned off, the positions of the DWs from 4 ps to 20 ps did not change (Fig. 6.8b), suggesting that 90° DW also does *not* have physically meaningful intrinsic inertial response. The main effect after the field removal is the structural relaxation leading to reduction of the x-component polarizations.

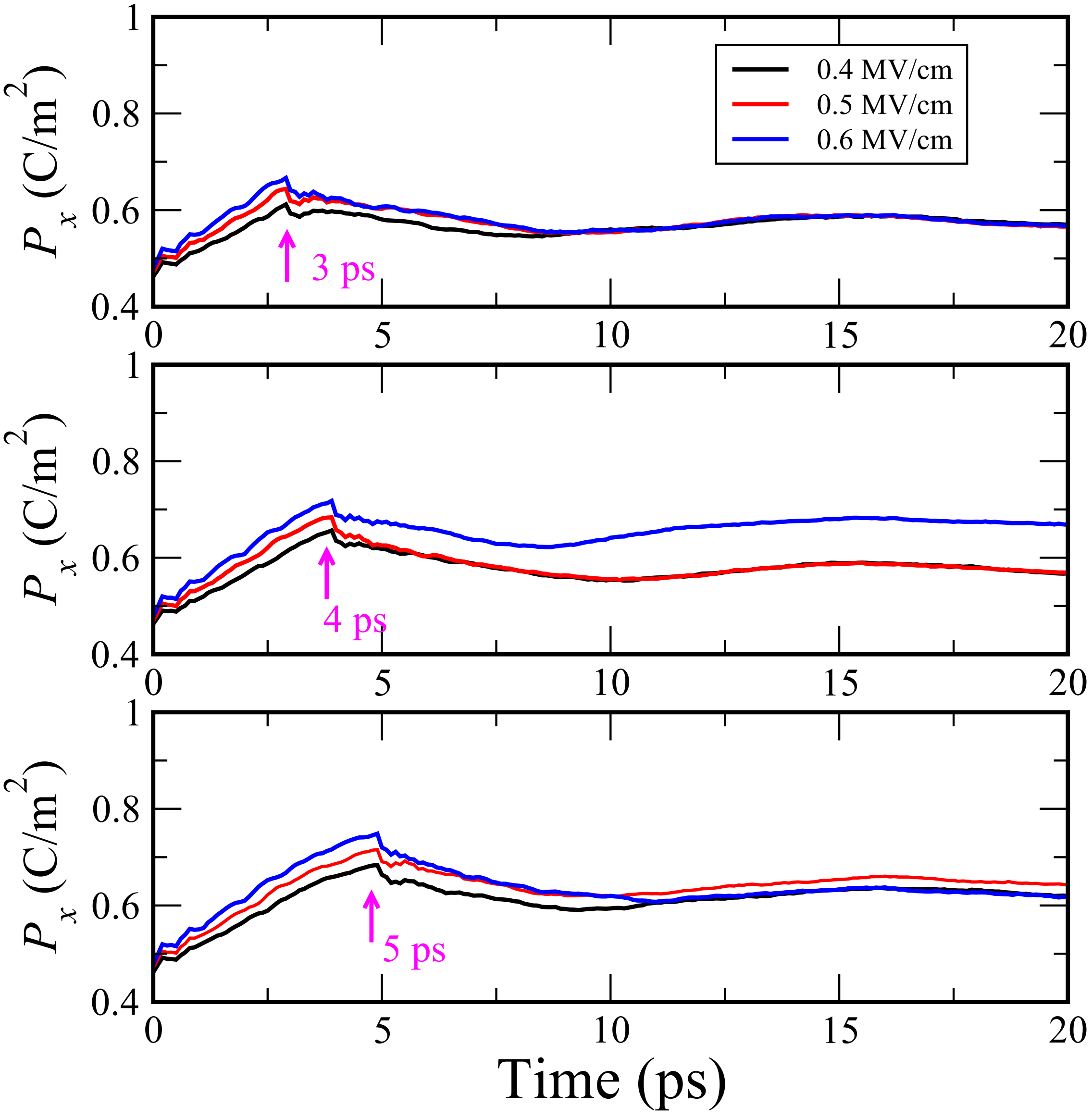

Figure 6.7: The evolution of x-component polarization of 90° DW in response of electric pulse. The electric field is turned off at 3 ps, 4 ps, and 5 ps, respectively.

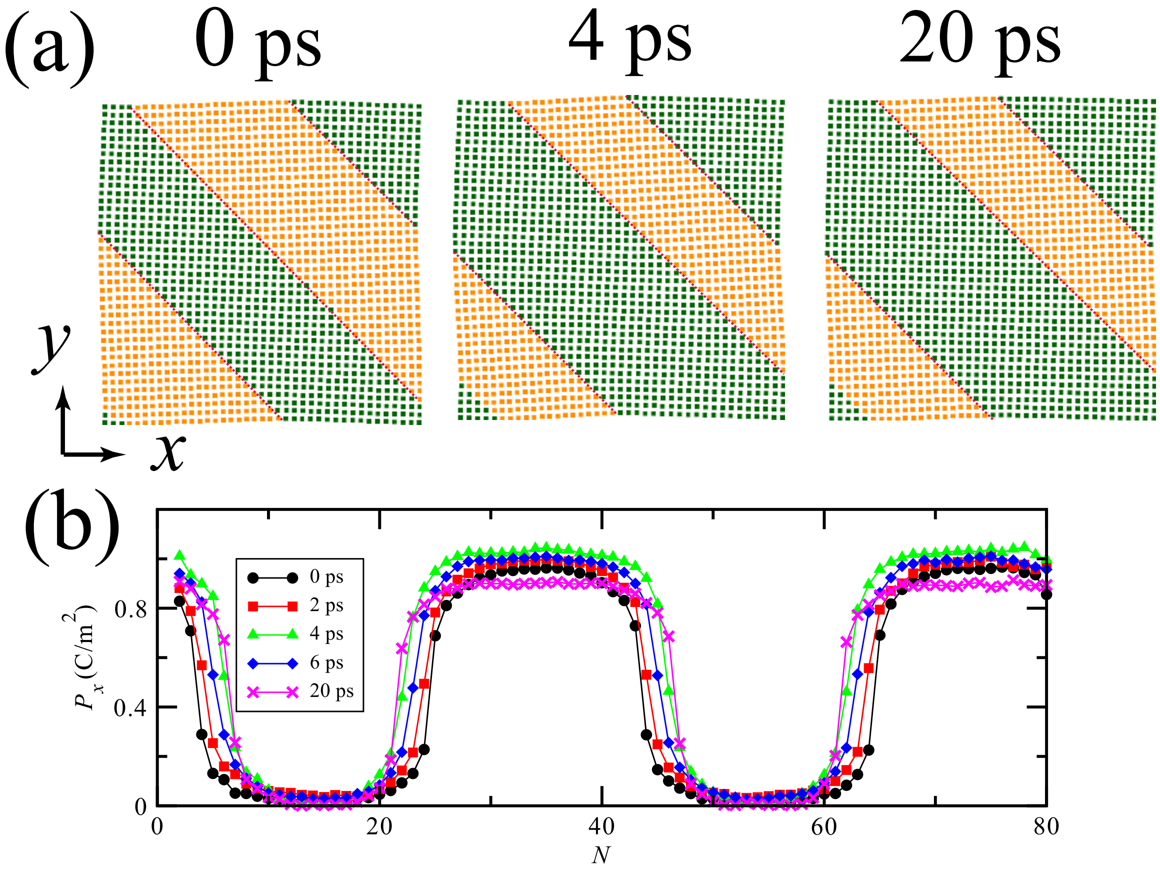

Figure 6.8: Evolution of (a) the domain patterns and (b) polarization profiles of a 90° DW experiencing 4 ps 0.4 MV/cm electric pulse.

6.4 Conclusion

In summary, we have explored the motions of both 180° and 90° domain walls in $PbTiO_3$, subjecting multi-domain samples to electric field pulses via molecular dynamics simulations. The analysis of changes of polarization and evolution of domain patterns reveal that both types of domain walls stop moving when the electric field is turned off and show that the velocity is solely determined by the strength of the electric field at any given time. We therefore conclude that ferroelectric domain walls do not exhibit significant intrinsic inertial response. Inertial movement found in previous simulations is therefore likely to be driven by extrinsic effects (e.g., stress).

Chapter 7

Universal intrinsic mechanism for ferroelectric switching

7.1 Introduction

Domain walls in ferroelectrics are homointerfaces separating regions of different polarity [183]. The existence of domain walls in ferroelectric materials can have a profound influence on the dielectric [184–187], piezoelectric [188, 189], pyroelectric [190, 191], and electronic properties [5, 192, 193] of ferroelectrics. In particular, domain wall motion is crucial for the polarization switching as characterized by the hysteresis loop that is the signature feature of ferroelectric materials [47]. Despite intense studies of domain walls, achieving controlled material design and device optimization for ferroelectrics remains a significant challenge. Experimentally, the observed dynamics of switching and domain walls are usually explained as the behavior of an elastic interface pinned by a random potential generated by defects[92], which appear to be strongly sample-dependent and affected by a wide variety of elastic, microstructural and other extrinsic effects [33–46]. Theoretically, it has been difficult to connect 0 K first-principles-based microscopic quantities (e.g., domain wall energy) to finite-temperature macroscopic properties such as the coercive field that are critical for material design and device performance [84, 85]. This has prevented the use of computational high-throughput methods and genetic algorithms that have been successfully applied to the *ab initio* based design of other types of materials (e.g. heterogeneous catalysts, electrochemical battery materials, and semiconducting oxides). Using the 90° domain walls in $PbTiO_3$ as an example, we explore the intrinsic ferroelectric response of domain walls with molecular dynamics (MD) simulations [159] under a wide range of temperatures and electric fields. With the microscopic insights obtained from MD simulations, we then propose a simple universal nucleation-and-growth-based analytical model that is able to quantify the dynamics of all types of domain walls in various ferroelectrics and use it to predict the temperature- and frequency-dependence of hysteresis loops and coercive fields at finite temperature from first-principles. Comparison of the theoretical and experimental results shows that even in the absence of defects the intrinsic temperature- and field-dependence of the wall velocity can be described with a non-linear creep-like region and a power-law depinning-like region. The estimated theoretical dynamical exponent μ and the velocity exponent θ agree well with the experimental values [39], highlighting the intrinsic origin for the domain wall motion in real materials. Similarly, the coercive fields estimated from our model agree well with experimental results for ceramics and thin films. This work suggest that despite the complexity of ferroelectric materials, the switching in ferroelectrics is largely governed by a simple universal mechanism of intrinsic domain wall motion; this provides an efficient framework for predicting and optimizing material properties of ferroelectrics.

In ferroelectric materials, domain walls separate regions with different polarization orientations. In response to an external perturbation that favors one polarization state over another, the domain wall will move to increase the size of the domain favored by the perturbation, eventually leading to polarization switching of the whole material. The translational motion of the 180° domain wall has been studied both experimentally [33, 34, 39, 40] and theoretically [25, 35, 79, 163, 194, 195]. The dynamical behavior of a domain wall is usually understood as an elastic interface moving in a fluctuating pinning potential created by defects[92]. Under relatively weak electric fields (E), the propagation of domain walls at finite temperature (T) can be described with a creep process [39, 40],

$$v \propto \exp\left[-\frac{U}{k_B T}\left(\frac{E_{C0}}{E}\right)^{\mu}\right] \tag{7.1}$$

where U is a characteristic energy barrier, k_B is Boltzmann's constant, E_{C0} is a critical field at which depinning occurs at 0 K and μ is called dynamical exponent determined by the nature of defects. The dynamical exponent $\mu = 1$ is usually ascribed to the random field defects which break the symmetry of the ferroelectric double-well potential [39, 40], while

$\mu = 0.5$ is an indication of random bond disorder which locally modify the symmetric ferroelectric double-well potential depth [36, 41, 42]. Another widely used equation that characterizes switching and domain wall motion takes the form of $v = v_0 \exp(-E_a/E)$, where E_a is the temperature-dependent activation field (Merz's law) [33–35]. Merz's law can be viewed as a reformulation of equation (7.1) with $\mu = 1$ and $E_a = UE_{C0}/k_BT$. When the electric field becomes larger than the crossing field E_{C0}, the wall experiences a pinning-depinning transition [39] with the velocity becoming temperature-independent and given by

$$v \propto (E - E_{C0})^{\theta} \tag{7.2}$$

where θ is a velocity exponent that reflects the dimensionality (D) of the wall. A classical theory based on a nucleation-and-growth mechanism was developed by Miller and Weinreich [35] to explain the intrinsic origin of Merz's law and creep behavior. However, the Miller-Weinreich model assumes an atomically-sharp triangular critical nucleus which incorrectly leads to implausibly high activation field for nucleation [40, 42]. Multiscale simulations for 180° domain walls in defect-free $PbTiO_3$ revealed a square critical nucleus with diffusive and beveled interface that significantly reduces the nucleation barrier and hence leads to much lower activation fields for domain wall motion, suggesting an intrinsic origin for $\mu = 1$ [25].

Unlike the motion of 180° domain walls, switching processes in ceramic, thin film and single crystal ferroelectrics are much less understood. The presence of a variety of extrinsic features, the possible role of ferroelastic non-180° switching and the long mus-ms time scales typically studied for switching make it challenging to relate the observed hysteresis loops to the microscopic properties of ferroelectric materials. Because of the strong clamping effect of the substrate [32, 196], the intrinsic dynamics of non-180° domain walls cannot be studied in high-quality ferroelectric thin films; instead, most recent experimental and theoretical studies of the non-180° domain walls have focused on the static properties [186, 187, 197]. Here, we use a multiscale approach to computationally model the switching process. We first obtain the missing quantitative understanding of the intrinsic dynamics of non-180° domain walls and encapsulate it in a simple and general model for domain wall speed. The model is then used in coarse grained simulations on long time scale that enable accurate calculation of ferroelectric switching hysteresis loops and coercive fields.

7.2 Results and discussion

7.2.1 Intrinsic creep-depinning transition

We quantitatively estimate the velocity of 90° domain wall in defect-free $PbTiO_3$ over a wide range of temperatures and electric fields using large-scale MD simulations (see Methods). Figure 7.1 presents the velocity as a function of applied electric field for various temperatures, revealing an intrinsic "creep-depinning" transition. In the low-field region ($E <$ 0.5 MV/cm), the velocity depends on the temperature significantly and has a strong non-linear dependence on the electric field. In the high-field region ($E >$ 0.5 MV/cm), the temperature dependence of the domain wall velocity becomes weaker, as seen in the overlap of the velocity data obtained at different temperatures. For example, the velocity data obtained at 20 K are nearly indistinguishable from those at 40 K. Plotting $\ln v$ vs $1/E$ (Fig.2b), we find that $\ln v$ has a linear relationship with $1/E$ in the low-field region. This confirms that for relatively low electric fields and high temperatures the velocity of the 90° domain wall follows Merz's law, or equivalently, shows $\mu = 1.0$ and a creep-like response even in the absence of defects. The slope of the line in the $\ln v$ versus $1/E$ plot gives the activation field E_a (UE_{C0}/k_BT). The inset in Fig 7.1b shows the temperature dependence of E_a above 140 K. The nearly linear relationship between E_a and $1/T$ shows that UE_{C0}/k_B is temperature independent in the creep-like region with a value of 283 K MV/cm. Fitting the velocity data at 40 K with equation 7.2, we find that $\theta = 0.72$ and $E_{C0} = 0.48$ MV/cm. The crossing field for the 90° domain wall is lower than that for the 180° domain wall (1 MV/cm) in Pb(Zr, Ti)O_3 (PZT) thin films [38]; this is expected because *ab initio* calculations have shown that the 90° domain wall in PbTiO_3 has lower energy than the 180° domain wall in PZT [79, 85]. The values of the dynamical exponents are the same ($\mu = 1$) for both 90° domain wall and 180° domain wall [25]. This indicates a universal intrinsic response for ferroelectric domain walls under a relatively low driving force. The observed intrinsic "creep-depinning" transition can be explained with an intrinsic nucleation-and-growth mechanism. The nucleation barrier and the size of critical nucleus decrease for stronger applied electric fields. At low fields, the large size of the critical nucleus and the high nucleation barrier relative to thermal fluctuation make nucleation the rate limiting step and lead to an Arrhenius-dependence of the velocity observed in the creep region. At high fields, the nucleation barrier is small and the domain wall velocity is growth dominated, resulting in near-linear dependence on electric fields and weak temperature dependence.

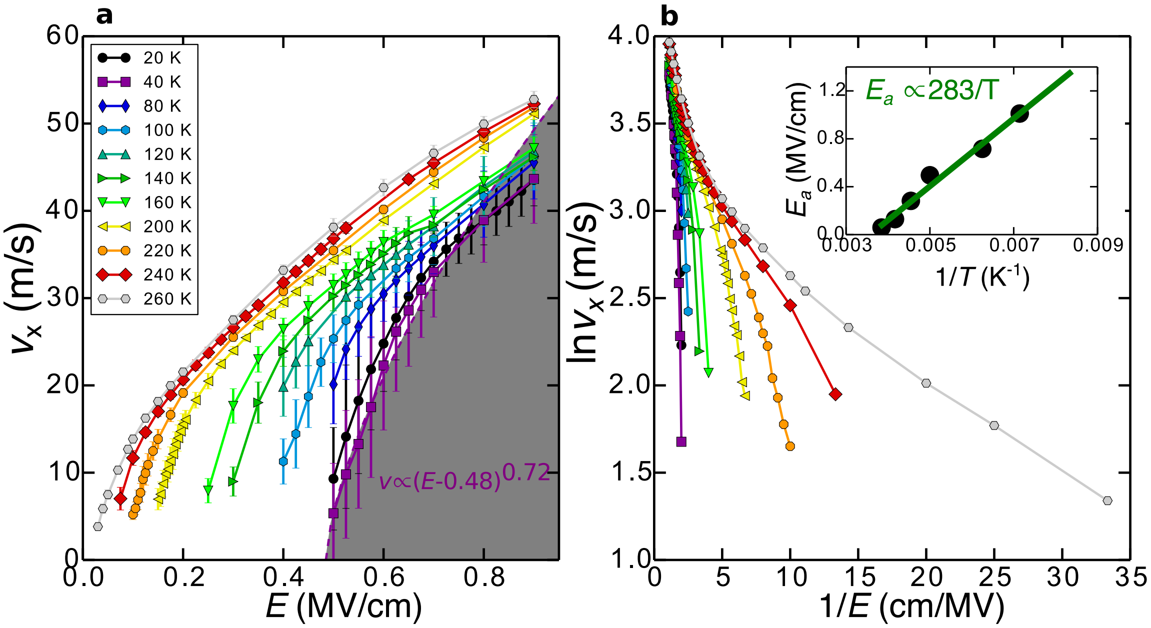

Figure 7.1: Domain wall velocity from molecular dynamics simulations. **a**, Temperature and field dependent domain wall velocity (v) data reveal an intrinsic "creep-depinning" transition. The wall velocity data at 40 K are in the flow region and are fit to equation 2. We find $\theta = 0.72$, $E_{C0} = 0.482$ MV/cm (boundary of the shadow area). The solid lines are guidelines for eyes. **b**, $\ln v$ vs $1/E$ curves. The inset shows the temperature dependence of the activation field E_a (UE_{C0}/k_BT) in the creep-like region.

7.2.2 LGD nucleation-and-growth model

We now develop an analytical model for nucleation at a non-180° domain wall based on our results of 90° domain wall from MD simulations. As shown in Fig. 7.2a 90° domain wall in x-y coordinates can be viewed as a special 180° domain wall in X-Y coordinates: the polarization component parallel to the domain wall (P_Y) is reversed by 180° across the boundary, while the polarization component perpendicular to the domain wall (P_X) remains almost unchanged. This is confirmed by the polarization profile obtained from the MD simulations (bottom of Fig. 7.2a). This transformation allows us to treat all types of non-180° domain walls as a 180° domain wall. Detailed examinations of nucleation events at the domain wall ($X = 0$) at low temperature (T = 20 K) reveal a diamond-like nucleus in the Y-Z plane (Fig. 7.2b), with significant diffuseness at the boundary characterized by a gradual polarization change. With this microscopic picture of nuecleaiton, we use Landau-Ginzburg-Devonshire (LGD) theory to relate the nucleation energy to the fundamental characteristics of the material. The nucleation energy U_{nuc} can be expressed as:

$$U_{\text{nuc}} = \Delta U_E + \Delta U_i \tag{7.3}$$

where

$$\Delta U_E = -E \int_{-\infty}^{\infty} dX \int_{-\infty}^{\infty} dY \int_{-\infty}^{\infty} dZ \left(P_{\text{nuc}}(X,Y,Z) - P_{\text{DW}}(X,Y,Z)\right) \tag{7.4}$$

$$\begin{aligned}\Delta U_i = \int_{-\infty}^{\infty} dX \int_{-\infty}^{\infty} dY \int_{-\infty}^{\infty} dZ\, \{[U_g(P_{\text{nuc}}) + U_{\text{loc}}(P_{\text{nuc}})] - \\ [U_g(P_{\text{DW}}) + U_{\text{loc}}(P_{\text{DW}})]\}\end{aligned} \tag{7.5}$$

Here $P_{\mathrm{nuc}}(X, Y, Z)$ and $P_{\mathrm{DW}}(X, Y, Z)$ are the polarization profiles of a domain wall with and without the nucleus, respectively. U_{loc} is the local energy penalty due to the deviation of the local polarization from the ground state bulk value (P_s) and is given by $U_{\mathrm{loc}}(P) = A_{\mathrm{loc}}\left[1 - (P/P_s)^2\right]^2$, where A_{loc} is the energy difference between the ferroelectric phase and the paraelectric phase. U_g is the gradient energy due to the polarization changes ($\partial_j P_i$) at the domain wall and is given by $U_g(P_i) = \sum_j g_{ij}\left(\partial_j P_i\right)^2$, where g_{ij} is the coefficient for the gradient of the i-th component of P along direction j. The value of g_{ij} can be derived from the energy and diffusiveness of the domain wall (see Methods). The contributions from stress (σ^2) and stress-polarization coupling (σP^2) terms can easily be implemented into equation 3. However, we find that the change of elastic energy (see Supplementary Information) is not significant and is therefore omitted in following analysis. At the lowest approximation, the P_X and P_Z remain unchanged across the domain wall, and therefore, the nucleation energy only depends on P_Y. The profile of P_Y for a domain wall containing a nucleus of size $l_1 \times l_2 \times l_3$ can be described as:

$$P_Y = \frac{2P_s}{\sqrt{2}} f\left(X, l_1, \delta_1\right) f\left(Y + Z, \sqrt{2} l_2, \delta_2\right) f\left(Y - Z, \sqrt{2} l_3, \delta_3\right) + \frac{P_s}{\sqrt{2}} g\left(X, l_1, \delta_1\right) \tag{7.6}$$

where $f(t, l, \delta) = \frac{1}{2}\left[\tanh(\frac{t+l/2}{\delta/2}) - \tanh(\frac{t-l/2}{\delta/2})\right]$, $g(t, l, \delta) = \tanh\left(\frac{t-l/2}{\delta/2}\right)$ and δ_i characterizes the diffuseness of the nucleus along direction i. Fig. 7.2c shows the polarization profile in Y-Z and X-Y planes generated by equation 7.6. Numerically integrating equation 3 allows the identification of the critical nucleus and the estimation of the nucleation activation energy (ΔU_{nuc}). According to Avrami theory of transformation kinetics, ΔU_{nuc} can be related to the activation field in Merz's law as $E_a \approx \frac{1}{d+1}\frac{\Delta U_{\mathrm{nuc}}}{k_B T} E$, where d is the dimensionality [25]. Applying this relation with $d = 2$ and using parameters (A_{loc} and g_{ij}) obtained from our classical BV potential, we obtain E_a values for a range of temperatures.

As shown in Fig. 7.2d, the activation fields predicted from the analytical model agree well with MD results. To apply the model to the other types of non-180° domain walls, only a simple modification of the input parameters is required with the necessary values easily obtained from first-principles density functional theory (DFT) calculations of the particular domain wall (see Methods).

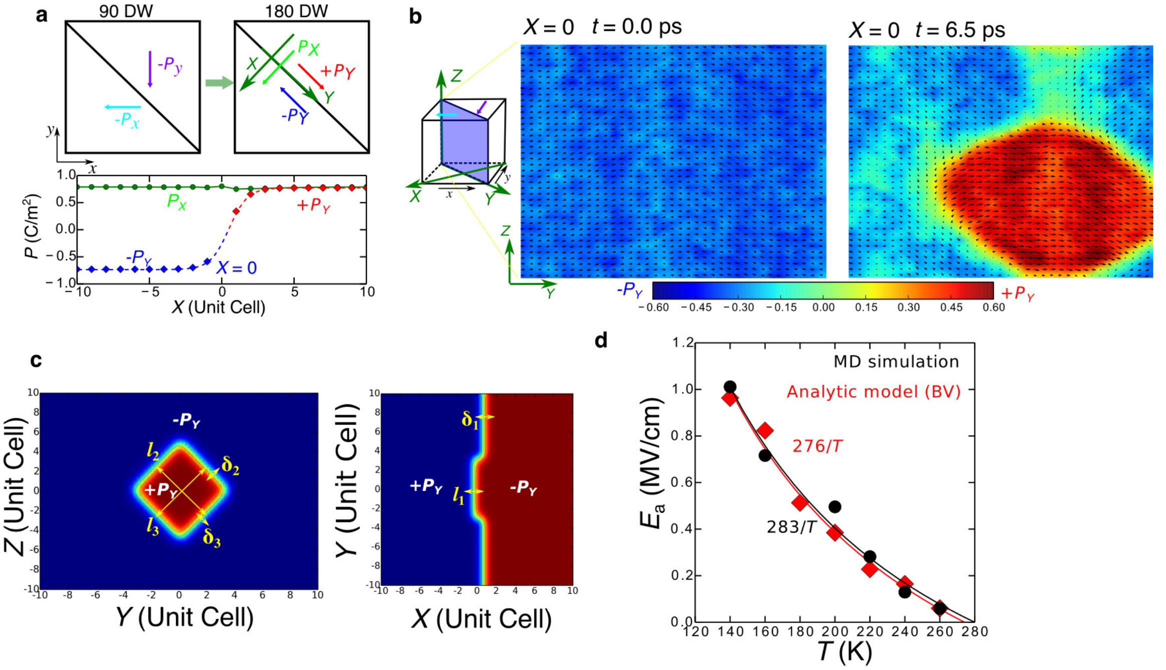

Figure 7.2: Landau-Ginzburg-Devonshire model of nucleation at domain walls. **a**, Schematic of mapping a 90° domain wall in x-y coordinates to a 180° domain wall in X-Y coordinates. The bottom figure shows the polarization profile of a 90° domain wall in X-Y coordinates. The change of P_X across the domain wall is small. **b**, Simulated nucleation process at the domain wall in the Y-Z plane. The black arrows scale with the local dipole magnitudes of each unit cell in Y-Z plane. The background of each arrow is colored based on the magnitude of Y-component of the local dipole. **c**, Polarization profile of a nucleus generated by equation 6. **d**, Comparison of the activation fields obtained from MD simulations with the results of the Landau-Ginzburg-Devonshire model. The analytical model reproduces MD activation fields using BV-potential-based parameters together with the MD temperature dependence of local polarization.

7.2.3 Simulating hysteresis loops and coercive fields

The availability of an analytical model that uses DFT inputs enables a rapid estimation of activation fields without the much more time-consuming MD simulations, which further enables us to make the connection between the microscopic characteristics calculated by DFT and the hysteresis loops and coercive fields (E_c) measured experimentally for a variety of macroscopic material samples. The coercive field reflects the ease of domain reversal and is one of the most important characteristic parameters of ferroelectrics for practical applications. For the domain reversal process achieved via domain wall motion, the change of the polarization under an applied electric field directly correlates with the distance moved by the domain wall, the velocity of which can be estimated based on Merz's law (see Methods). We extract the pre-exponential factor v_0 in Merz's law from MD simulations in the creep-like region and obtain E_a values for $\mathrm{PbTiO_3}$ from the LGD model with parameters calculated with DFT PBEsol calculations [139]. With these values of v_0 and E_a, we then simulate hysteresis loops at 300 K and obtain the frequency dependence of E_c for varying domain sizes (Fig. 7.3a). Since the structure and polarization of PZT are similar to those of $\mathrm{PbTiO_3}$, we compare the simulated values of the $\mathrm{PbTiO_3}$ E_c to various experimental values for PZT materials. It is found that our theoretical coercive fields (Fig. 7.3b) using parameters of 90° domain wall motion agree well over a large frequency range with experimental E_c values (5-20 kV/cm) [88–91]. The E_c values based on 180° domain wall motion are quite large and exhibit the correct frequency dependence, in agreement with experimental results obtained in thin films [198]. This suggests that the 180° switching in ceramics proceeds via sequential 90° domain wall motion [88], due to the much smaller intrinsic nucleation barrier at the 90° domain wall. Thus, the switching and coercive fields in PZT are largely determined by the intrinsic properties of the appropriate domain wall motion mechanism. Similar to the PZT results, we find that switching in $\mathrm{BaTiO_3}$ ceramics is governed by the motion of 90° domain walls, with the predicted coercive field of around

0.1 kV/cm at 300 K close to the experimental value for coarse $BaTiO_3$ ceramics [199–201].

Polarization reversal in $BiFeO_3$ is another good test of our model due to the importance of octahedral rotations and the presence of three types of domain walls in the rhombohedrally polarized $BiFeO_3$. Previous DFT calculations revealed that the 71° domain wall has the highest energy, followed by 180° domain wall, with the lowest domain wall energy for the 109° domain wall[170, 202, 203]. The higher energy of 71° domain wall is attributed to the mismatch of oxygen octahedra rotation across the domain boundary. We introduce a second order parameter, oxygen octahedra rotation (θ), into our LGD-based nucleation-and-growth model (see Methods). Using DFT domain wall energies, our analytical model predicts the opposite order for the coercive field: E_c is lowest for the 71° wall, followed by the 109° and 180° domain wall. The predicted coercive fields for 180° walls are comparable with the experimental values in thin films[144, 204]. The ability of our simple analytical model to estimate the E_c values accurately indicates that the value of the coercive field is largely determined by the intrinsic properties of the material, with the nucleation barrier on the domain wall controlling the dynamics of polarization reversal.

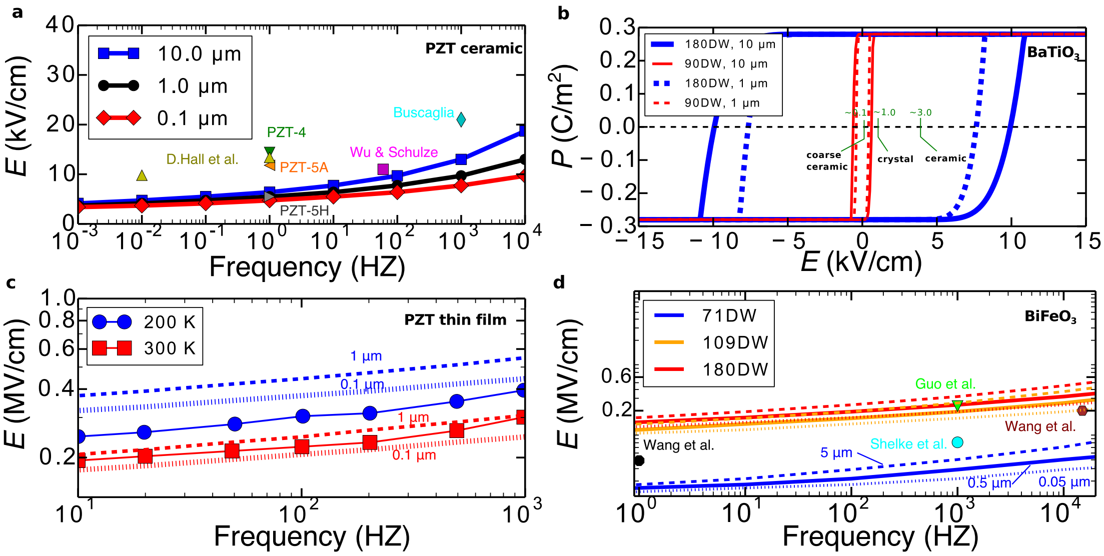

Figure 7.3: Hysteresis loops and coercive fields for several materials simulated using first-principles data. **a**, Simulated frequency dependence of coercive fields for various domain sizes at 300 K. Theoretical values are comparable to various experimental values in ceramics. **b**, Hysteresis loops of $BaTiO_3$ with a domain size of 10 μm (coarse grain). **c**, Frequency and temperature dependent coercive fields for PZT thin films. Experimental data are taken from Ref. 47. A domain size of 500 nm is used to obtain the theoretical values. **d**, Coercive fields for different domain walls in $BiFeO_3$ with a domain size of 500 nm.

7.3 Conclusions

In summary, we have demonstrated that the motion of ferroelectric domain walls exhibits an intrinsic creep-depinning transition resulting from the nucleation-and-growth mechanism at the domain wall and is governed by a universal nucleation mechanism. Comparison of coercive fields obtained from hysteresis loops due to the intrinsic mechanism shows that switching in FE films and ceramics is largely controlled by intrinsic characteristics of the materials. Such a unified framework relates microscopic zero-Kelvin quantities to macroscopic material parameters at finite temperature, and thus suggests an appealing avenue for rational material design.

7.4 Methods

7.4.1 Molecular dynamics simulations of 90° domain wall

To understand the intrinsic dynamics of non-180° domain walls, we study the motion of the 90° domain wall in defect-free $\mathrm{PbTiO_3}$ as an example and then generalize the obtained results to other types of non-180° domain walls. We perform molecular dynamics simulations over a wide range of temperatures and electric fields using a bond-valence-based classical potential (BV) and extract the velocity data for the 90° domain wall [159, 163]. As shown in Fig. 7.4, we use a $40 \times 40 \times 40$ supercell with polarization direction changing from $[0\bar{1}0]$ to $[\bar{1}00]$ across the boundary. Due to the usage of an orthorhombic supercell, the domains are homogeneously strained, making the relative angle between the orientations of the polarization axes of neighboring domains exactly 90° rather than $2\arctan(a/c)$ that is geometrically required for a tetragonal ferroelectric. The electric field is applied along $[100]$ direction; this will cause the domain wall to move along the [110] direction

(v_{DW}) due to the 90° switching of $[\bar{1}00]$ dipoles to $[0\bar{1}0]$ dipoles at the domain boundary (Fig. 7.4b). The velocity of the domain wall motion can be calculated from the slope of the time evolution profile of the supercell dimension along [100] direction (L_x) and is given by $v_{\mathrm{DW}} = v_x\sqrt{a^2 + c^2}/(c - a)$, where $v_x = dL_x/dt$, c is the long-axis lattice constant and a is the short-axis lattice constant. Owing to the stochastic behavior of nucleation, 20 simulations with slightly different initial structures are carried out for a given temperature and electric field to obtain the velocity average and standard deviation.

7.4.2 Model parameters for non-180° domain walls

The nucleation model discussed here closely follows the methods in Ref. 25. The mapping scheme discussed in the paper allows the treatment of a non-180° domain wall as a generalized 180° domain wall lying in the Y-Z plane with polarization changing from $+P_Y$ to $-P_Y$ along X. The following five parameters are required to estimate the nucleation energy at the domain wall under a given temperature T: $P_s(T)$, $A_{\mathrm{loc}}(T)$, g_{YY}, g_{YX} and g_{YZ}, where

$$P_Y(T) = \gamma P_s(T) \tag{7.7}$$

$$A_{\mathrm{loc}}(T) = A_{\mathrm{loc}}(0)\frac{P_s^4(T)}{P_s^4(0)} \tag{7.8}$$

$$A_{\mathrm{loc}}^{Y}(0) = \gamma^4 A_{\mathrm{loc}}(0) \tag{7.9}$$

$$g_{YX} \approx g_{YZ} = \left[\frac{3\sigma_{\mathrm{DW}}^{YX}}{8P_Y(0)}\right]^2 \frac{1}{A_{\mathrm{loc}}^{Y}(0)} = A_{\mathrm{loc}}^{Y}(0)\left[\frac{\delta_X}{2P_Y(0)}\right]^2 \tag{7.10}$$

$$g_{YY} = \left[\frac{3\sigma_{\mathrm{DW}}^{YY}}{8P_Y(0)}\right]^2 \frac{1}{A_{\mathrm{loc}}^{Y}(0)} = A_{\mathrm{loc}}^{Y}(0)\left[\frac{\delta_Y}{2P_Y(0)}\right]^2 \tag{7.11}$$

Here P_s is the total local polarization, γ is the percentage of the polarization variation across the domain boundary (e.g., $\gamma = \sqrt{2}/2$ for a 90° domain wall), A_{loc} is the energy difference between the ferroelectric phase and the high symmetry paraelectric phase; $\sigma_{\mathrm{DW}}^{YX}$ is the energy of a domain wall with normal along X and neighboring dipoles along X, and δ_X is the diffusiveness parameter across the domain boundary; In analogy, $\sigma_{\mathrm{DW}}^{YY}$ is the energy of a domain wall with normal along Y and neighboring dipoles also along Y (head-to-head or tail-to-tail domain wall), and δ_Y is associated diffusiveness parameter. $P_s(0)$ and $A_{\mathrm{loc}}(0)$ are easily assessable to zero-Kelvin DFT calculations. The temperature dependence of $P_s(T)$ is taken from experiments when available. The values of $g_{_{YY}}$ and g_{YZ} can be determined based on the domain wall energy (σ_{DW}, calculated from DFT) or diffusiveness parameters (δ, calculated from MD). In practice, $g_{_{YY}}$ and $g_{_{YX}}(g_{YZ})$ are of the same order, and therefore $g_{_{YX}} \approx g_{_{YY}}$ is a useful approximation.

For BaTiO$_3$, DFT calculations using PBEsol with $a = 3.986$ Å and $c/a = 1.1$ give $A_{\mathrm{loc}}(0)$ = 3.48×10^7 J/m^3, $\sigma_{180\mathrm{DW}} = 11$ mJ/m^2, $\sigma_{90\mathrm{DW}} = 3.89$ mJ/m^2, $P_s(0) = 0.283$ C/m^2 and $g_{_{YX}} = 0.61 \times 10^{-11}$ m^{3}F^{-1}. These parameters are used for simulating the hysteresis loop in Fig. 7.3a. For PbTiO$_3$, we used experimental lattice constants ($a = 3.9$ Å, $c = 4.15$ Å) for DFT calculations with PBEsol and obtain $A_{\mathrm{loc}}(0) = 5.05 \times 10^8$ J/m^3, $\sigma_{180\mathrm{DW}} = 175$ mJ/m^2, $\sigma_{90\mathrm{DW}} = 67$ mJ/m^2, $g_{_{YX}} = 1.21 \times 10^{-11}$ m^{3}F^{-1}. The temperature dependence of polarization is taken from Ref with $P_s(0) = 0.872$C/m^2. These parameters are used for predicting the coercive fields of PbTiO$_3$-based ceramics and thin films in Fig. 7.3(b,c).

7.4.3 LGD model for BiFeO$_3$

71°, 109° and 180° domain walls are possible in BiFeO$_3$. The energetics of these three types of domain walls have been investigated with DFT in several studies[170, 203]. Diéguez *et al.* [170] reported $\sigma_{71\mathrm{DW}}$ = 152 mJ/m^2, $\sigma_{109\mathrm{DW}}$ = 62 mJ/m^2, and $\sigma_{180\mathrm{DW}}$ = 73 mJ/m^2 using LDA. Wang *et al.* [203] reported $\sigma_{71\mathrm{DW}}$ = 128 mJ/m^2, $\sigma_{109\mathrm{DW}}$ = 33 mJ/m^2, and $\sigma_{180\mathrm{DW}}$ = 98 mJ/m^2 with GGA+U. From equation 10, it is easy to deduct that $\sigma_{\mathrm{DW}}^{YX} \propto P_Y\sqrt{A_{\mathrm{loc}}^{Y} g_{_{YX}}}$. Assuming the polarization gradient coefficient is isotropic, a non-180° domain wall energy

($\sigma^{\gamma}_{\text{DW}}$) can be related to the 180° domain wall energy with $\sigma^{\gamma}_{\text{DW}} = \gamma^3 \sigma_{180\text{DW}}$. Therefore, for a given ferroelectric, $\sigma_{71\text{DW}} : \sigma_{90\text{DW}} : \sigma_{109\text{DW}} : \sigma_{180\text{DW}} = 0.192 : 0.354 : 0.544 : 1$. Such relationship appears to work well for 90° and 180° domain walls in BaTiO_3 and PbTiO_3 [79], and reasonably well for 109° and 180° domain walls in BiFeO_3 [170, 203]. However, the 71° domain wall is found to have the highest energy in BiFeO_3, which is attributed to the mismatch of oxygen octahedra rotation across the domain boundary [170, 203]. To capture this feature, we introduce a second order parameter, oxygen octahedra rotation (θ), into the LDG model of BiFeO_3. Therefore, the 71° domain wall in BiFeO_3 has following extra energy term

$$U_\theta = \frac{1}{2}K \int_{-\infty}^{\infty} dX \int_{-\infty}^{\infty} dY \int_{-\infty}^{\infty} dZ \left(\theta_{\text{DW}}(X,Y,Z) - \theta_{\text{Bulk}}(X,Y,Z)\right) \tag{7.12}$$

where K is the harmonic angle constant and $\theta_{\text{Bulk}}(X,Y,Z) \approx 8^\circ$ [203]. The value of K is optimized such that the LGD model reproduces the DFT value of $\sigma_{71\text{DW}}$. Following term is added to equation 3 when estimating the nucleation energy,

$$\Delta U_\theta = \frac{1}{2}K \int_{-\infty}^{\infty} dX \int_{-\infty}^{\infty} dY \int_{-\infty}^{\infty} dZ \left(\theta_{\text{nuc}}(X,Y,Z) - \theta_{\text{DW}}(X,Y,Z)\right) \tag{7.13}$$

where an analytical equation similar to equation 6 to describe the angle profile $\theta_{\text{nuc}}(X,Y,Z)$. Other parameters are $A_{\text{loc}}(0)$ = 5.81×10^8 J/m^3, $P_s(0)$ = 0.987 C/m^2, T_0 = 1120 K.

7.4.4 Analytical simulation of P-E hysteresis loop

Following the experimental setup in most hysteresis loop measurements, a triangular electric field, $E(t)$, with frequency f and maximum magnitude E_0 is used in the simulation:

$$E(t) = \begin{cases} 4fE_0t & 0 < t < \frac{1}{4f} \\ -4fE_0t + 2E_0 & \frac{1}{4f} < t < \frac{3}{4f} \\ 4fE_0t - 4E_0 & \frac{3}{4f} < t < \frac{1}{f} \end{cases} \tag{7.14}$$

At $t = 0$, the domain of size d is fully poled with saturation polarization $-P_s$. Assuming the domain reversal is achieved via domain wall motions, the polarization at t can be calculated with

$$P(t) = -P_s + \frac{\int_0^{1/f} v(t)dt}{d} P_s, \tag{7.15}$$

where $v(t)$ is the domain wall velocity at time t and is calculated using Merz's law, $v(t) = v_0 \exp(-E_a/E(t))$. When the value of $P(t)$ obtained from equation 7.15 is larger than P_s (the domain is fully reversed), $P(t)$ is set to P_s. Plotting $E(t)$ with respect to $P(t)$ leads to the hysteresis loop. The coercive field E_c is the magnitude of the electric field when $P(t) = 0$. We used $v_0 = 300$ m/s for predicting room-temperature coercive fields based on results from MD simulations. We find that the coercive field is not sensitive to the value of v_0, as demonstrated by the moderate change of coercive fields in response to orders of magnitude change in d (which is equivalent to changing v_0 for fixed d).

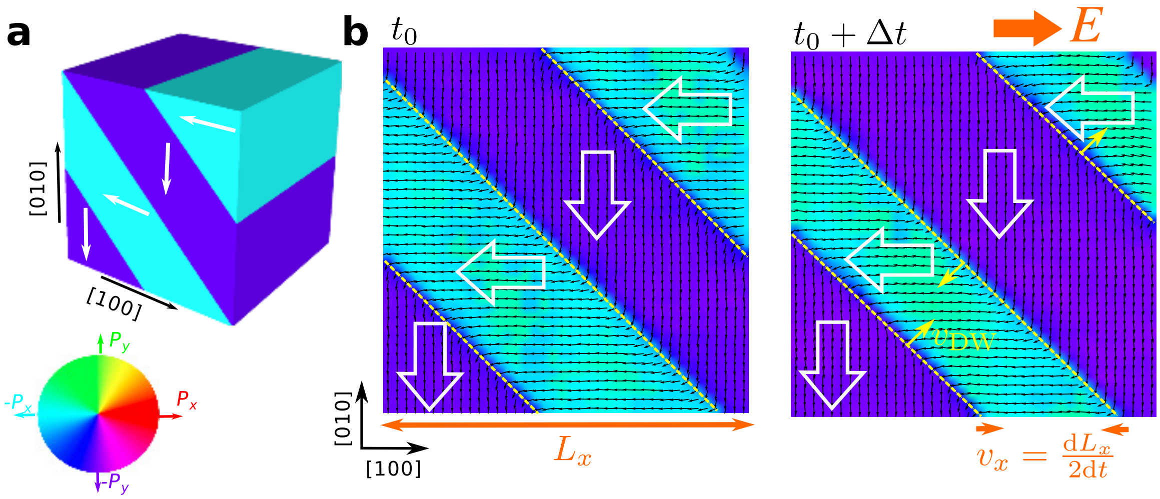

Figure 7.4: Large-scale molecular dynamics simulations of 90° domain wall motions. **a**, Schematic diagram of a $40 \times 40 \times 40$ supercell with 90° domain walls used in molecular dynamics simulations. The colors of the domains correspond to the polarization wheel shown at the bottom. **b**, Simulated domain evolution under [100]-oriented electric field. The electric field is turned on at t_0. The wall velocity v along [110] is estimated based on the change of supercell dimension L_x along [100] from t_0 to $t_0 + \Delta t$. The black arrow scales with the local dipole of each unit cell. The domain wall motion is achieved via the 90° switching of $[\bar{1}00]$ dipoles to $[0\bar{1}0]$ dipoles.

Chapter 8

Ferroelectric polarization reversal via successive ferroelastic transitions

8.1 Introduction

Ferroelectric materials are increasingly being considered as critical components in next generation logic [205], non-volatile memories [4], actuators and sensors [6], and electro-optic elements for waveguide devices [7]. Such applications require a deep understanding of the susceptibilities (especially to electric fields) and routes to control and manipulate the order parameters in these materials. Recent advances in thin-film synthesis have enabled the manipulation of structure and properties of ferroelectric thin films [69, 206]. For example, in the tetragonal ferroelectric $PbZr_{0.2}Ti_{0.8}O_3$ both the domain structure [207, 208] and properties (i.e., dielectric [186, 188, 209], piezoelectric [188, 210], and pyroelectric [211, 212]) can be dramatically tuned by varying epitaxial strain, film thickness, electrical boundary conditions, and other parameters. To date, the majority of work on such films has focused on (001)-oriented heterostructures, where the possible domain structures have been theoretically predicted [212, 213] and observed [212, 214]. How these domain structures evolve in other film orientations, however, has not been widely probed. Studies of single-crystal ferroelectrics, however, where it is possible to apply the stimulus field along different crystallographic directions [187, 215, 216], have demonstrated that a poling field that is not purely along the bulk polarization direction produces increased domain wall density and enhanced dielectric [217] and piezoelectric [218] responses. Similar studies on thin-film samples have not been completed.

Breakthrough applications of these materials require knowledge of both the static structure and the dynamics of field-dependent responses. Real-time studies of polarization dynamics including (for example) X-ray scattering, [219–221] piezoresponse force microscopy (PFM) [74, 75], and transmission electron microscopy [222–224] have shed new light on switching processes. Despite these advances, it remains difficult to explore some aspects of switching that take place on very short time scales. Advances in molecular dynamics (MD) simulations now provide an unprecedented look at the dynamics of complex nanoscale events [23], and interatomic potentials derived from *ab initio* calculations can be applied to study finite-temperature properties in a variety of environments [13, 27, 143, 159, 225]. These studies provide insight into the coupling of polarization, strain, electric field, stress, temperature, and local structure; however, there are still very few MD simulations of domain wall motion and growth rates [25], and the dynamics of 90° domain walls has not been investigated previously. In this work, we develop a comprehensive picture of the interrelationships between thin-film epitaxy, nanoscale domain structures, and electric field switching in $PbZr_{0.2}Ti_{0.8}O_3$. Clear differences are demonstrated between (001)-/(101)- and (111)-oriented films with the latter exhibiting complex, nanotwinned ferroelectric domain structures with high densities of 90° domain walls, considerably broadened ferroelectric switching characteristics, and lower threshold fields for the onset of nonlinearity in Rayleigh studies. MD simulations reveal the presence of both 180° switching and multi-step 90° switching domain reversal processes. Subsequent stroboscopic PFM studies confirm the presence of intermediate, 90° switching events in (111)-oriented films and 180° switching events in (001)- and (101)-oriented films. The varying effects of domain sizes (or volume fractions) and electric field on the different film orientations give rise to the difference in switching mechanism. These results have implications for our fundamental understanding of ferroelectric switching and provide avenues to accelerate domain reversal in these materials for next-generation applications.

8.2 Results and discussion

8.2.1 Characterization of differently oriented heterostructures

We focus on 150 nm $PbZr_{0.2}Ti_{0.8}O_3$/10 nm $SrRuO_3$ or $La_{0.7}Sr_{0.3}MnO_3$/$SrTiO_3$(001), (110), and (111) heterostructures grown via pulsed-laser deposition (see Methods section for details). X-ray diffraction studies show that the films are epitaxial and single-phase. The ferroelectric domain structure was probed using PFM. Throughout the remainder of the discussion, we will use the following terminology to describe the polarization variants in the samples: for tetragonal $PbZr_{0.2}Ti_{0.8}O_3$, domains with polarization along the positive and negative [100], [010], and [001] axes will be referred to as $P_1^{+/-}$,$P_2^{+/-}$, and $P_3^{+/-}$, respectively. In (001)-oriented heterostructures, a typical polydomain structure with majority P_3^- domains and minority P_1^+ and P_2^- domains is observed (Fig. 8.1a,b). In (101)-oriented heterostructures, three different domain types are found (Fig. 8.1c,d), with majority P_3^+ domains (in which the polarization is oriented at an angle of $\approx$43.6° from the plane of the film) and the remainder primarily composed of in-plane polarized stripe-like P_2^+ and P_2^- domains and small fractions of P_1^- domains (also oriented $\approx$43.6° from the plane of the film). The as-grown domain structure of the (001)- and (101)-oriented films, as probed by PFM studies which enable exact determination of the polarization directions, represents the equilibrium domain structure predicted for these film orientations [226, 227], and does not change with electric field cycling.

Analysis of the (111)-oriented heterostructures reveals a dramatically different picture. The as-grown domain structure has a complex, metastable nanoscale domain pattern. A domain structure consistent with that predicted to the equilibrium domain structure is obtained after a series of $\pm$6 V d.c. voltages were applied to the PFM tip to switch a 1.5 μm $\times$ 1.5 μm region of the film a total of 2-6 times. The domain pattern consists of a high density of nanotwinned domains (Fig. 8.1e). The observed domain structure is the result of the tiling of three types of domain bands, separated by 120° (noted as areas 1, 2, and 3, Fig. 8.1e) with average domain band widths of ≈300 nm. Within each domain band, the domain structure consists of a mixture of all three degenerate polarization variants (P_1^-,P_2^-,and P_3^-, each possessing a polarization direction that is oriented at an angle of ≈33.9° form the plane of the film) distributed into two sub-bands, with each sub-band composed of only two of the polarization variants. The average domain size within the domain sub-bands is ≈40 nm. The geometry of such domain structures is shown in a schematic illustration (Fig. 8.1f). Prior theoretical treatments predicted such equilibrium domain structures [228].

Having established the difference in domain structures for the various heterostructure orientations, we probed their dielectric and ferroelectric properties using symmetric metal-oxide capacitor structures [229] and MD simulations (see Methods section for details). All heterostructures, regardless of orientation, were found to exhibit symmetric, well-saturated polarization-electric field hysteresis loops (Fig. 8.2a) that are maintained down to at least 1 Hz. As expected, the saturation polarization scales with the film orientation, with (001)- and (111)-oriented films having the largest and smallest values, respectively. In addition, although all films possess high remnant polarization, the (001)- and (101)-oriented films show nearly square hysteresis loops with sharp electric field switching, while (111)-oriented films exhibit more slanted hysteresis loops regardless of frequency, indicative of switching at a broader range of fields.

The dielectric permittivity was then measured as a function of increasing ac electric field excitation. Since we are focused here on switching behavior, we have extended this analysis to larger fields than are typically applied in Rayleigh studies [230]. These studies reveal that (111)-oriented heterostructures exhibit a lower threshold field (8.2 kV/cm) for the onset of non-linearity (or polarization switching) as compared to (001)- and (101)-oriented films (46.3 kV/cm and 22.5 kV/cm, respectively) (Fig. 8.2b). Additionally, the field dependence of the dielectric response of the (111)-oriented film shows a gradual increase (and, therefore, ferroelectric switching) over a much larger range of fields, relative to the (001)- and (101)-oriented films, consistent with the polarization-electric field hysteresis loops (Fig. 8.2a).

8.2.2 Molecular dynamics simulations of domain switching

To understand what gives rise to these different electric field responses, we used MD simulations to examine the evolution of domain switching under differently oriented electric fields. We studied the evolution of domain structures resembling those experimentally observed in (001)-, (101)- and (111)-oriented films possessing 90° domain walls under electric fields applied along the film normal directions $[00\bar{1}]$, $[\bar{1}0\bar{1}]$ (Fig. 8.3a), and $[\bar{1}\bar{1}\bar{1}]$ (Fig. 8.3b), respectively. The volume fraction of the minority domain used in the simulations is based on experimental observations. The MD simulations provide a time-resolved view of the evolution of the domain structure including specific polarization variants.

For brevity, we discuss here only the detailed MD studies of (101)-oriented films, but detailed studies of (001)-oriented films, which show similar results, are also provided. In the case of (101)-oriented films, in the initial state (0.0 ps) we simulate a domain configuration with 20% minority P_2^+domains (green, Fig. 8.3a) and 80% majority P_1^+ domains (red, Fig. 8.3a) with the electric field applied along the $[\bar{1}0\bar{1}]$ (yellow arrow, Fig. 8.3a). This results in a series of complicated changes (Fig. 8.3a). At 3 ps, we observe that the volume fraction of P_2^+ domains increases as they widen via changes of the type $P_1^+ \rightarrow P_2^+$ at the domain boundary due to the $[\bar{1}1]$-component of the electric field. In addition, a significant number of P_1^+ dipoles close to domain boundaries are switched by 180° to P_1^- dipoles (cyan). Further application of electric field facilitates the growth of the P_1^- domains via the 180° switching process of $P_1^+ \rightarrow P_1^-$ (see 5 and 7 ps images, Fig. 8.3a). At 10 ps, the whole supercell reaches a nearly single-domain state. Subsequent relaxation of the structure (after the field is turned off) for another 30 ps results in the reemergence of domain structures similar to that in the initial state (albeit poled in the opposite direction) due to strain accommodation. The lateral shift of the domain boundary is likely due to the application of large electric field to achieve picosecond switching in MD simulations.

In the case of (111)-oriented films, in the initial state (0.0 ps) we simulate a domain configuration with 50% P_1^+domains (red, Fig. 8.3b) and 50% P_2^+ domains (green, Fig. 8.3b) with the electric field applied along the $[\bar{1}\bar{1}\bar{1}]$ (yellow arrow, Fig. 8.3b). This process results in a fundamentally different domain switching evolution (Fig. 8.3b). First, we observe that there is no significant domain wall motion. Although decidedly different from the behavior in (101)-oriented films, this is expected since all polarization directions are energetically equivalent with respect to the applied field. Additionally, at 5 ps, we see new domains perpendicular to their parent domains appear via two types of 90° switching processes: $P_1^+ \to P_2^-$ and $P_2^+ \to P_1^-$, respectively. By 8 ps, the new domains spread quickly across their parent domains and dipole frustration at domain boundaries, leading to transient charged domain walls, is also observed. [231] This switching process continues, until the final configuration of P_1^- and P_2^- domains is achieved by 10 ps. The strain-driven structural relaxation for another 10 ps in the absence of electric field leads to a slight change in the positions of domain walls, but overall the reemergence of domain structures similar to that in the initial state (albeit poled in the opposite direction). What these MD simulations reveal, is that if one only considers the starting and final states, the domain structures could potentially lead one to assume only 180° switching has taken place on the macroscale. These time-dependent models, however, reveal a more nuanced evolution with clear differences between (001)-/(101)- and (111)-oriented films with the latter revealing a multi-step, 90° switching domain reversal process.

8.2.3 PFM switching in differently oriented films

To further explore these proposed switching pathways and their implications for material properties, we completed local-scale PFM switching studies where a time series of images was produced while incrementally increasing the applied tip bias. Focusing first on switching in the (001)- and (101)-oriented films, similarly abrupt switching processes occurring in a narrow field range have been observed, consistent with the macroscale property studies. For brevity, we discuss here only the detailed switching studies of (101)-oriented films (Fig. 8.4), but detailed studies of (001)-oriented films are provided. The (101)-oriented films show no obvious contrast change in either the lateral or vertical PFM images (Fig. 8.4a, b) when applying biases from 0-3.0 V to locally switch a 1 μm $\times$ 1 μm square region in the center of the scanned area. A schematic of this domain structure before switching is provided (Fig. 8.4c). Upon increasing the applied tip bias further, to 3.5 V, domains in the film start to switch, resulting in a contrast change in both the lateral and vertical PFM images (Fig. 8.4d). Further increasing the bias to 4.0 V results in complete switching of the central square region (Fig. 8.4e). Based on the PFM images, the final switched domain structure is interpreted such that both domains initially possessing polarization P_3^+(orange regions, Fig. 8.4c) and in-plane oriented stripe domains P_2^- and P_2^+ (black and grey regions, Fig. 8.4c) are switched by 180° (Fig. 8.4f). These observations are consistent with the abrupt switching that occurs in a narrow field range in the polarization hysteresis loops and with the abrupt increase of dielectric response in the Rayleigh analysis. These results indicate that 180° switching reversal occurs in (101)-oriented films, in agreement with MD prediction.

Similar studies of (111)-oriented films, however, reveal decidedly different responses with a complex evolution of domain structures involving four characteristic steps in the switching (Fig. 8.5a-d). Detailed static domain structure characterization of the (111)-oriented films has been discussed above, and here we focus on an area possessing fully down-poled nanotwinned domain bands of a single type for simplicity (Fig. 8.5a). When applying a tip bias of –2.5 V to locally switch a 1 μm $\times$ 1 μm square region, only a small fraction of the domains switch (inset, Fig. 8.5b). Examination of the lateral PFM contrast reveals that the orientation of the long axes of the domains that were switched rotates by 90° in-the-plane of the film, resulting in a new domain configuration with a characteristic angle of 60° between the domain sub-bands (Fig. 8.5b). Upon further increasing the bias to 3.5 V, the majority of the square region subjected to the bias has been switched in the out-of-plane direction (inset, Fig. 8.5c) with the contrast changing accordingly in the lateral PFM images to reveal a characteristic angle of 60° between all domain sub-bands in the switched region (Fig. 8.5c). The domain structure does not exhibit further evolution until the applied tip bias exceeds –6 V. At this point, all domains in the square region subjected to the bias have been fully up-poled (inset, Fig. 8.5d). The nanotwinned domain pattern is observed to return to the initial orientation and reestablishes the characteristic angle of 120° between the long axes of the domains (Fig. 8.5d). Although a similar nanotwinned domain structure has been achieved, the in-plane contrast in the nanotwinned array has changed as compared to the initial state (i.e., sub-bands with dark PFM contrast become light and vice versa, Fig. 8.5d) suggesting that full switching is accompanied by an orientation change of the in-plane component of polarization.

This multi-step switching process is intriguing, and here we systematically analyze it. We provide schematic illustrations of the geometry of the sample including the crystallographic axes (Fig. 8.5e), the six possible polarization variants (Fig. 8.5f), and the twelve possible (six distinct) 90° domain boundaries (i.e., those between P_1^+–P_2^+ (P_1^-–P_2^-), P_1^+–P_3^+ (P_1^-–P_3^-), P_2^+–P_3^+ (P_2^-–P_3^-), P_1^+–P_2^- (P_1^-–P_2^+), P_1^+–P_3^- (P_1^-–P_3^+), P_2^+–P_3^- (P_2^-–P_3^+); each given a unique color in the figure) (Fig. 8.5g) projected on the (111) of the PFM image. Additional details about the geometry of the domain boundaries are provided. To aid the discussion, we provide schematic illustrations of the domain structures (Fig. 8.5h-o) in each distinct domain sub-band type for the four PFM images (Fig. 8.5a-d). Three different colors (orange, blue, and grey) are used to represent the three different polarization variants with solid and dashed lines corresponding to down- and up-poled versions, respectively. In the initial state (Fig. 8.5a), all domains are down-poled, and the dark (Fig. 8.5h) and light (Fig. 8.5i) domain sub-bands consist of alternating P_1^-/P_2^- and P_1^-/P_3^- domains, respectively. Upon application of the –2.5 V applied bias (Fig. 8.5b), the orientation of the domain boundaries in both the dark (Fig. 8.5j) and light (Fig. 8.5k) domain sub-bands are found to rotate by 90° in-the-plane of the film. Such a change in the domain boundary orientation can only be achieved by a complex switching process which includes three different switching events including 90° switching that maintains the vertical component of the polarization ($P_1^- \rightarrow P_2^-$, area 1, Fig. 8.5j), 180° switching ($P_1^- \rightarrow P_1^+$, area 2, Fig. 8.5j), and 90° switching that changes the vertical component of the polarization ($P_2^- \rightarrow P_1^+$, area 3, Fig. 8.5j) as well as regions that experience no switching ($P_2^- \rightarrow P_2^-$, area 4, Fig. 8.5j). Similar complex switching occurs in the light domain sub-bands as well (Fig. 8.5k). Upon further increasing the bias to 3.5 V (Fig. 8.5c), the orientation of the domain boundaries remains the same, but all domains are now up-poled (Fig. 8.5l,m) with a change of the in-plane contrast from light to dark (and vice versa) for the different domain sub-band types. This switching process includes 90° switching that maintains the vertical component of the polarization ($P_1^+ \rightarrow P_2^+$, Fig. 8.5l) and 90° switching that changes it ($P_2^- \rightarrow P_1^+$, Fig. 8.5l). Similar 90° switching events occur in the other domain sub-bands (Fig. 8.5m). Based on the PFM analysis, this up-poled domain structure should likely possess charged domain walls; however, it is not changed until the applied bias is further increased to –6 V (Fig. 8.5d). At this point, the domain boundaries are again rotated in-the-plane of the film by 90° and the domain structure is returned to a configuration consistent with the initial state (Fig. 8.5n,o), but with a change of the in-plane contrast in the PFM from light to dark (and vice versa) for the different domain sub-band types. Again, the domain walls in the final state are uncharged. This process is again accomplished by two types of 90° switching events that maintain the vertical component of the polarization ($P_1^+ \rightarrow P_2^+$ and $P_2^+ \rightarrow P_1^+$, Fig. 8.5n). Similar 90° switching events are observed for both domain sub-band types (Fig. 8.5o). In the end, regardless of how the switching is probed and acknowledging potential differences in the fine-scale nature of excitation and final domain structure produced by the different methodologies, the mechanisms underlying the switching events are innate to the materials. Thus the combination of macroscopic capacitor, scanning-probe, and MD studies provides a detailed, multiple length- and time-scale look at the switching in these materials. From these studies, we observe that (001)-/(101)-oriented films switch via 180° switching processes while (111)-oriented films undergo domain reorientation via 90° switching mediated processes.

8.2.4 Origin of successive ferroelastic switching

Although the nucleation and growth process for 180° switching events is fairly well understood, little evidence for 90° switching mediated domain reversal has been presented. It has been suggested that broadened (or double) current peaks during reverse switching of previously poled $PbZr_{0.415}Ti_{0.585}O_3$ ceramics could be the result of non-180° domain switching as a result of the residual stresses developed during forward poling [232] and that in single-crystals of [111]-oriented 95.5% $PbZn_{1/3}Nb_{2/3}O_3$–4.5% $PbTiO_3$, polarization reversal through intermediate polarization rotations of 71° and 109° can occur. citeYin01p4556, Daniels07p104108 Despite these observations, the mechanisms underlying such behavior are not entirely clear [32] and no direct measurements and examples of 90° switching mediated domain reversal have been reported in the literature. This is particularly the case for thin films where there are no reports in this regard. In thin films, the 90° domain switching process, due to the elastic clamping of the substrate, is thought to be so energetically costly that it does not typically occur. Enhanced 90° domain switching can be realized in thin films if the effect of clamping can be compensated by engineering specific film or domain structures such as in patterned ferroelectric layers [233] or through a layered structure where the top layer is anchored on an underneath layer of a secondary ferroelectric phase [234]. Here we have achieved the 90° switching mediated domain reversal process in thin films by utilizing (111)-oriented domain structures where the energetics are such that it permits these events to take place.

The preference for a 90° or 180° switching process in different films is ultimately controlled by the clamping of the ferroelectric film (and the resulting domain size). In both (001)-/(101)-oriented heterostructures, the elastic constraints from the substrate lead to dramatic differences in the fraction of in-plane and out-of-plane polarized domains (in particular, minimizing the fraction of in-plane polarized domains). Although 90° domain walls have lower domain wall energy than 180° domain walls [79], the 90° ferroelastic switching in thin films is generally unfavorable as compared to the 180° ferroelectric switching (as we observed for (001)-/(101)-oriented films in our simulations) under moderate electric fields because of the large energy penalty associated with the change of volume fractions of in-plane and out-of-plane polarized domains that must occur to accommodate such switching events [196]. Said another way, the free-energy change (Δf) for a ferroelastic 90° switching event is dominated by the contributions from the stress (σ^2) and the stress-polarization coupling (σP^2) terms. These energy terms are high in the (001)-/(101)-oriented films due to the elastic constraints of the substrate and the drastically different stress states for an in-plane or out-of-plane polarized domain. On the other hand, the (111)-oriented films possess three energetically-degenerate polarization variants (in a fully-poled state) all possessing in-plane and out-of-plane polarization components that are the same and, in effect, renders the elastic energy costs associated with a ferroelastic 90° switching event greatly reduced. Additionally, our MD simulations reveal that coordinated 90° switching events (i.e., $P_1^+ \rightarrow P_2^-$ and $P_2^+ \rightarrow P_1^-$) occur in essentially equal proportions across the entire domain width to accommodate (and maintain) both the elastic and electrostatic energy state of the system. As a result, the coordinated, multi-step 90° switching process will not incur a large elastic energy cost in agreement with the arguments above. Ultimately the preference of the 90° switching over the 180° switching in the (111)-oriented films is due to the lower kinetic barrier for 90° polarization rotation indicated by the lower energy of the 90° domain wall compared to that of the 180° domain wall.

The observation of such 90° switching mediated domain reversal, in turn, has important implications for our overall understanding of ferroelectric materials and their utilization in devices. First, the presence of active intermediate switching states can be correlated to the differences observed in the dielectric and ferroelectric response of the various orientations of films. Although all films possess high remnant polarization, the (001)-/(101)-oriented films show nearly square hysteresis loops with sharp electric field switching (consistent with 180° switching events), while (111)-oriented films exhibit more slanted hysteresis loops with larger coercive fields, indicative of switching at a broader range of fields and a multi-step switching process. Furthermore, it is likely that the availability of low-field intermediate switching can account for the observation of lower threshold fields for the nucleation of switching events in the Rayleigh studies of the (111)-oriented films. The domain reversal process is significantly impacted by changing the orientation of the epitaxial film and by allowing all possible switching types to be active in the material. Ultimately, if we can create pathways similar to those demonstrated in the stroboscopic PFM studies by which to deterministically stabilize or incrementally step the switched polarization from one state, through a number of intermediate states, before reaching the oppositely poled state, the possibility for creating new modalities of low-power, multi-state memory or logic are possible. At the same time, if we can determine ways to promote the 90° switching mediated domain reversal process, this could further accelerate the domain reversal and reduce the timescale of ferroelectrics thereby increasing their potential for use in advanced nanoelectronics.

8.2.5 Conclusion

In conclusion, we have observed both 180° and multi-step 90° switching domain reversal processes in $PbZr_{0.2}Ti_{0.8}O_3$ thin films. Using a combination of epitaxial thin-film growth, macro- and nano-scale characterization, and MD simulations, we have been able to manipulate the domain structure through the control of film orientations and explore the coupling between the domain structures and properties. Specifically, stark differences between (001)-/(101)- and (111)-oriented films were observed, with the latter exhibiting complex, nanotwinned ferroelectric domain structures with high densities of 90° domain walls, considerably broadened ferroelectric switching characteristics, and lower threshold fields for the onset of non-linearity during Rayleigh studies. Subsequent MD simulations and PFM studies reveal both types of switching mechanisms are possible, but that the switching process that ultimately occurs is determined by a combination of factors including domain wall energy, elastic strain, and domain size. These observations provide insight into a previously unexplored aspect of ferroelectric switching and highlight the complexity of these materials. Such studies are crucial for developing precise control of nanoscale ferroelectric materials and can potentially lead to interesting multi-state devices and accelerated switching in ferroelectrics.

8.3 Methods

8.3.1 Epitaxial thin film growth

The growth of the $PbZr_{0.2}Ti_{0.8}O_3$ was carried out at an oxygen pressure of 200 mtorr at 635°C with a laser fluence of 0.9-1.0 J/cm^2 and a laser repetition rate of 3 Hz. The growth of $SrRuO_3$ and $La_{0.7}Sr_{0.3}MnO_3$ were accomplished at oxygen pressures of 100 mtorr and 200 mtorr, respectively, at 645°C with laser repetition rates of 12 Hz and 3 Hz, respectively. After the growth, the samples were cooled at 5°C/min. in an oxygen pressure of 760 mtorr. We note that the crystal and domain structure and properties of $PbZr_{0.2}Ti_{0.8}O_3$ films grown on either $SrRuO_3$ or $La_{0.7}Sr_{0.3}MnO_3$ bottom electrodes are essentially the same and thus the data from heterostructures with both electrode layers are used interchangeably.

8.3.2 Crystal and domain structure characterization

X-ray $\theta - 2\theta$ scans were obtained by high-resolution x-ray diffraction (XPert MRD Pro equipped with a PIXcel detector, Panalytical). The piezoresponse force microscopy studies were carried out on a Cypher (Asylum Research) AFM using Ir/Pt-coated conductive tips (Nanosensor, PPP-NCLPt, force constant $\approx$48 N/m). The detailed polarization maps were generated under the single frequency vector PFM mode which enables the simultaneous imaging of the phase (θ) and amplitude (A) from both the lateral and vertical piezoresponse signal. To elucidate the PFM contrast, the PFM signals were processed in the form of a combination ($A \cos\theta$) of phase and amplitude. Electrical Measurements. All the electrical measurements were performed on capacitor structures of $PbZr_{0.2}Ti_{0.8}O_3$ films with symmetric electrodes of $SrRuO_3$ or $La_{0.7}Sr_{0.3}MnO_3$. The patterned circular top electrodes were fabricated by an MgO hard mask technique40 and the measurement was conducted on capacitors with the top electrode diameter ranging from 25 μm to 200 μm. The polarization-electric field hysteresis loops were measured using a Precision Multiferroic Tester (Radiant Technologies, Inc.). The room temperature permittivity was measured using an E4980A LCR meter (Agilent Technologies). All samples were pre-poled prior to the dielectric measurement. During the measurement, the bottom electrode was driven by an increasing AC electric field at 1 kHz.

8.3.3 Molecular dynamics simulations

Domain reversal in $PbTiO_3$ under applied electric fields was modeled with molecular dynamics. We use a bulk, stoichiometric $PbTiO_3$ supercell. We carry out molecular dynamics simulations under periodic boundary conditions with fixed dimensions. The supercell lengths and angles are slightly adjusted based on the volume fraction (γ) of the minority domain (green domains shown in Fig. 8.3) to simulate the mechanical clamping effect consistent with the epitaxial thin film in experiments. Although a thin film clamped in the two in-plane directions in principle can be modeled with a slab geometry, applying such a model with mixed elastic boundary conditions is technically difficult in MD simulations and will also complicate the understanding of the switching mechanism after introducing surface and size (thickness) effects. Our bulk model corresponds to a sample clamped in all three Cartesian directions. This was done by design to enable us to focus on the intrinsic response of the material, allowing us to separate the switching behavior due to domain structure and strain as opposed to that influence by the surface and other extrinsic effects. The simulations are performed with a bond-valence based interatomic potential with a timestep of 1.0 fs at 200 K. The domain structure is modeled with a $120a_1 \times 120a_2 \times 4a_3$ supercell, where a_1, a_2, and a_3 are the averaged lattice constants. The electric field is applied for 10 ps along $[\bar{1}0\bar{1}]$ to the supercell with γ= 0.2 and along $[\bar{1}\bar{1}\bar{1}]$ to the supercell with γ = 0.5, to resemble the actual field orientations experienced by the (101) and (111) thin films of similar volume fractions in experiments. After the field removal, we allow the system to evolve freely with supercell dimensions conserved. Since the structure and polarization of $PbZr_{0.2}Ti_{0.8}O_3$ are similar to those of $PbTiO_3$, we expect that the domain switching mechanisms modeled with $PbTiO_3$ are applicable to $PbZr_{0.2}Ti_{0.8}O_3$.

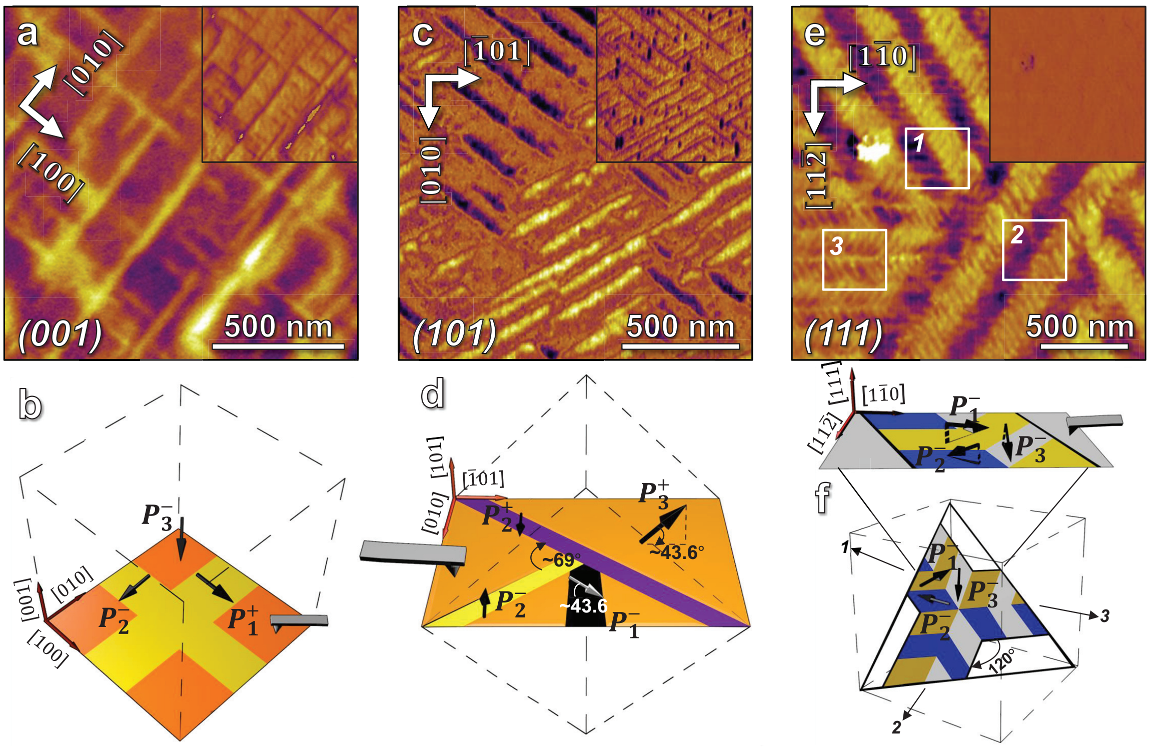

Figure 8.1: Piezoresponse force microscopy studies of $PbZr_{0.2}Ti_{0.8}O_3$ films. Lateral ($A\cos\theta$, combining phase θ and amplitude A) and vertical ($A\cos\theta$, inset) piezoresponse force microscopy images and schematic illustrations of the domain structures are provided for (001)-oriented heterostructures with majority P_3^- (orange) and minority P_1^+ and P_2^- domains (yellow) (a,b); (101)-oriented heterostructures with majority P_3^+ (with polarization oriented at $\approx 43.6°$ from the plane-of-the-film, orange) and minority, stripe-like P_2^+ and P_2^- domains (in-plane polarized, purple) and small fractions of P_1^- domains (with polarization oriented at $\approx 43.6°$ from the plane-of-the-film, black) (c,d); (111)-oriented heterostructures with complex nanotwinned domain structures wherein there are three degenerate polarization variants P_1^-,P_2^-,and P_3^- oriented at an angle of$\approx 33.9°$ from the plane of the film (represented by yellow, blue, and grey, respectively) which are tiled to produce three degenerate domain bands separated by $120°$ as labeled in the squares 1, 2, and 3 (e,f).

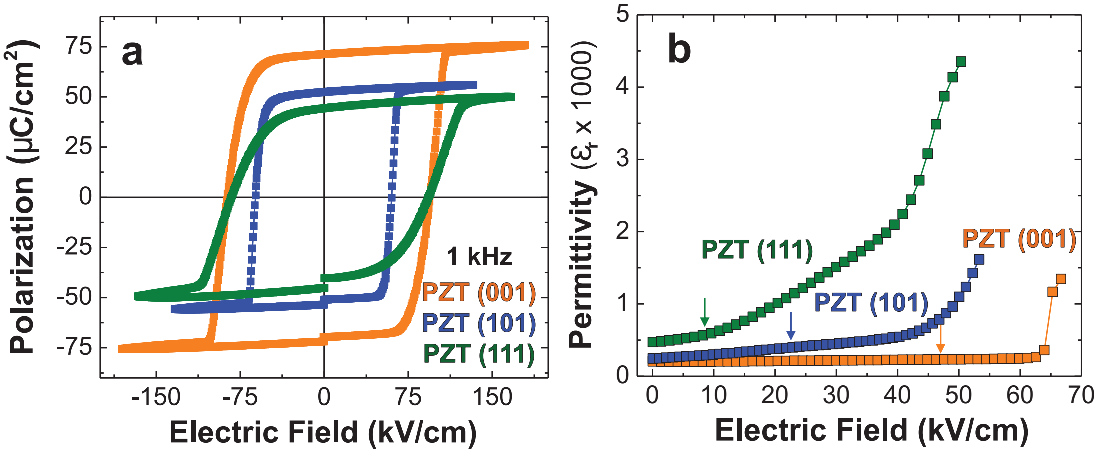

Figure 8.2: Electrical characterization of $PbZr_{0.2}Ti_{0.8}O_3$ films. (a) Polarization–electric field hysteresis loops measured at 1 kHz and (b) permittivity as a function of ac electric field measured at 1 kHz for (001)-, (101)-, and (111)-oriented $PbZr_{0.2}Ti_{0.8}O_3$ thin films. The arrows demarcate the location of the onset of non-linearity from the Rayleigh studies.

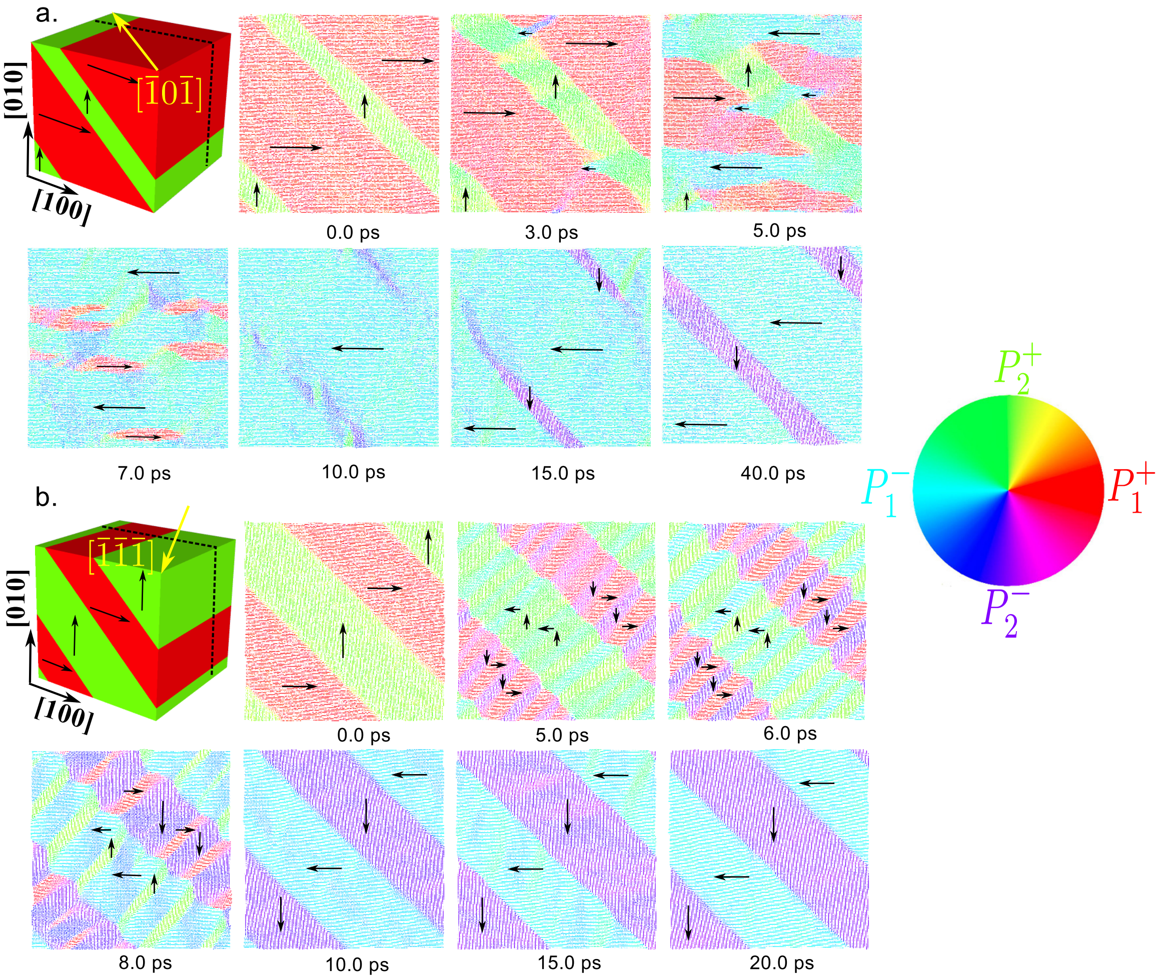

Figure 8.3: MD simulations of switching in ferroelectrics with 90° domain walls. For all simulations, the electric field is turned-on at 0.0 ps and off at 10 ps and allowed to relax at zero applied field from that point. (a) Domain evolution in (101)-oriented films possessing 20 volume % of minority P_2^+ domains (green) and 80 volume % of majority P_1^+ domains (red) under applied field along the $[\bar{1}0\bar{1}]$ (yellow arrow). Direct 180° polarization reversal is observed ($P_2^+ \rightarrow P_2^-$ and $P_1^+ \rightarrow P_1^-$). (b) Domain evolution in (111)-oriented films possessing 50 volume % P_2^+ domains (green) and 50 volume % of P_1^+ domains (red) under applied field along the $[\bar{1}\bar{1}\bar{1}]$ (yellow arrow). Only 90° polarization switching events ($P_2^+ \rightarrow P_1^-$ and $P_1^+ \rightarrow P_2^-$) are observed. The local polarization within each unit cell is represented by an arrow colored according to the polarization wheel.

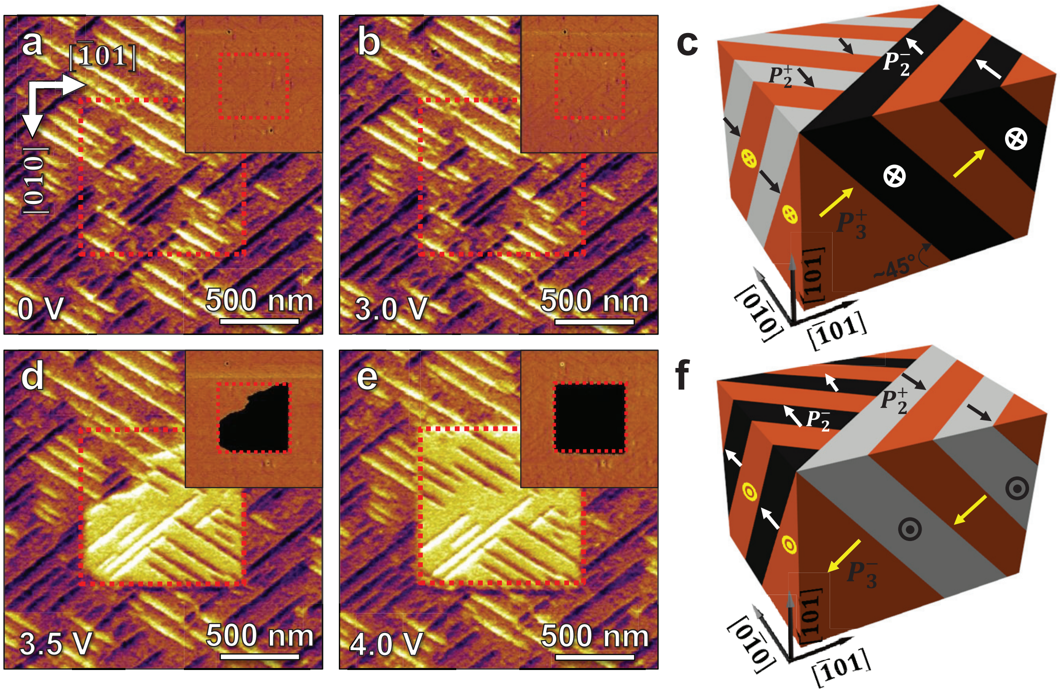

Figure 8.4: PFM switching studies of $PbZr_{0.2}Ti_{0.8}O_3$. Lateral ($A\cos\theta$, combining phase θ and amplitude A) and vertical (phase θ, inset) PFM images of field-dependent domain structure evolution in (101)-oriented $PbZr_{0.2}Ti_{0.8}O_3$ in the (a) as-grown state and (b) after applying a tip bias of 3.0 V in the central square region. (c) Schematic illustration of the observed, unswitched domain structure with the majority P_3^+ (orange domains, oriented at an angle of $43.6°$ from the plane of the film) and the stripe-like P_2^- (black domains) and P_2^+ (white domains) domains (in-plane polarized). Upon increasing the applied tip bias to (d) 3.5 V and (e) 4.0 V, abrupt switching is observed. (f) Schematic illustration of the switched domain structure in (d) and (e) with the majority P_3^- (orange domains), P_2^- (black domains), and P_2^+ (white domains) after the $180°$ switching.

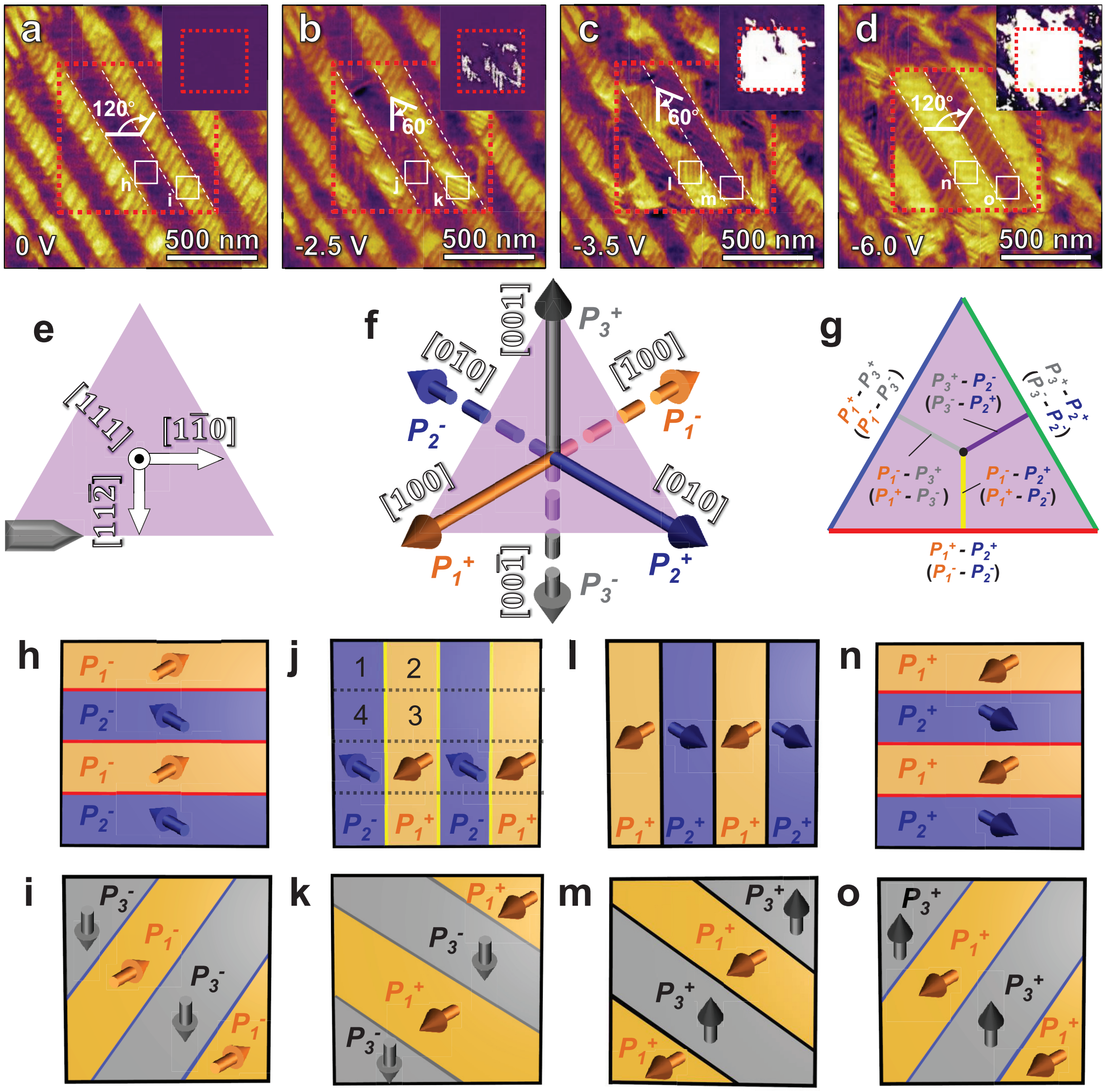

Figure 8.5: PFM switching studies of PbZr$_{0.2}$Ti$_{0.8}$O$_3$ (111) thin films. Lateral ($A\cos\theta$, combining phase θ and amplitude A) and vertical (phase θ, inset) PFM images of domain structure evolution in (111)-oriented PbZr$_{0.2}$Ti$_{0.8}$O$_3$ in the (a) initial down-poled state, after applying a tip bias of (b) -2.5 V (partial switching), (c) -3.5 V (complete out-of-plane, incomplete in-plane switching), and (d) -6.0 V (complete out-of-plane and in-plane switching). Schematic illustrations of the (e) projection of the crystallographic axes, (f) six possible polarization variants (solid and dashed pointing out and into the film plane, respectively), and (g) six possible distinct 90° domain boundaries (each given a unique color that is carried throughout the remaining panels). Additional illustrations of the switching process for dark and light domain bands, respectively, for the (h), (i) initial state, (j), (k) a majority down-poled intermediate state, (l), (m) an up-poled intermediate, and (n), (o) the final state.

Chapter 9

Ferroelectric domain wall induced band-gap reduction and charge separation in organometal halide perovskites

9.1 Introduction

The studies of organometal halide perovskites date back over a century [235, 236]. Their applications in photovoltaic devices have seen amazing improvements in past five years. In 2006, the device based on methyl ammonium lead tribromide, $CH_3NH_3PbBr_3$, had a power conversion efficiency of 2.2% [48]. The methyl ammonium lead triiodide ($CH_3NH_3PbI_3$) was later introduced as a light sensitizer in dye-sensitized solar cells by Kojima and coworkers in 2009, leading to an efficiency of 3.8% [49]. Since then, the power conversion efficiency of photovoltaic devices based on organometal halide perovskites has increased rapidly to nearly 20% [50, 51]. The high efficiency of $CH_3NH_3PbI_3$ [52] and its chlorine-doped derivative $CH_3NH_3PbI_{3-x}Cl_x$ [53, 54] is the result of their near optimal direct band gap ($\approx$1.55 eV) [49, 237], high optical absorption [238, 239], high carrier mobility [53, 240–244], and long carrier diffusion length [245]. Some organometal halide perovskites also exhibit room-temperature ferroelectricity [246]. First-principles density functional theory (DFT) calculations show a strong bulk polarization (0.38 C/m^2) in $CH_3NH_3PbI_3$ [247]. Recent DFT calculations demonstrate that the orientational order of the methylammonium (MA) cations will influence the magnitude of bulk polarization [248, 249]. It is suggested that the spontaneous polarization within these materials may enhance the charge separation and help achieve above-band-gap open circuit voltages [192, 247, 250].

Ferroelectric materials usually possess complex domain structures, with domain walls separating regions of homogeneously polarized domains. The domain wall is considered as a 2D topological defect and has been widely studied in inorganic ferroelectrics [25, 39, 163, 174, 183, 251, 252]. It has been demonstrated that domain walls can exhibit distinct electronic properties that are different from bulk materials [5, 253]. The presence of switchable ferroelectric domains in β-$CH_3NH_3PbI_3$ has been confirmed recently via piezoresponse force microscopy [246]. However, the local structure and the electronic properties of domain walls in organometal halide perovskites remain unknown. In this letter, we explore the energies and electronic structures of 180° and 90° domain walls in MAPbX_3(MA=CH_3NH_3,X=Cl, Br, I) via DFT. Both types of domain walls can be charged or uncharged, depending on the orientational order of the organic molecules around the domain boundaries. We find that a domain structure with charged walls will have a lower band gap than that of a single domain. On the contrary, the presence of uncharged walls has little impact on the band gap. Our calculations demonstrate the importance of these 2D topological defects and suggest a potential avenue to tune the band gap via domain engineering.

9.2 Results and discussion

9.2.1 180° domain wall in organometal halide perovskites

For our calculations, we have used the plane-wave density functional theory package QUANTUM–ESPRESSO [160] with Perdew-Burke-Ernzerhof (PBE) [106] density functional and norm conserving pseudopotentials generated from the OPIUM package [112, 115]. According to previous computational studies, a plane-wave cutoff energy of 50 Ry is sufficient to obtain well-converged results [249]. We first optimize the geometry of the orthorhombic 12-atom unit cell of $MAPbX_3$(X=Cl, Br, I). Figure 9.1 shows the optimized orthorhombic unit cells for MAPbX_3. Using Berry phase calculations, we find that the polarization, aligning with the molecular dipoles, is mostly along the x axis (P_x) with a value of 0.13 C/m^2 for $MAPbCl_3$, 0.12 C/m^2 for $MAPbBr_3$, and 0.12 C/m^2 for $MAPbI_3$. The hydrogen bond between the -NH_3 group and the halogen atom is critical for the bulk polarization. Additionally, as the dipoles of the MA cations are not perfectly aligned along the x axis, the unit cell has a small component of polarization ($\approx$0.04 C/m^2) along the z direction (P_z) shown in Fig. 9.1. For the simulation of the 180° domain wall, we use a supercell consisting of $1 \times 1 \times 6$ orthorhombic unit cells stacked along the z direction. The uncharged domain wall (UCDW) is constructed by rotating the orientations of MA cations in the right three cells such that the polarization changes from (P_x, 0, P_z) to (-P_x, 0, P_z) across the wall. On the other hand, the charged domain wall (CDW) has the polarization change from (P_x, 0, P_z) to (-P_x, 0, -P_z) across the domain boundary, with P_z component being discontinuous at the domain wall. The dimensions of the supercell are fixed to values based on the optimized lattice constants of the orthorhombic unit cell. The atomic positions are then fully relaxed using a $3 \times 3 \times 1$ Monkhorst-Pack k-point mesh [137]. We report in Fig. 9.1 the optimized domain structures with charged and uncharged 180° walls in MAPbI$_3$, MAPbBr$_3$, and MAPbCl$_3$. The domain wall energy (E_{DW}) is calculated by

$$E_{\mathrm{DW}} = \frac{E_{\mathrm{supercell}} - E_{\mathrm{bulk}}}{S_{\mathrm{DW}}} \tag{9.1}$$

where $E_{\mathrm{supercell}}$ is the energy of the supercell containing domain walls and E_{bulk} is the energy of a single domain supercell of the same size. S_{DW} is the domain wall area, and it is noted that each supercell includes two domain walls due to the application of periodic boundary conditions. We find that the uncharged wall has small domain wall energies (3 mJ/m^2 in MAPbCl$_3$, 1 mJ/m^2 in MAPbBr$_3$, and 8 mJ/m^2 in MAPbI$_3$). The energies for charged 180° domain walls in MAPbCl$_3$, MAPbBr$_3$, MAPbI$_3$, are 22 mJ/m^2, 28 mJ/m^2, and 33 mJ/m^2, respectively. These values are comparable to Ti-centered 180° domain walls in BaTiO$_3$ (17 mJ/m^2) [79]. The relatively low domain wall energy suggests that the formation of charged and uncharged domain walls are both energetically possible in hybrid perovskites.

The band gap is a crucial material factor for photovoltaic applications. We calculate the band structures for supercells with and without 180° domain walls. As shown in Table 1, the calculated PBE band gaps for single domains (E_g^{bulk}) are comparable to experimental [49, 237] and reported theoretical values [242, 243, 254]. Surprisingly, we find that domain structures with charged 180° domain walls have smaller band gaps (E_g^{180CDW}) than their single-domain counterparts, while structures with uncharged 180° domain walls have band gaps (E_g^{180UCDW}) similar to bulk values. Generally, a significant 20% band gap reduction is observed after introducing charged domain walls spaced by ≈1.5 nm in MAPbX_3. A larger supercell $1 \times 1 \times 8$ is employed to study the charged 180° walls in MAPbI$_3$, and a band gap reduction of 0.41 eV is observed. Spin-orbit coupling (SOC) is known to have a profound effect on the electronic structures of organometal halide perovskites [255–257], so we also evaluate the band gaps with PBE+SOC (Table 1). It is found that the band gaps with SOC are reduced by 0.20 eV in MAPbI$_3$, 0.29 eV inMAPbBr$_3$, and 0.43 eV in MAPbCl$_3$ due to charged domain walls. Figure 9.2 shows the band structures of MAPbI$_3$ with and without charged 180° walls. The band gap reduction results from the upshift of the valence band maximum (VBM) and the downshift of the conduction band minimum (CBM). Most notably, the presence of 180° walls removes the Rashba band splitting demonstrated in bulk MAPbI$_3$ [258], due to the recovery of symmetry (net zero polarization) for the whole supercell. The trend in band gap change in MAPbCl$_3$ is also examined with hybrid functional HSE06 [259, 260] with SOC. The band gap is reduced from 2.47 eV for the single domain to 2.08 eV for the structure with charged 180° domain walls, confirming the trend we observed with PBE.

In order to understand the origin of the band gap reduction, we analyzed the local density of states (LDOS) for a structure with charged 180° walls in MAPbI$_3$. Shown in Figure **??**a is the layer-resolved LDOS. The states near the band gap are mainly due to the hybridization between Pb and I atoms. The orbitals from the organic molecules are far away from the band gap, in agreement with previous theoretical work [242, 243]. As one can see from the layer-resolved LDOS, the CBM is located at domain wall A (Fig. 9.3 inset) which has P_z components meeting with a “head-to-head” configuration and the VBM is at domain wall B with a “tail-to-tail” configuration. A head-to-head domain wall has positive bound charges, while a tail-to-tail domain wall has negative bound charges [231]. This will give rise to an electric field across the domain, which is responsible for the shift of the CBM and the VBM [261]. The calculated electrostatic potential along the z direction shown in Fig. 9.3b has a zigzag shape, with domain wall A at the potential minimum and domain wall B at the potential maximum, revealing a built-in electrostatic field due to static uncompensated charge at domain walls. For comparison, we plot in-plane averaged electrostatic potential for the uncharged 180° walls in Fig. 9.3c. Since the P_z component is small and continuous across the uncharged 180° walls, a flat averaged potential profile is found.

Table 9.1: The band gaps (E_g in eV) for structures with and without 180° domain walls in MAPbX_3 calculated with PBE.

PBE	E_g^{bulk}	E_g^{180UCDW}	E_g^{180UCDW}-E_g^{bulk}	E_g^{180CDW}	E_g^{180CDW}-E_g^{bulk}
$\mathrm{MAPbCl_3}$	2.39	2.38	-0.01	1.89	-0.50
$\mathrm{MAPbBr_3}$	1.69	1.70	$+0.01$	1.30	-0.39
$\mathrm{MAPbI_3}$	1.58	1.56	-0.02	1.29	-0.29
PBE+SOC	E_g^{bulk}	E_g^{180UCDW}	E_g^{180UCDW}-E_g^{bulk}	E_g^{180CDW}	E_g^{180CDW}-E_g^{bulk}
$\mathrm{MAPbCl_3}$	1.35	1.32	-0.03	0.92	-0.43
$\mathrm{MAPbBr_3}$	0.67	0.67	$+0.00$	0.38	-0.29
$\mathrm{MAPbI_3}$	0.45	0.43	-0.02	0.25	-0.20

Table 9.2: The band gaps for structures with and without 90° domain walls in MAPbX_3 calculated with PBE.

PBE	E_g^{bulk}	E_g^{90UCDW}	E_g^{90UCDW}-E_g^{bulk}	E_g^{90CDW}	E_g^{90CDW}-E_g^{bulk}
$MAPbCl_3$	2.43	2.45	$+0.02$	1.62	-0.81
$MAPbBr_3$	1.80	1.83	$+0.03$	1.14	-0.66
$MAPbI_3$	1.75	1.70	-0.05	0.96	-0.79
PBE+SOC	E_g^{bulk}	E_g^{90UCDW}	E_g^{90UCDW}-E_g^{bulk}	E_g^{90CDW}	E_g^{90CDW}-E_g^{bulk}
$MAPbCl_3$	1.39	1.44	$+0.05$	1.06	-0.34
$MAPbBr_3$	0.78	0.83	$+0.05$	0.63	-0.15
$MAPbI_3$	0.63	0.59	-0.04	0.40	-0.23

9.2.2 90° domain wall in organometal halide perovskites

Further, we explore the 90° domain walls in MAPbX_3. Adopting a strategy similar to that for simulating 180° walls, we first relax the $\sqrt{2} \times \sqrt{2} \times 1$ unit cell of MAPbX_3. The structures of optimized unit cells have polarization along [100] ($P'_x \approx P'_y = \frac{1}{\sqrt{2}} P_{[100]}$) as shown in Fig. 9.4. The domain structure with 90° walls is then constructed by stacking six $\sqrt{2} \times \sqrt{2} \times 1$ cells along x, while rotating the orientations of MA molecules by 90° in the three unit cells on the right. The polarization changes from (P'_x, $-P'_y$, 0) to (P'_x, P'_y, 0) across the uncharged 90° domain wall (90UCDW) at [011] plane, and from (P'_x, $-P'_y$, 0) to ($-P'_x$, $-P'_y$, 0) across the charged 90° domain wall (90CDW). The atomic positions are relaxed with fixed supercell dimensions. It is worth noting that the 90CDW investigated here has the whole P'_x component being head-to-head.This configuration is generally not stable in bulk inorganic ferroelectrics due to the large depolarization filed at domain walls [262]. It is possible to construct a charged 90° wall by rotating the P'_x component such that only a small component being head-to-head (similar to the construction of charged 180° walls).

Figure 9.4 displays the geometries for the 90° domain walls. The energy differences between structures with and without 90UCDW are small (within 5 meV/formula unit), indicating negligible domain wall energies for the current setup. The energies for charged 90° domain walls in $\mathrm{MAPbCl_3}$, $\mathrm{MAPbBr_3}$ and $\mathrm{MAPbI_3}$, are 66 mJ/m^2, 54 mJ/m^2, and 56 mJ/m^2, respectively. These values, though higher than charged 180° domain walls, are still comparable to 90° domain walls in inorganic ferroelectrics such as $\mathrm{PbTiO_3}$ [79]. The results for band structure calculations with PBE and PBE+SOC are summarized in Table 2. It is found that charged 90° domain walls will significantly reduce the band gaps, and uncharged 90° domain walls have no impact on the band gaps, consistent with our findings for 180° domain walls. Figure 9.5 presents the computed potential across 90° domain walls in $\mathrm{MAPbCl_3}$. For the uncharged 90° walls, the potential decreases along the direction of the P_x within each domain. Also noticeable is the potential jump across the domain boundary.

This is caused by the dipole layer at the domain wall due to the variation of P_x across the boundary (Fig. 9.5a). As for the charged 90° walls, similar to charged 180° walls, the head-to-head wall is at the potential minimum and the tail-to-tail wall is at the potential maximum.

9.2.3 Domain wall induced charge separation

It is hypothesized that the ferroelectric domains in hybrid halide perovskites may aid the separation of photoexcited electrons and holes, and reduce recombination through the segregation of charge carriers [247]. Here we demonstrate that charged domain walls, both 180° and 90°, can serve as segregated channels for the motion of charge carriers. As illustrated in Fig. 9.6a, electrons prefer to diffuse to head-to-head charged domain walls and holes prefer to move to tail-to-tail charged domain walls. Then electrons and holes are likely to move separately along differently-charged domain walls under internal or external electric fields, reducing the rate of recombination. As for uncharged domain walls, the 180° wall may not result in a strong potential step for electron-hole separation, due to the small polarization component along the domain wall normal (Fig. 9.3c). However, uncharged 90° domain walls may act as dipole layers and give rise to significant potential steps, helping the carrier separation and increasing the diffusion lengths in hybrid halide perovskites (Fig. 9.6b).

9.3 Conclusion

In summary, the structures and electronic properties of ferroelectric 180° and 90° domain walls in $MAPbCl_3$, $MAPbBr_3$ and $MAPbI_3$ are studied via first-principles density functional theory. The domain wall energies in these materials are found to be small, suggesting that the formation of domain walls is energetically favorable. Most noticeably, we find that the presence of charged domain walls ("head-to-head" and "tail-to-tail") will reduce the band gap significantly, while the "head-to-tail" uncharged domain walls will not induce such reduction. Both 180° and 90° charged domain walls can serve as segregated channels for the diffusion of charge carriers. The presence of uncharged 90° domain wall may increase the diffusion length. It should be noted that the rotations of PbX_6 octahedrons are generally ignored in this investigation, partly due to the associated computational cost. Future investigations are required to fully understand the interplay between orientational order of organic molecules, rotations of inorganic octahedra, and the electronic structure of organometal halide perovskites. Our findings highlight the importance of ferroelectric domain walls in hybrid perovskites and also suggest a promising approach of device optimization via domain-wall engineering.

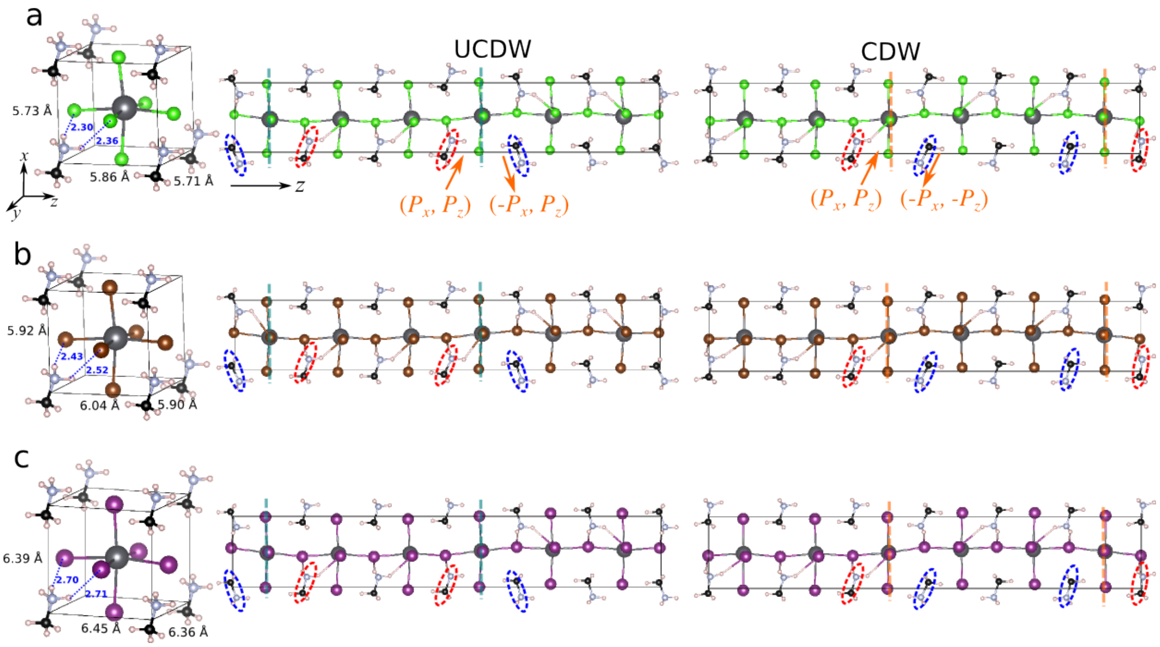

Figure 9.1: Optimized orthorhombic unit cells and domain structures with 180° domain walls in (a) $MAPbCl_3$, (b) $MAPbBr_3$, (c) $MAPbI_3$. The left panel is the relaxed orthorhombic unit cell. The middle panel is the side view of a $1 \times 1 \times 6$ supercell containing uncharged 180° domain walls (UCDW); the polarization changes from (P_x, P_z) to $(-P_x, P_z)$, as demonstrated with orange arrows. The right panel is the side view of a supercell with charged 180° domains (CDW); the polarization changes from (P_x, P_z) to $(-P_x, -P_z)$. The $X\cdots H{-}N$ hydrogen bond is displayed explicitly to help the visualization of different domains. Pb: dark grey, I: purple, Br: brown, Cl: green, C: black, N: light blue, H: light pink.

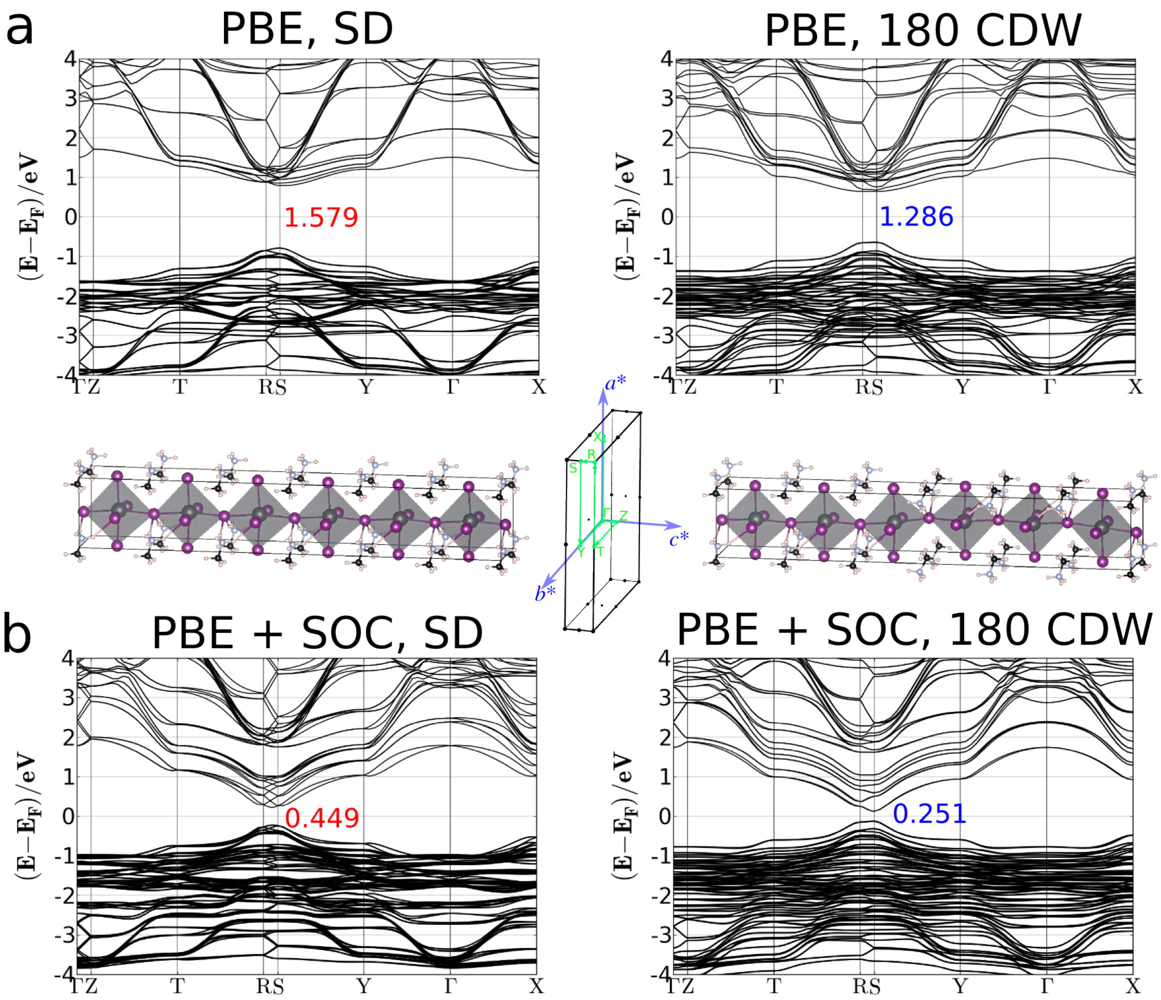

Figure 9.2: Calculated band structures for $\mathrm{MAPbI_3}$ (a) with PBE, and (b) with PBE and spin-orbit coupling (SOC). The left panel is for a single domain (SD) and the right panel is for structures with charged 180° domain walls (180 CDW). The Brillouin Zone and the k-point path for the $1 \times 1 \times 6$ supercell are displayed int the middle. Band gap values are in eV.

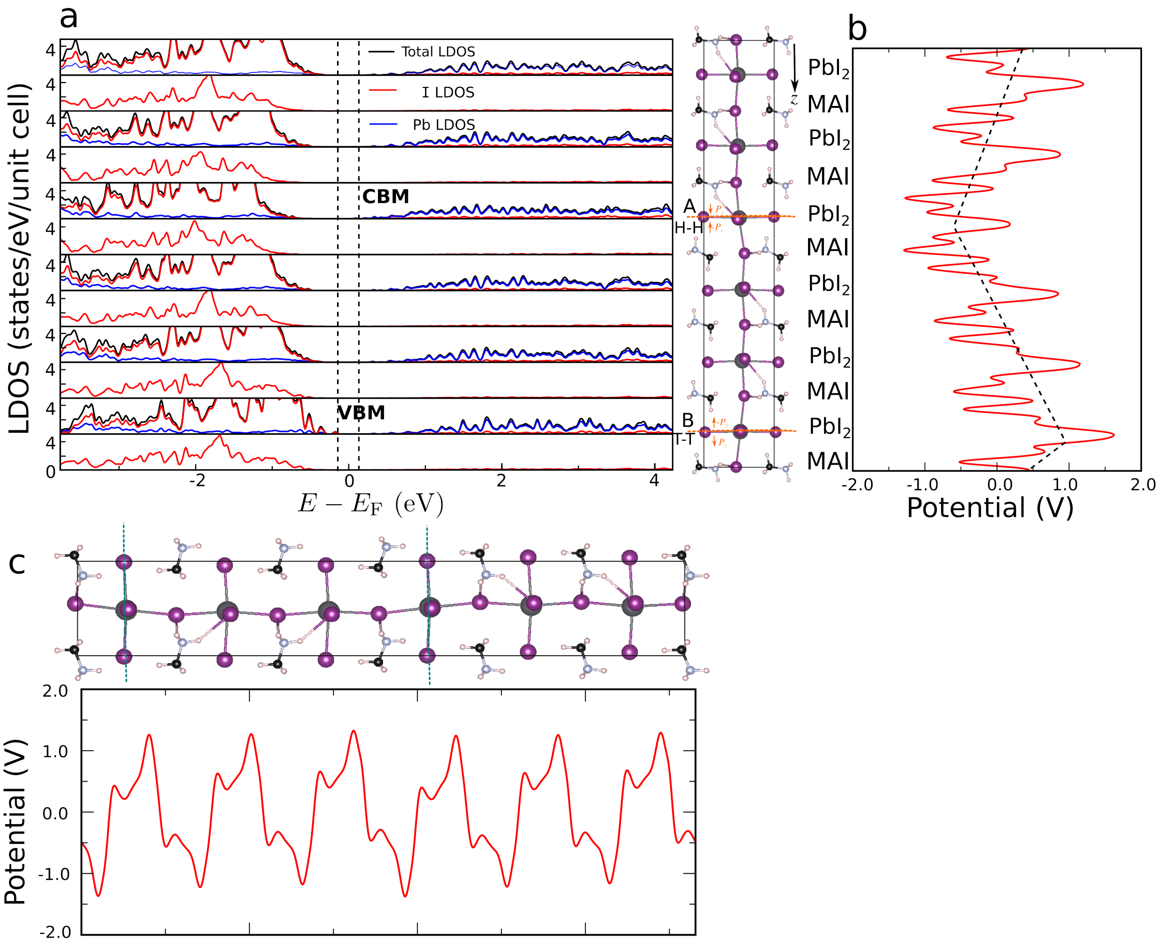

Figure 9.3: (a) Layer-resolved LDOS and (b) electrostatic potential along the z direction across charged 180° domain walls in $MAPbI_3$. The states near the band gap are mainly due to the hybridization between Pb and I atoms. The inset shows the domain structure with charged 180° domain walls labeled as A and B respectively. Domain A has a head-to-head (H-H) configuration. Domain B has a tail-to-tail (T-T) configuration.(c) Electrostatic potential across uncharged 180° domain walls in $MAPbI_3$.

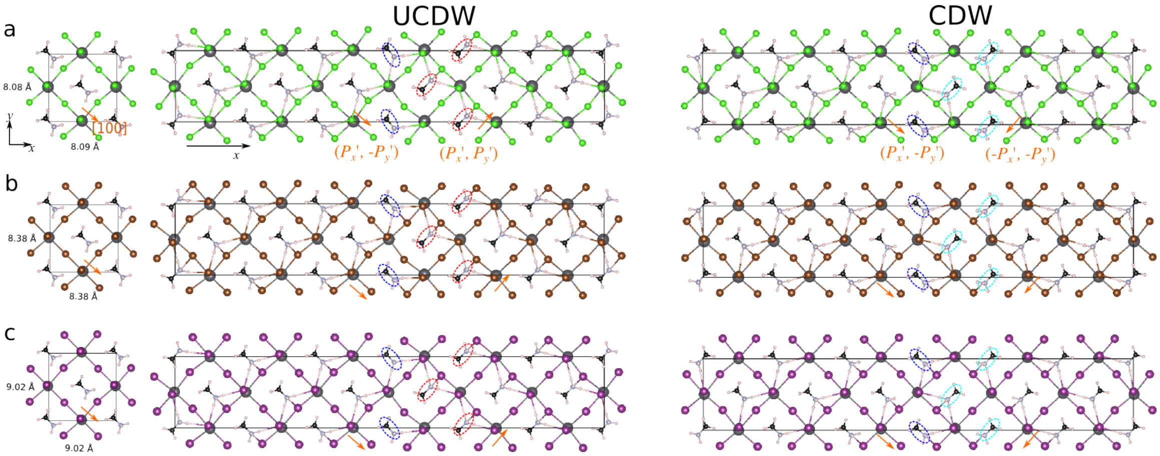

Figure 9.4: Optimized orthorhombic $\sqrt{2} \times \sqrt{2} \times 1$ unit cells and domain structures with 90° domain walls in (a) $MAPbCl_3$, (b) $MAPbBr_3$, (c) $MAPbI_3$. The left panel is the relaxed 20-atom unit cell. The middle panel is the side view of a $6\sqrt{2} \times \sqrt{2} \times 1$ supercell with uncharged 90° walls. The right panel is the side view of a supercell with charged 90° walls. The orange arrows represent the directions of the polarization. The $X \cdots H–N$ hydrogen bond is displayed explicitly to help the visualization of different domains. Pb: dark grey, I: purple, Br: brown, Cl: green, C: black, N: light blue, H: light pink.

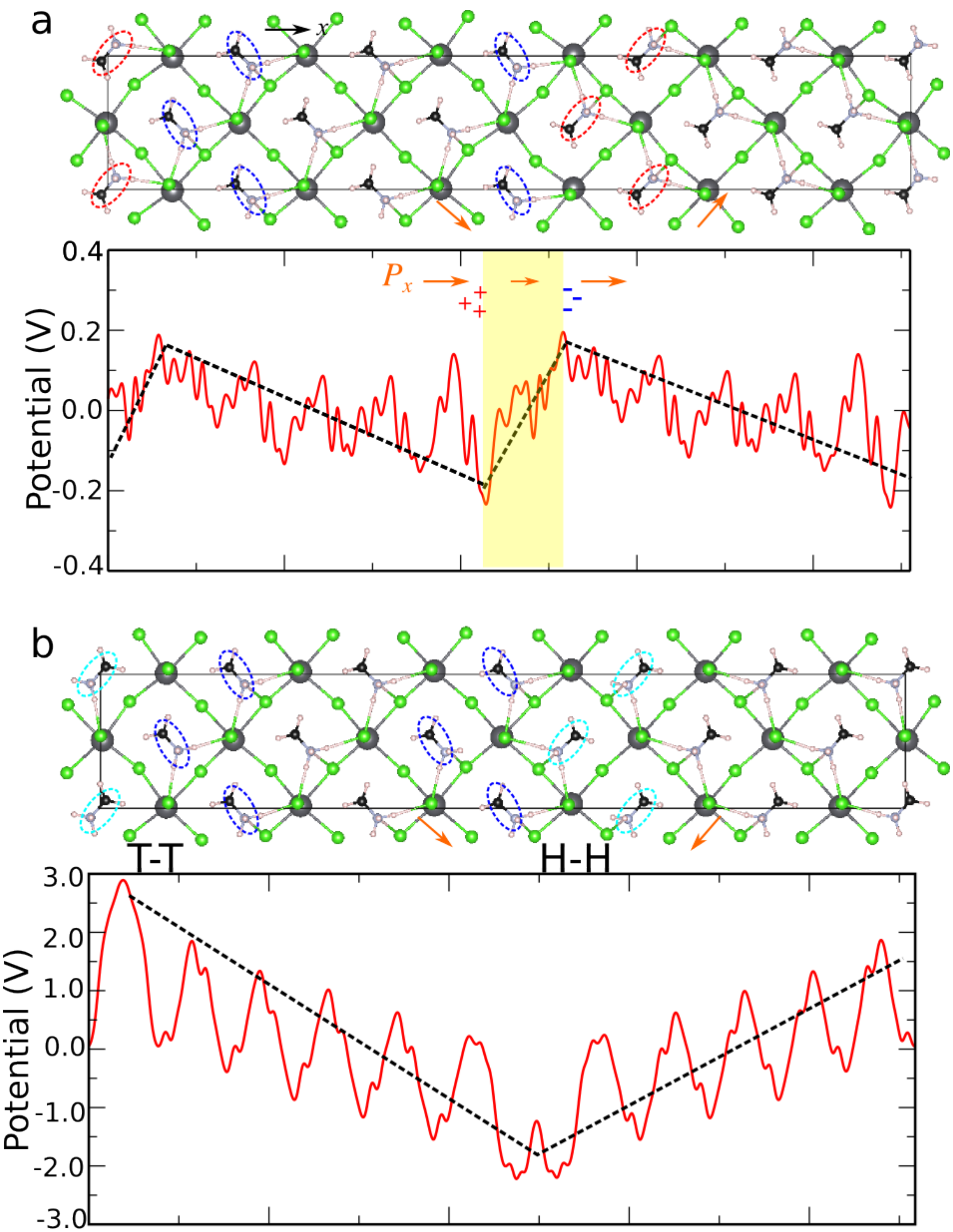

Figure 9.5: Electrostatic potential across (a) uncharged and (b) charged 90° domain walls in $MAPbCl_3$. The black broken lines are guidelines for eyes.

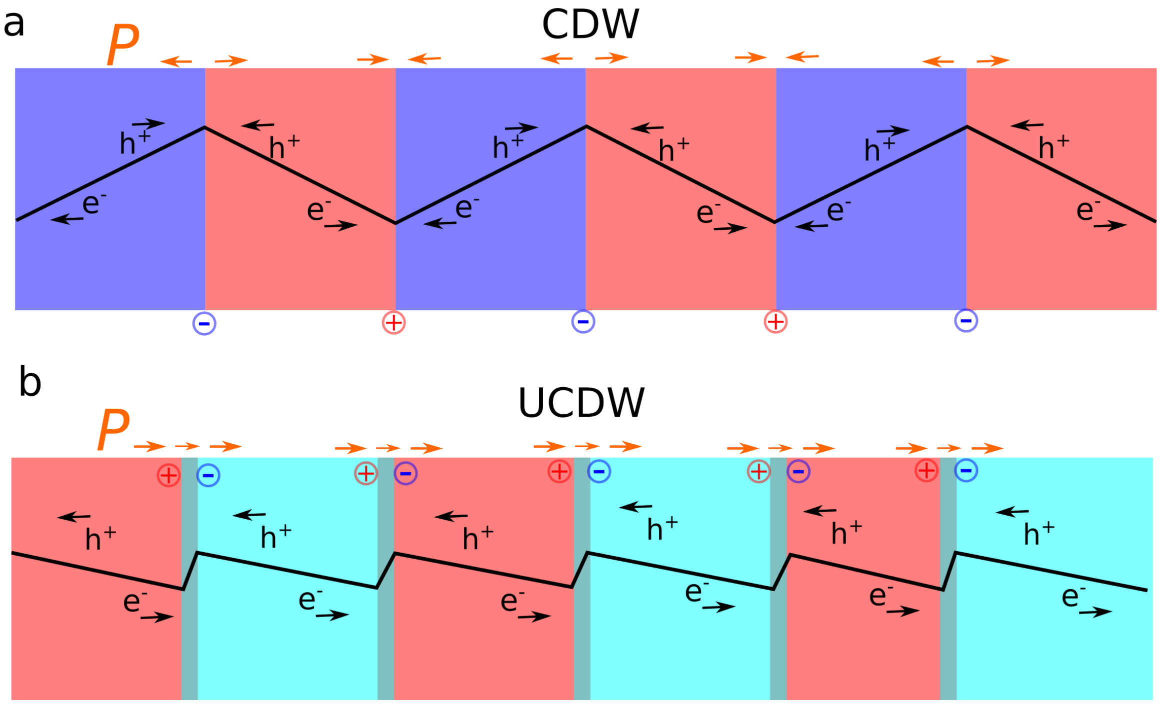

Figure 9.6: Schematic illustrations of electrostatic potential steps and electron-hole separations in a periodic array of (a) charged domain walls and (b) uncharged domain walls. ⊕ and ⊖ represent bound positive and negative charges.

Chapter 10

Future Research

The internal structure and the motion of domain walls in ferroelectric materials can have a profound influence on the dielectric, piezoelectric, pyroelectric, and electronic properties of ferroelectrics. Many questions remain unanswered about the microscopic origin of these domain-wall related properties. It is of great importantance to understand various structure-property relationships of ferroelectric domain walls, and to discover, develop and demonstrate new material-design principles and engineering strategies for optimized and breakthrough applications of ferroelectrics.

10.1 Susceptibility from stationary domain walls

The effect of domain wall motion on the ferroelectric susceptibility has been widely recognized and studied [184, 185, 188]. Recently, the stationary contribution resulting from the response of the ferroelectric materials within the finite width of the domain walls to an applied stimulus has received increased attention [187, 263]. It is suggested that non-motional contributions could be 6-78 times larger than the bulk response [187]. However, the origin of the stationary contribution is currently unknown. I will use first-principles density functional theory (DFT) calculations to explore the effects of domain walls on the dielectric and piezoelectric properties of ferroelectric materials with varying domain sizes, domain wall densities and periodicities. Taking the 180° and 90° domains walls in the prototypic ferroelectric $PbTiO_3$ as examples, I will calculate the frequency-dependent dielectric constants and the e_{33} and d_{33} piezoelectric coefficients. The key local structural and electronic features within the domain wall and their connections to the macroscopic susceptibility will be identified. This work will also be coupled with classical molecular dynamics (MD) simulations to investigate large supercells ($>$ 200 atoms) that are not accessible via conventional DFT methods. Based on the results from the DFT and MD simulations, I will seek to develop an analytical model that accurately describes the relationship between the domain-wall-related descriptors (e.g., density and thickness) and the susceptibility. This model will allow us to generalize the findings from $PbTiO_3$ to other materials, enabling performance optimization through domain patterning.

10.2 Single domain switching driven by an electric field

The polarization reversal in single crystals of ferroelectrics is generally understood by a nucleation-and-growth mechanism. As shown in Fig. 10.1, under an external electric field applied in reverse of the direction of bulk polarization, oppositely polarized domains, preferably at electrode-crystal interfaces or at defects, will emerge, expand, and grow into the bulk, which eventually will lead to the reversal of the whole domain. However, the theoretical values for the nucleation activation energy ($\approx 10^6 - 10^8\ k_BT$) according to Landauer's calculations [264] are several orders of magnitude larger than experimental values ($\approx 10k_BT$) [1]. In the past several decades, various studies have been done to resolve Landauer's paradox [37, 265, 266]. During my thesis work, I have explored the nucleation-and-growth mechanism at the 90° domain wall and found a diamond-like nucleus exhibiting a diffusive boundary with a gradual polarization change. However, the nucleation mechanism in single crystals without extrinsic topological defects (e.g., interfaces, domain walls and point defects) remains unclear. This works aims to resolve the Landauer's paradox with atomistic insights from MD simulations and first-principles calculations.

I will carry out MD simulations to examine the nucleation-and-growth mechanism in a single crystal with a large supercell size (320,000 atoms) in $PbTiO_3$ and $BiFeO_3$ using bond-valence-based force fields. The key processes for the single domain switching will be identified, and the dependence of the switching speed on external variables (temperatures, electric fields and elastic boundary conditions) will be determined. Comparison of the switching mechanisms in tetragonal $PbTiO_3$ and rhombohedral $BiFeO_3$ will reveal the role of crystal symmetry in electric polarization switching. I will examine the size and the three-dimensional shape of the critical nucleus in a single crystal. The detailed nucleation mechanism elucidated from MD simulations can be used to construct an analytical model based on Landau-Ginzburg-Devonshire (LGD) theory, to relate the nucleation energy to the fundamental characteristics of the material assessable via DFT calculations. The estimated nucleation barriers can then be used in a stochastic kinetic Monte Carlo (KMC) calculation to simulate switching in different types of ferroelectrics that occurs in μm length and second time scales, comparable to experimental conditions. This multi-scale scheme will enable a quantitative resolution of Landauer's paradox and provide atomistic insights into the ferroelectric switching.

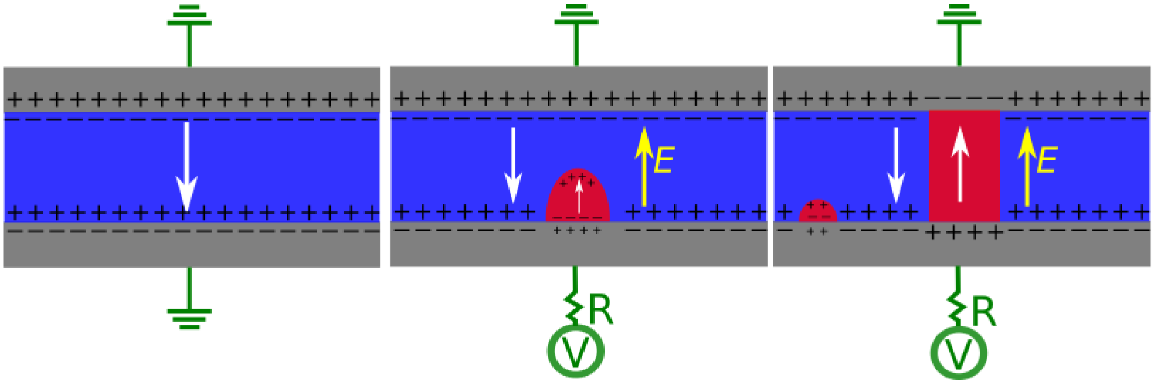

Figure 10.1: Schematic diagram showing the nucleation-and-growth mechanism for the polarization reversal in a single crystal. The sample is sandwiched by metal electrodes and is prepolarized downward under the short circuit condition (left panel); A small spike-shaped domain of reversed polarization is formed at the electrode-crystal interface under a upward electric field (middle panel); The nucleus will grow and eventually lead to the domain reversal (right panel).

Bibliography

[1] Lines, M. E.; Glass, A. M. *Principles and Applications of Ferroelectrics and Related Materials*; Clarendon Press: Oxford, 1977.

[2] Yang, S. M.; Jo, J. Y.; Kim, D. J.; Sung, H.; Noh, T. W.; Lee, H. N.; Yoon, J. . G.; Song, T. K. *Appl. Phys. Lett.* **2008**, *92*, 252901–1–3.

[3] Kim, T. H.; Baek, S. H.; Yang, S. M.; Jang, S. Y.; Ortiz, D.; Song, T. K.; Chung, J. . S.; Eom, C. B.; Noh, T. W.; Yoon, J. . G. *Appl. Phys. Lett.* **2009**, *95*, 262902–1–3.

[4] Scott, J. F. *Science* **2007**, *315*, 954–959.

[5] Seidel, J.; Martin, L. W.; He, Q.; Zhan, Q.; Chu, Y.-H.; Rother, A.; Hawkridge, M.; Maksymovych, P.; Yu, P.; Gajek, M.; et al. *Nature Mater.* **2009**, *8*, 229–234.

[6] Eom, C. B.; Trolier-McKinstry, S. *MRS Bull.* **2012**, *37*, 1007–1021.

[7] Wessels, B. W. *Annu. Rev. Mater. Res.* **2007**, *37*, 659–679.

[8] Zhong, W.; King-Smith, R. D.; Vanderbilt, D. *Phys. Rev. Lett.* **1994**, *72*, 3618–22.

[9] Cohen, R. E. *Nature* **1992**, *358*, 136–138.

[10] Grinberg, I.; Rappe, A. M. *Phys. Rev. B* **2004**, *70*, 220101–1–4.

[11] Pettifor, D. G.; Oleinik, I. I. *Phys. Rev. B* **1999**, *59*, 8487–8499.

[12] Sepliarsky, M.; Cohen, R. E. *AIP Conf. Proc.* **2002**, *626*, 36–44.

[13] Sepliarsky, M.; Stachiotti, M. G.; Migoni, R. L. *Phys. Rev. B* **2005**, *72*, 014110–1–6.

[14] Grinberg, I.; Cooper, V. R.; Rappe, A. M. *Nature* **2002**, *419*, 909–911.

[15] Pettifor, D. G.; Oleinik, I. I.; Nguyen-Manh, D.; Vitek, V. *Comp. Mat. Sci.* **2002**, *23*, 33–7.

[16] Shin, Y.-H.; Cooper, V. R.; Grinberg, I.; Rappe, A. M. *Phys. Rev. B* **2005**, *71*, 054104–1–4.

[17] van Duin, A. C.; Merinov, B. V.; Han, S. S.; Dorso, C. O.; Goddard Iii, W. A. *J. Phys. Chem. A* **2008**, *112*, 11414–11422.

[18] Aoki, M.; Nguyen-Manh, D.; Pettifor, D. G.; Vitek, V. *Prog. Mater Sci.* **2007**, *52*, 154–195.

[19] Shimada, T.; Wakahara, K.; Ulmeno, Y.; Kitamura, T. *J. Phys. Condens. Matter* **2008**, *20*, 325225–1–11.

[20] Zhong, W.; Vanderbilt, D.; Rabe, K. M. *Phys. Rev. B* **1995**, *52*, 6301–12.

[21] Waghmare, U. V.; Rabe, K. M. *Phys. Rev. B* **1997**, *55*, 6161–6173.

[22] Wojdeł, J. C.; Hermet, P.; Ljungberg, M. P.; Ghosez, P.; Íñiguez, J. *J. Phys.: Condens. Matter* **2013**, *25*, 305401–1–25.

[23] Phillpot, S. R.; Sinnott, S. B.; Asthagiri, A. *Annu. Rev. Mater. Res.* **2007**, *37*, 239–270.

[24] Brown, I. D. *Chem. Rev.* **2009**, *109*, 6858–6919.

[25] Shin, Y.-H.; Grinberg, I.; Chen, I.-W.; Rappe, A. M. *Nature* **2007**, *449*, 881–6.

[26] Grinberg, I.; Shin, Y.-H.; Rappe, A. M. *Phys. Rev. Lett.* **2009**, *103*, 197601–1–4.

[27] Hiroyuki Takenaka, I. G.; Rappe, A. M. *Phys. Rev. Lett.* **2013**, *110*, 147602–1–147602–5.

[28] Harvey, M. A.; Baggio, S.; Baggio, R. *Acta Crystallogr. B* **2006**, *62*, 1038–1042.

[29] Bhide, V. G.; Hegde, M. S.; Deshmukh, K. G. *J. Am. Chem. Soc.* **1968**, *51*, 565–68.

[30] Moreau, J. M.; Michel, C.; Gerson, R.; James, W. J. *J. Phys. Chem. Solids* **1971**, *32*, 1315–1320.

[31] Catalan, G.; Scott, J. F. *Adv. Mater.* **2009**, *21*, 2463–2485.

[32] Pramanick, A.; Prewitt, A. D.; Forrester, J. S.; Jones, J. L. *Crit. Rev. Solid State Mater. Sci.* **2012**, *37*, 243–275.

[33] Merz, W. J. *Phys. Rev.* **1954**, *95*, 690–698.

[34] Miller, R. C.; Savage, A. *Phys. Rev.* **1959**, *115*, 1176–84.

[35] Miller, R. C.; Weinreich, G. *Phys. Rev.* **1960**, *117*, 1460–1466.

[36] Pertsev, N.; Petraru, A.; Kohlstedt, H.; Waser, R.; Bdikin, I.; Kiselev, D.; Kholkin, A. *Nanotechnology* **2008**, *19*, 375703 1–7.

[37] Jo, J. Y.; Kim, D. J.; Kim, Y. S.; Choe, S.-B.; Song, T. K.; Yoon, J.-G.; Noh, T. W. *Phys. Rev. Lett.* **2006**, *97*, 247602 1–3.

[38] Jo, J.; Han, H.; Yoon, J.-G.; Song, T.; Kim, S.-H.; Noh, T. *Phys. Rev. Lett.* **2007**, *99*, 267602–1–4.

[39] Jo, J.; Yang, S.; Kim, T.; Lee, H.; Yoon, J.-G.; Park, S.; Jo, Y.; Jung, M.; Noh, T. W. *Phys. Rev. Lett.* **2009**, *102*, 045701–1–4.

[40] Tybell, T.; Paruch, P.; Giamarchi, T.; Triscone, J.-M. *Phys. Rev. Lett.* **2002**, *89*, 097601–1–4.

[41] Paruch, P.; Giamarchi, T.; Triscone, J.-M. *Phys. Rev. Lett.* **2005**, *94*, 197601–1–4.

[42] Paruch, P.; Giamarchi, T.; Tybell, T.; Triscone, J.-M. *J. Appl. Phys.* **2006**, *100*, 051608 1–10.

[43] Pertsev, N.; Kiselev, D.; Bdikin, I.; Kosec, M.; Kholkin, A. *J. Appl. Phys.* **2011**, *110*, 052001–1–5.

[44] Rodriguez, B. J.; Nemanich, R.; Kingon, A.; Gruverman, A.; Kalinin, S.; Terabe, K.; Liu, X.; Kitamura, K. *Appl. Phys. Lett.* **2005**, *86*, 012906–1–3.

[45] Rodriguez, B. J.; Jesse, S.; Bokov, A. A.; Ye, Z.-G.; Kalinin, S. *Appl. Phys. Lett.* **2009**, *95*, 092904–092904.

[46] Paruch, P.; Guyonnet, J. *C. R. Phys.* **2013**, *14*, 667–684.

[47] Jin, L.; Li, F.; Zhang, S. *J. Am. Ceram. Soc.* **2014**, *97*, 1–27.

[48] Kojima, A.; Teshima, K.; Miyasaka, T.; Shirai, Y. In *Meeting Abstracts*; The Electrochemical Society; pp 397–397.

[49] Kojima, A.; Teshima, K.; Shirai, Y.; Miyasaka, T. *J. Am. Chem. Soc.* **2009**, *131*, 6050–6051.

[50] Zhou, H.; Chen, Q.; Li, G.; Luo, S.; Song, T.-b.; Duan, H.-S.; Hong, Z.; You, J.; Liu, Y.; Yang, Y. *Science* **2014**, *345*, 542–546.

[51] Jeon, N. J.; Lee, H. G.; Kim, Y. C.; Seo, J.; Noh, J. H.; Lee, J.; Seok, S. I. *J. Am. Chem. Soc.* **2014**, *136*, 7837–7840.

[52] Burschka, J.; Pellet, N.; Moon, S.-J.; Humphry-Baker, R.; Gao, P.; Nazeeruddin, M. K.; Grätzel, M. *Nature* **2013**, *499*, 316–319.

[53] Lee, M. M.; Teuscher, J.; Miyasaka, T.; Murakami, T. N.; Snaith, H. J. *Science* **2012**, *338*, 643–647.

[54] Liu, M.; Johnston, M. B.; Snaith, H. J. *Nature* **2013**, *501*, 395–398.

[55] Valasek, J. *Phys. Rev.* **1921**, *17*, 475–480.

[56] Valasek, J. *Phys. Rev.* **1922**, *19*, 478–491.

[57] Valasek, J. *Phys. Rev.* **1922**, *20*, 639–664.

[58] Valasek, J. *Phys. Rev.* **1924**, *24*, 560–568.

[59] Megaw, H. D.; *Crystal structure of barium titanate*; 1945.

[60] Ogawa, S. *J. Phys. Soc. Jpn.* **1946**, *1*, 32–33.

[61] Von Hippel, A.; Breckenridge, R. G.; Chesley, F.; Tisza, L. *Ind. Eng. Chem.* **1946**, *38*, 1097–1109.

[62] Bhalla, A.; Guo, R.; Roy, R. *Mater. Res. Innov.* **2000**, *4*, 3–26.

[63] Sawaguchi, E.; Maniwa, H.; Hoshino, S. *Phys. Rev.* **1951**, *83*, 1078.

[64] Park, S.-E.; Shrout, T. R. *J. Appl. Phys.* **1997**, *82*, 1804–11.

[65] Shirane, G.; Hoshino, S. *J. Phys. Soc. Jpn.* **1951**, *6*, 265–270.

[66] Kubel, F.; Schmid, H. *Acta Cryst.* **1990**, *B46*, 698–702.

[67] Rabe, K. M.; Ahn, C. H.; Triscone, J.-M. *Physics of ferroelectrics: a modern perspective*; Springer Science & Business Media, 2007; Vol. 105.

[68] Arlt, G. *J. Mat. Sci.* **1990**, *25*, 2655–2666.

[69] Dawber, M.; Rabe, K. M.; Scott, J. F. *Rev. Mod. Phys.* **2005**, *77*, 1083–1130.

[70] Okuyama, M.; Ishibashi, Y. *Ferroelectric thin films: basic properties and device physics for memory applications*; Springer Science & Business Media, 2005; Vol. 98.

[71] Güthner, P.; Dransfeld, K. *Appl. Phys. Lett.* **1992**, *61*, 1137–1139.

[72] Kolosov, O.; Gruverman, A.; Hatano, J.; Takahashi, K.; Tokumoto, H. *Phys. Rev. Lett.* **1995**, *74*, 4309–4312.

[73] Hidaka, T.; Maruyama, T.; Saitoh, M.; Mikoshiba, N.; Shimizu, M.; Shiosaki, T.; Wills, L.; Hiskes, R.; Dicarolis, S.; Amano, J. *Appl. Phys. Lett.* **1996**, *68*, 2358–2359.

[74] Kalinin, S. V.; Rodriguez, B. J.; Borisevich, A. Y.; Baddorf, A. P.; Balke, N.; Chang, H. J.; Chen, L. Q.; Choudhury, S.; Jesse, S.; Maksymovych, P.; Nikiforov, M. P.; Pennycook, S. J. *Adv. Mater.* **2010**, *22*, 314–322.

[75] Gruverman, A.; Rodriguez, B. J.; Dehoff, C.; Waldrep, J. D.; Kingon, A. I.; Nemanich, R. J.; Cross, J. S. *Appl. Phys. Lett.* **2005**, *87*, 082902–1–3.

[76] Soergel, E. *J. Phys. D: Appl. Phys.* **2011**, *44*, 464003.

[77] Kalinin, S. V.; Rodriguez, B. J.; Jesse, S.; Shin, J.; Baddorf, A. P.; Gupta, P.; Jain, H.; Williams, D. B.; Gruverman, A. *Microsc. Microanal.* **2006**, *12*, 206–220.

[78] Pöykkö, S.; Chadi, D. J. *Appl. Phys. Lett.* **1999**, *75*, 2830–2.

[79] Meyer, B.; Vanderbilt, D. *Phys. Rev. B* **2002**, *65*, 104111–1–11.

[80] Tsai, F.; Khiznichenko, V.; Cowley, J. *Ultramicroscopy* **1992**, *45*, 55–63.

[81] Foeth, M.; Sfera, A.; Stadelmann, P.; Buffat, P.-A. *J. Elec. Micro.* **1999**, *48*, 717–23.

[82] Stemmer, S.; Streiffer, S.; Ernst, F.; Rüuhle, M. *Philos. Mag. A* **1995**, *71*, 713–724.

[83] Tybell, T.; Paruch, P.; Giamarchi, T.; Triscone, J.-M. *Phys. Rev. Lett.* **2002**, *89*, 097601–1–4.

[84] Kim, S.; Gopalan, V.; Gruverman, A. *Appl. Phys. Lett.* **2002**, *80*, 2740–2742.

[85] Beckman, S.; Wang, W.; Rabe, K. M.; Vanderbilt, D. *Phys. Rev. B* **2009**, *79*, 144124–1–8.

[86] Kitamura, K.; Furukawa, Y.; Niwa, K.; Gopalan, V.; Mitchell, T. E. *Appl. Phys. Lett.* **1998**, *73*, 3073–3075.

[87] Gopalan, V.; Mitchell, T. E.; Furukawa, Y.; Kitamura, K. *Appl. Phys. Lett.* **1998**, *72*, 1981–1983.

[88] Lente, M.; Picinin, A.; Rino, J.; Eiras, J. *J. Appl. Phys.* **2004**, *95*, 2646–2653.

[89] Lente, M.; Eiras, J. *J. Appl. Phys.* **2001**, *89*, 5093–5099.

[90] Kong, L.; Ma, J. *Mater. Lett.* **2001**, *51*, 95–100.

[91] Shrout, T. R.; Zhang, S. J. *J. Electroceram.* **2007**, *19*, 113–126.

[92] Chauve, P.; Giamarchi, T.; Le Doussal, P. *Phys. Rev. B* **2000**, *62*, 6241–6267.

[93] Payne, M. C.; Teter, M. P.; Allan, D. C.; Arias, T. A.; Joannopoulos, J. D. *Rev. Mod. Phys.* **1992**, *64*, 1045–1097.

[94] Rapaport, D. C. *The art of molecular dynamics simulation*; Cambridge University Press, 2004.

[95] Frenkel, D.; Smit, B. *Understanding molecular simulation: from algorithms to applications*; Academic Press, 2001; Vol. 1.

[96] Born, M.; Oppenheimer, J. R. *Ann. Phys.* **1927**, *84*, 457–484.

[97] Pisana, S.; Lazzeri, M.; Casiraghi, C.; Novoselov, K. S.; Geim, A. K.; Ferrari, A. C.; Mauri, F. *Nature Mater.* **2007**, *6*, 198–201.

[98] Hartree, D. R. In *Mathematical Proceedings of the Cambridge Philosophical Society*; Cambridge Univ Press; pp 89–110.

[99] Thomas, L. H. In *Mathematical Proceedings of the Cambridge Philosophical Society*; Cambridge Univ Press; pp 542–548.

[100] Fermi, E. *Rend. Accad. Naz. Lincei* **1927**, *6*, 602–607.

[101] Hohenberg, P.; Kohn, W. *Phys. Rev.* **1964**, *136*, B864–71.

[102] Kohn, W.; Sham, L. J. *Phys. Rev.* **1965**, *140*, A1133–8.

[103] Perdew, J. P.; Wang, Y. *Phys. Rev. B* **1992**, *45*, 13244–9.

[104] MA, S.-K.; Brueckner, K. A. *Phys. Rev.* **1968**, *165*, 18–31.

[105] Perdew, J. P.; Chevary, J. A.; Vosko, S. H.; Jackson, K. A.; Pederson, M. R.; Singh, D. J.; Fiolhais, C. *Phys. Rev. B* **1992**, *46*, 6671–6687.

[106] Perdew, J. P.; Burke, K.; Ernzerhof, M. *Phys. Rev. Lett.* **1996**, *77*, 3865–8.

[107] Phillips, J. C. *Physical Review* **1958**, *112*, 685–695.

[108] Phillips, J. C.; Kleinman, L. *Phys. Rev.* **1959**, *116*, 287–94.

[109] Hamann, D. R.; Schlüter, M.; Chiang, C. *Phys. Rev. Lett.* **1979**, *43*, 1494–7.

[110] Bachelet, G. B.; Hamann, D. R.; Schlüter, M. *Phys. Rev. B* **1982**, *26*, 4199–4228.

[111] Bachelet, G. B.; Schlüter, M. *Phys. Rev. B* **1982**, *25*, 2103–2108.

[112] Rappe, A. M.; Rabe, K. M.; Kaxiras, E.; Joannopoulos, J. D. *Phys. Rev. B Rapid Comm.* **1990**, *41*, 1227–30.

[113] Troullier, N.; Martins, J. L. *Phys. Rev. B* **1991**, *43*, 1993–2006.

[114] Kleinman, L.; Bylander, D. M. *Phys. Rev. Lett.* **1982**, *48*, 1425–8.

[115] Ramer, N. J.; Rappe, A. M. *Phys. Rev. B* **1999**, *59*, 12471–8.

[116] Maitland, G. C. *Intermolecular forces: their origin and determination*; Oxford University Press, 1981.

[117] Verlet, L. *Phys. Rev.* **1967**, *159*, 98–103.

[118] Hünenberger, P. H. In *Advanced computer simulation*; Springer, 2005; pp 105–149.

[119] Andersen, H. C. *J. Chem. Phys.* **1980**, *72*, 2384–2393.

[120] Nosé, S. *J. Chem. Phys.* **1984**, *81*, 511–519.

[121] Hoover, W. G. *Phys. Rev. A* **1985**, *31*, 1695–7.

[122] Nosé, S. *Mol. Phys.* **1984**, *52*, 255–268.

[123] Parrinello, M.; Rahman, A. *Phys. Rev. Lett.* **1980**, *45*, 1196.

[124] Shin, Y.-H.; Son, J.-Y.; Lee, B.-J.; Grinberg, I.; Rappe, A. M. *J. Phys.: Condens. Matter* **2008**, *20*, 015224–1–5.

[125] Brown, I.; Shannon, R. *Acta Cryst.* **1973**, *A 29*, 266–82.

[126] Brown, I.; Wu, K. K. *Acta. Cryst.* **1976**, *B32*, 1957–9.

[127] Finnis, M.; Sinclair, J. *Philos. Mag. A* **1984**, *50*, 45–55.

[128] Sutton, A. P. *Electronic Structure of Materials*; Oxford University Press, 1993.

[129] Horsfield, A.; Bratkovsky, A.; Fearn, M.; Pettifor, D.; Aoki, M. *Phys. Rev. B* **1996**, *53*, 12694–12712.

[130] F, C.-L. *J. Phys. Chem. Solids* **1968**, *29*, 1235–1243.

[131] Cyrot-Lacmann, F. *Phys. Rev. B* **1980**, *22*, 2744–2748.

[132] Ducastelle, F.; Cyrot-Lacmann, F. *J. Phys. Chem. Solids* **1971**, *32*, 285–301.

[133] Carlsson, A. E.; Ashcroft, N. W. *Phys. Rev. B* **1983**, *27*, 2101–2110.

[134] Hansen, L.; Stoltze, P.; Jacobsen, K. W.; Nørskov, J. K. *Phys. Rev. B* **1991**, *44*, 6523–6526.

[135] Plimpton, S. *J. Comput. Phys.* **1995**, *117*, 1–19.

[136] Gonze, X.; et al. *Comp. Mater. Sci.* **2002**, *25*, 478–92.

[137] Monkhorst, H. J.; Pack, J. D. *Phys. Rev. B* **1976**, *13*, 5188–5192.

[138] Perdew, J.; Ruzsinszky, A.; Gábor, C.; Vydrov, O.; Scuseria, G.; Constantin, L.; Zhou, X.; Burke, K. *Phys. Rev. Lett.* **2008**, *100*, 136406–1–4.

[139] Zhao, Y.; Truhlar, D. G. *J. Chem. Phys.* **2008**, *128*, 184109–1–8.

[140] Wu, Z.; Cohen, R. E. *Phys. Rev. Lett.* **2005**, *95*, 037601–1–4.

[141] Ganesh, P.; Cohen, R. *J. Phys.: Condens. Matter* **2009**, *21*, 064225–1–4.

[142] Ahart, M.; Somayazulu, M.; Cohen, R. E.; Ganesh, P.; Dera, P.; Mao, H. K.; Hemley, R. J.; Ren, P., Y. a nd Liermann; Wu, Z. G. *Nature* **2008**, *451*, 545–548.

[143] Liu, S.; Grinberg, I.; Rappe, A. M. *J. Physics.: Condens. Matter* **2013**, *25*, 102202–1–6.

[144] Wang, J.; Neaton, J. B.; Zheng, H.; Nagarajan, V.; Ogale, S. B.; Liu, B.; Viehland, D.; Vaithyanathan, V.; Schlom, D. G.; Waghmare, U. V.; Spaldin, N. A.; Rabe, K. M.; Wuttig, M.; Ramesh, R. *Science* **2003**, *299*, 1719–1722.

[145] Fiebig, M.; Lottermoser, T.; Frohlich, D.; Goltsev, A. V.; Pisarev, R. V. *Nature* **2002**, *419*, 818–820.

[146] Kimura, T.; Goto, T.; Shintani, H.; Ishizaka, K.; Arima, T.; Tokura, Y. *Nature* **2003**, *426*, 55–58.

[147] Eerenstein, W.; Mathur, N. D.; Scott, J. F. *Nature* **2006**, *442*, 759–65.

[148] Zhao, T.; Scholl, A.; Zavaliche, F.; Lee, K.; Barry, M.; Doran, A.; Cruz, M. P.; Chu, Y. H.; Ederer, C.; Spaldin, N. A.; Das, R. R.; Kim, D. M.; Baek, S. H.; Eom, C. B.; Ramesh, R. *Nat. Mater.* **2006**, *5*, 823–829.

[149] Ramesh, R.; Spaldin, N. *Nat. Mater.* **2007**, *6*, 21–29.

[150] Zeches, R. J.; et al. *Science* **2009**, *326*, 977–980.

[151] Neaton, J. B.; Ederer, C.; Waghmare, U. V.; Spaldin, N. A.; Rabe, K. M. *Phys. Rev. B* **2005**, *71*, 014113.

[152] Baettig, P.; Ederer, C.; Spaldin, N. A. *Phys. Rev. B* **2005**, *72*, 214105–1–8.

[153] Ravindran, P.; Vidya, R.; Kjekshus, A.; Fjellvåg, H. *Phys. Rev. B* **2006**, *74*, 224412–1–18.

[154] Lee, J.-H.; Oak, M.-A.; Choi, H. J.; Son, J. Y.; Jang, H. M. *J. Mater. Chem.* **2012**, *22*, 1667–1672.

[155] Prosandeev, S.; Kornev, I. A.; Bellaiche, L. *Phys. Rev. Lett.* **2011**, *107*, 117602–1–5.

[156] Kornev, I. A.; Lisenkov, S.; Haumont, R.; Dkhil, B.; Bellaiche, L. *Phys. Rev. Lett.* **2007**, *99*, 227602–1–4.

[157] Albrecht, D.; Lisenkov, S.; Ren, W.; Rahmedov, D.; Kornev, I. A.; Bellaiche, L. *Phys. Rev. B* **2010**, *81*, 140401–1–4.

[158] Prosandeev, S.; Kornev, I. A.; Bellaiche, L. *Phys. Rev. B* **2011**, *83*, 020102–1–4.

[159] Liu, S.; Grinberg, I.; Takenaka, H.; Rappe, A. M. *Phys. Rev. B* **2013**, *88*, 104102–1–7.

[160] Giannozzi, P.; et al. *J. Phys.: Condens. Matter* **2009**, *21*, 395502–20.

[161] http://opium.sourceforge.net.

[162] Lubk, A.; Gemming, S.; Spaldin, N. A. *Phys. Rev. B* **2009**, *80*, 104110–1–8.

[163] Liu, S.; Grinberg, I.; Rappe, A. M. *Appl. Phys. Lett.* **2013**, *103*, 232907–1–4.

[164] Sepliarsky, M.; Stachiotti, M. G.; Migoni, R. L. *Phys. Rev. B* **2005**, *72*, 014110–1–6.

[165] Zhong, W.; Vanderbilt, D.; Rabe, K. M. *Phys. Rev. Lett.* **1994**, *73*, 1861–4.

[166] Garcia, A.; Vanderbilt, D. *Appl. Phys. Lett.* **1998**, *72*, 2981–3.

[167] Bellaiche, L.; Garcia, A.; Vanderbilt, D. *Phys. Rev. Lett.* **2000**, *84*, 5427–30.

[168] Palewicz, A.; Przenioslo, R.; Sosnowska, I.; Hewat, A. W. *Acta Crystallogr., Sect. B: Struct. Sci* **2007**, *63*, 537–544.

[169] Arnold, D. C.; Knight, K. S.; Morrison, F. D.; Lightfoot, P. *Phys. Rev. Lett.* **2009**, *102*, 027602–1–4.

[170] Diéguez, O.; Aguado-Puente, P.; Junquera, J.; Íñiguez, J. *Phys. Rev. B* **2013**, *87*, 024102–1–11.

[171] Scott, J. F. *Ferroelectric memories*; Springer Science & Business Media, 2000; Vol. 3.

[172] Rabe, K. A.; Dawber, M.; Lichtensteiger, C.; Ahn, C. H.; Triscone, J. M. *Topics in Applied Physics* **2007**, *105*, 1–30.

[173] Lu, H.; Bark, C. . W.; Esque de los Ojos, D.; Alcala, J.; Eom, C. B.; Catalan, G.; Gruverman, A. *Science* **2012**, *336*, 59–61.

[174] Catalan, G.; Seidel, J.; Ramesh, R.; Scott, J. F. *Rev. Mod. Phys.* **2012**, *84*, 119–156.

[175] Scott, J. F. *International Scholarly Research Notices* **2013**, *2013*, 1–24.

[176] Molotskii, M.; Rosenwaks, Y.; Rosenman, G. *Annu. Rev. Mater. Res.* **2007**, *37*, 271–296.

[177] Sharma, P.; McQuaid, R. G. P.; McGilly, L. J.; Gregg, J. M.; Gruverman, A. *Adv. Mater.* **2013**, *25*, 1323–1330.

[178] Thomas, L.; Hayashi, M.; Jiang, X.; Moriya, R.; Rettner, C.; Parkin, S. *Science* **2007**, *315*, 1553–1556.

[179] Thomas, L.; Moriya, R.; Rettner, C.; Parkin, S. S. P. *Science* **2010**, *330*, 1810–1813.

[180] Dawber, M.; Jung, D. J.; Scott, J. F. *Appl. Phys. Lett.* **2003**, *82*, 436–438.

[181] Kim, Y.; Han, H.; Lee, W.; Baik, S.; Hesse, D.; Alexe, M. *Nano Lett.* **2010**, *10*, 1266–1270.

[182] Kittel, C. *Phys. Rev.* **1951**, *83*, 458–458.

[183] Seidel, J. *J. Phys. Chem. Lett.* **2012**, *3*, 2905–2909.

[184] Zhang, Q.; Wang, H.; Kim, N.; Cross, L. *J. Appl. Phys.* **1994**, *75*, 454–459.

[185] Taylor, D.; Damjanovic, D. *J. Appl. Phys.* **1997**, *82*, 1973–1975.

[186] Karthik, J.; Damodaran, A.; Martin, L. *Phys. Rev. Lett.* **2012**, *108*, 167601–1–5.

[187] Xu, R.; Karthik, J.; Damodaran, A. R.; Martin, L. W. *Nat. Comm.* **2014**, *5*, 3120–1–7.

[188] Xu, F.; Trolier-McKinstry, S.; Ren, W.; Xu, B.; Xie, Z.-L.; Hemker, K. *J. Appl. Phys.* **2001**, *89*, 1336–48.

[189] Chaplya, P. M.; Carman, G. P. *J. Appl. Phys.* **2001**, *90*, 5278–5286.

[190] Seifert, A.; Muralt, P.; Setter, N. *Appl. Phys. Lett.* **1998**, *72*, 2409–2411.

[191] Karthik, J.; Martin, L. *Appl. Phys. Lett.* **2011**, *99*, 032904–1–9.

[192] Yang, S. Y.; Seidel, J.; Byrnes, S. J.; Shafer, P.; Yang, C.-H.; Rossell, M. D.; Yu, P.; Chu, Y.-H.; Scott, J. F.; Ager III, J. W.; Martin, L. W.; Ramesh, R. *Nat. Nanotech.* **2010**, *5*, 143–147.

[193] Salje, E. K. H. *ChemPhysChem* **2010**, *11*, 940–950.

[194] Wang, J.; Shi, S.-Q.; Chen, L.-Q.; Li, Y.; Zhang, T.-Y. *Acta Mater.* **2004**, *52*, 749–764.

[195] Gureev, M.; Mokrỳ, P.; Tagantsev, A.; Setter, N. *Phys. Rev. B* **2012**, *86*, 104104 1–10.

[196] Gao, P.; Britson, J.; Jokisaari, J. R.; Nelson, C. T.; Baek, S.-H.; Wang, Y.; Eom, C.-B.; Chen, L.-Q.; Pan, X. *Nature Commun.* **2013**, *4*, 2791–1–9.

[197] Tang, Y.; Zhu, Y.; Wang, Y.; Wang, W.; Xu, Y.; Ren, W.; Zhang, Z.; Ma, X. *Sci. Rep.* **2014**, *4*, 4115–1–9.

[198] Yang, S. M.; Jo, J. Y.; Kim, T.; Yoon, J.-G.; Song, T.; Lee, H. N.; Marton, Z.; Park, S.; Jo, Y.; Noh, T. W. *Phys. Rev. B* **2010**, *82*, 174125–1–7.

[199] Hall, D. *J. Mater. Sci.* **2001**, *36*, 4575–4601.

[200] Wu, K.; Schulze, W. A. *J. Am. Ceram. Soc.* **1992**, *75*, 3385–3389.

[201] Buscaglia, M. T.; Viviani, M.; Buscaglia, V.; Mitoseriu, L.; Testino, A.; Nanni, P.; Zhao, Z.; Nygren, M.; Harnagea, C.; Piazza, D.; Galassi, C. *Phys. Rev. B* **2006**, *73*, 064114–1–10.

[202] Ren, W.; Yang, Y.; Diéguez, O.; Íñiguez, J.; Choudhury, N.; Bellaiche, L. *Phys. Rev. Lett.* **2013**, *110*, 187601 1–5.

[203] Wang, Y.; Nelson, C.; Melville, A.; Winchester, B.; Shang, S.; Liu, Z.-K.; Schlom, D. G.; Pan, X.; Chen, L.-Q. *Phys. Rev. Lett.* **2013**, *110*, 267601–1–5.

[204] Guo, E.-J.; Dörr, K.; Herklotz, A. *Appl. Phys. Lett.* **2012**, *101*, 242908–1–5.

[205] Hoffman, J.; Pan, X.; Reiner, J. W.; Walker, F. J.; Han, J.; Ahn, C. H.; Ma, T. *Advanced Materials* **2010**, *22*, 2957–2961.

[206] Martin, L. W.; Schlom, D. G. *Curr. Opin. Sol. State Mater. Sci.* **2012**, *16*, 199–215.

[207] Nagarajan, V.; Jenkins, I. G.; Alpay, S. P.; Li, H.; Aggarwal, S.; Salamanca-Riba, L.; Roytburd, A. L.; Ramesh, R. *J. Appl. Phys.* **1999**, *86*, 595–602.

[208] Li, Y. L.; Hu, S. Y.; Liu, Z. K.; Chen, L. Q. *Appl. Phys. Lett.* **2002**, *81*, 427–429.

[209] Pertsev, N. A.; Arlt, G.; Zembilgotov, A. G. *Microelectron. Eng.* **1995**, *29*, 135–140.

[210] Kim, D.-J.; Maria, J.-P.; Kingon, A. I.; Streiffer, S. K. *J. Appl. Phys.* **2003**, *93*, 5568–5574.

[211] Bruchhaus, R.; Pitzer, D.; Schreiter, M.; Wersing, W. *J. Electroceram.* **1999**, *3*, 151–162.

[212] Karthik, J.; Martin, L. *Phys. Rev. B* **2011**, *84*, 024102–1–9.

[213] Pertsev, N. A.; Kukhar, V. G.; Kohlstedt, H.; Waser, R. *Phys. Rev. B* **2003**, *67*, 054107–1–10.

[214] Pertsev, N. A.; Zembilgotov, A. G. *J. Appl. Phys.* **1996**, *80*, 6401–6406.

[215] Saito, K.; Kurosawa, T.; Akai, T.; Oikawa, T.; Funakubo, H. *J. Appl. Phys.* **2003**, *93*, 545–550.

[216] Oikawa, T. *Journal of Applied Physics* **2004**, *95*, 3111–3115.

[217] Bernal, A.; Zhang, S. J.; Bassiri-Gharb, N. *Appl. Phys. Lett.* **2009**, *95*, 142911–1–3.

[218] Wada, S.; Yako, K.; Kakemoto, H.; Tsurumi, T.; Kiguchi, T. *J. Appl. Phys.* **2005**, *98*, 014109–1–7.

[219] Grigoriev, A.; Do, D. H.; Kim, D. M.; Eom, C. B.; Adams, B.; Dufresne, E. M.; Evans, P. G. *Phys. Rev. Lett.* **2006**, *96*, 187601–1–4.

[220] Jo, J. Y.; Chen, P.; Sichel, R. J.; Callori, S. J.; Sinsheimer, J.; Dufresne, E. M.; Dawber, M.; Evans, P. G. *Phys. Rev. Lett.* **2011**, *107*, 055501–1–4.

[221] Zubko, P.; Stucki, N.; Lichtensteiger, C.; Triscone, J.-M. *Phys. Rev. Lett.* **2010**, *104*, 187601–1–4.

[222] Nelson, C. T.; et al. *Science* **2011**, *334*, 968–971.

[223] Winkler, C. R.; Damodaran, A. R.; Karthik, J.; Martin, L. W.; Taheri, M. L. *Micron* **2012**, *43*, 1121–1126.

[224] Chang, H. J.; Kalinin, S. V.; Yang, S.; Yu, P.; Bhattacharya, S.; Wu, P. P.; Balke, N.; Jesse, S.; Chen, L. Q.; Ramesh, R.; Pennycook, S. J.; Borisevich, A. Y. *J. Appl. Phys.* **2011**, *110*, 052014–1–6.

[225] Sepilarsky, M.; Phillpot, S. R.; Wolf, D.; Stachiotti, M. G.; Migoni, R. L. *Appl. Phys. Lett.* **2000**, *76*, 3986–3988.

[226] Roitburd, A. L. *Phys. Status Solidi A* **1976**, *37*, 329–339.

[227] Ouyang, J.; Slusker, J.; Levin, I.; Kim, D. M.; Eom, C. B.; Ramesh, R.; Roytburd, A. L. *Adv. Funct. Mater.* **2007**, *17*, 2094–2100.

[228] Romanov, A. E.; Vojta, A.; Pompe, W.; Lefevre, M. J.; Speck, J. S. *Phys. Status Solidi A* **1999**, *172*, 225–253.

[229] Karthik, J.; Damodaran, A. R.; Martin, L. W. *Adv. Mater.* **2012**, *24*, 1610–1615.

[230] Bassiri-Gharb, N.; Fujii, I.; Hong, E.; Trolier-McKinstry, S.; Taylor, D. V.; Damjanovic, D. *J. Electroceram.* **2007**, *19*, 47–65.

[231] Sluka, T.; Tagantsev, A. K.; Damjanovic, D.; Gureev, M.; Setter, N. *Nat. Commun.* **2012**, *3*, 748–1–7.

[232] Kamel, T. M.; de With, G. *J. Appl. Phys.* **2007**, *102*, 044118–1–5.

[233] Nagarajan, V.; Roytburd, A.; Stanishevsky, A.; Prasertchoung, S.; Zhao, T.; Chen, L.; Melngailis, J.; Auciello, O.; Ramesh, R. *Nat. Mater.* **2003**, *2*, 43–47.

[234] Anbusathaiah, V.; Kan, D.; Kartawidjaja, F. C.; Mahjoub, R.; Arredondo, M. A.; Wicks, S.; Takeuchi, I.; Wang, J.; Nagarajan, V. *Adv. Mater.* **2009**, *21*, 3497–3502.

[235] Topsöe, H. *Zeitschrift für Kristallographie* **1884**, *8*, 246–296.

[236] Wyckoff, R. *Am. J. Sci.* **1928**, 349–359.

[237] Baikie, T.; Fang, Y.; Kadro, J. M.; Schreyer, M.; Wei, F.; Mhaisalkar, S. G.; Graetzel, M.; White, T. J. *J. of Mater. Chem. A* **2013**, *1*, 5628–5641.

[238] Im, J.-H.; Lee, C.-R.; Lee, J.-W.; Park, S.-W.; Park, N.-G. *Nanoscale* **2011**, *3*, 4088–4093.

[239] Filip, M. R.; Eperon, G. E.; Snaith, H. J.; Giustino, F. *Nat. Commun.* **2014**, *5*, 5757–1–9.

[240] Etgar, L.; Gao, P.; Xue, Z.; Peng, Q.; Chandiran, A. K.; Liu, B.; Nazeeruddin, M. K.; Graetzel, M. *J. Am. Chem. Soc.* **2012**, *134*, 17396–17399.

[241] Stoumpos, C. C.; Malliakas, C. D.; Kanatzidis, M. G. *Inorg. Chem.* **2013**, *52*, 9019–9038.

[242] Umari, P.; Mosconi, E.; De Angelis, F. *Sci. Rep.* **2014**, *4*, 4467–1–7.

[243] Geng, W.; Zhang, L.; Zhang, Y.-N.; Lau, W.-M.; Liu, L.-M. *J. Phys. Chem. C* **2014**, *118*, 19565–19571.

[244] Du, M. H. *J. Mater. Chem. A* **2014**, *2*, 9091–9098.

[245] Stranks, S. D.; Eperon, G. E.; Grancini, G.; Menelaou, C.; Alcocer, M. J. P.; Leijtens, T.; Herz, L. M.; Petrozza, A.; Snaith, H. J. *Science* **2013**, *342*, 341–344.

[246] Kutes, Y.; Ye, L.; Zhou, Y.; Pang, S.; Huey, B. D.; Padture, N. P. *J. Phys. Chem. Lett.* **2014**, *5*, 3335–3339.

[247] Frost, J. M.; Butler, K. T.; Brivio, F.; Hendon, C. H.; van Schilfgaarde, M.; Walsh A. *Nano Lett.* **2014**, *14*, 2584–2590.

[248] Quarti, C.; Mosconi, E.; De Angelis, F. *Chem. Mater.* **2014**, 6557–6569.

[249] Zheng, F.; Takenaka, H.; Wang, F.; Koocher, N. Z.; Rappe, A. M. *J. Phys. Chem. Lett.* **2015**, *6*, 31–37.

[250] Grinberg, I.; West, D. V.; Torres, M.; Gou, G.; Stein, D. M.; Wu, L.; Chen, G.; Gallo, E. M.; Akbashev, A. R.; Davies, P. K.; Spanier, J. E.; Rappe, A. M. *Nature* **2013**, *503*, 509–512.

[251] Wojdeł, J. C.; Íñiguez, J. *Phys. Rev. Lett.* **2014**, *112*, 247603.

[252] Xu, R.; Liu, S.; Grinberg, I.; Karthik, J.; Damodaran, A. R.; Rappe, A. M.; Martin, L. W. *Nat. Mater.* **2015**, *14*, 79–86.

[253] Farokhipoor, S.; Noheda, B. *Phys. Rev. Lett.* **2011**, *107*, 127601–1–4.

[254] Mosconi, E.; Amat, A.; Nazeeruddin, M. K.; Graetzel, M.; De Angelis, F. *J. Phys. Chem. C* **2013**, *117*, 13902–13913.

[255] Amat, A.; Mosconi, E.; Ronca, E.; Quarti, C.; Umari, P.; Nazeeruddin, M. K.; Graetzel, M.; De Angelis, F. *Nano Letters* **2014**, *14*, 3608–3616.

[256] Even, J.; Pedesseau, L.; Jancu, J.-M.; Katan, C. *J. Phys. Chem. Lett.* **2013**, *4*, 2999–3005.

[257] Egger, D. A.; Kronik, L. *J. Phys. Chem. Lett.* **2014**, *5*, 2728–2733.

[258] Kim, M.; Im, J.; Freeman, A. J.; Ihm, J.; Jin, H. *Proc. Natl. Acad. Sci.* **2014**, *111*, 6900–6904.

[259] Heyd, J.; Scuseria, G. E.; Ernzerhof, M. *J. Chem. Phys.* **2003**, *118*, 8207–8215.

[260] Heyd, J.; Scuseria, G. E.; Ernzerhof, M. *J. Chem. Phy.* **2006**, *124*, 219906–219906.

[261] Ma, J.; Wang, L.-W. *Nano Lett.* **2015**, *15*, 248–253.

[262] Gureev, M.; Tagantsev, A.; Setter, N. *Phys. Rev. B* **2011**, *83*, 184104–1–18.

[263] Morozovska, A. N.; Eliseev, E. A.; Varenyk, O. V.; Kalinin, S. V. *J. Appl. Phys.* **2013**, *113*, 187222–1–7.

[264] Landauer, R. *J. Appl. Phys.* **1957**, *28*, 227–34.

[265] Jiang, A.-Q.; Lee, H. J.; Hwang, C. S.; Tang, T.-A. *Phys. Rev. B* **2009**, *80*, 024119–1–7.

[266] Ducharme, S.; Fridkin, V. M.; Bune, A. V.; Palto, S. P.; Blinov, L. M.; Petukhova, N. N.; Yudin, S. G. *Phys. Rev. Lett.* **2000**, *84*, 175–178.